



**DEVELOPMENT OF OPTIMIZED PIEZOELECTRIC BENDING ACTUATORS
FOR USE IN AN INSECT SIZED FLAPPING WING MICRO AIR VEHICLE**

THESIS

Robert K. Lenzen, Second Lieutenant, USAF

AFIT-ENY-13-M-21

**DEPARTMENT OF THE AIR FORCE
AIR UNIVERSITY**

AIR FORCE INSTITUTE OF TECHNOLOGY

Wright-Patterson Air Force Base, Ohio

DISTRIBUTION STATEMENT A:
APPROVED FOR PUBLIC RELEASE; DISTRIBUTION UNLIMITED

The views expressed in this thesis are those of the author and do not reflect the official policy or position of the United States Air Force, the Department of Defense, or the United States Government.

This material is declared a work of the U.S. Government and is not subject to copyright protection in the United States.

AFIT-ENY-13-M-21

DEVELOPMENT OF OPTIMIZED PIEZOELECTRIC BENDING ACTUATORS
FOR USE IN AN INSECT SIZED FLAPPING WING MICRO AIR VEHICLE

THESIS

Presented to the Faculty
Department of Aeronautics and Astronautics
Graduate School of Engineering and Management
Air Force Institute of Technology
Air University
Air Education and Training Command
in Partial Fulfillment of the Requirements for the
Degree of Master of Science in Aeronautical Engineering

Robert K. Lenzen, B.S.M.E.
Second Lieutenant, USAF

March 2013

DISTRIBUTION STATEMENT A:
APPROVED FOR PUBLIC RELEASE; DISTRIBUTION UNLIMITED

AFIT-ENY-13-M-21

DEVELOPMENT OF OPTIMIZED PIEZOELECTRIC BENDING ACTUATORS
FOR USE IN AN INSECT SIZED FLAPPING WING MICRO AIR VEHICLE

Robert K. Lenzen, B.S.M.E.
Second Lieutenant, USAF

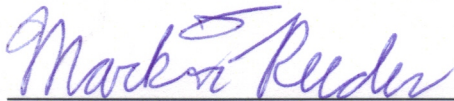
Approved:



Richard G. Cobb, PhD (Chairman)

1 MAR 2013

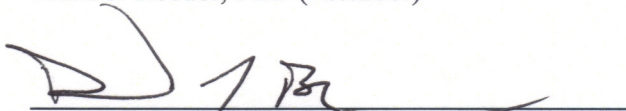
Date



Mark F. Reeder, PhD (Member)

1 Mar 2013

Date



David J. Bunker, PhD (Member)

28 Feb 2013

Date

Abstract

Piezoelectric bimorph actuators, as opposed to rotary electric motors, have been suggested as an actuation mechanism for flapping wing micro air vehicles (FWMAVs) because they exhibit favorable characteristics such as low weight, rapidly adaptable frequencies, lower acoustic signature, and controllable flapping amplitudes. Research at the Air Force Research Labs and the Air Force Institute of Technology has shown that by using one actuator per wing, up to five degrees of freedom are possible. However, due to the weight constraints on a FWMAV, the piezoelectric bimorph actuators need to be fully optimized to support free flight.

This study focused on three areas of investigation in order to optimize the piezoelectric actuators: validating and improving analytical models that have been previously suggested for the performance of piezoelectric bimorph actuators; identifying the repeatability and reliability of current custom manufacturing techniques; and determining the failure criteria for piezoelectric actuators so that they can be driven at the highest possible voltage.

Through the optimization, manufacturing, and performance testing of piezoelectric bimorphs, analytical models have been adjusted to fit the empirical data to yield minimum mass actuators that could potentially meet the mechanical energy requirements in a FWMAV. For custom manufactured actuators, optimized tapered actuators with an end extension showed an 89.5% energy density improvement over optimized rectangular actuators and a 19.5% improvement in energy density over commercially available actuators.

Acknowledgments

First and foremost I would like thank my thesis advisor Dr. Richard Cobb, who provided invaluable guidance and support throughout my research. Also, to Dr. Mark Reeder and Dr. Alan Jennings for asking great questions and providing suggestions during our meetings. To Capt. Garrison Lindholm for helping my to focus my research and always being enthusiastic. Additionally, to Maj. Ryan O'Hara and Mr. Nelson Freeman for their instruction and insights into the piezoelectric actuator manufacturing process. A am very thankful for everyone's help and support because I would not have been able to complete my research without it.

Robert K. Lenzen

Table of Contents

| | Page |
|--|-------|
| Abstract | iv |
| Acknowledgments | v |
| Table of Contents | vi |
| List of Figures | ix |
| List of Tables | xii |
| List of Symbols | xiv |
| List of Acronyms | xvii |
| I. Introduction | 1 |
| 1.1 Research Motivation | 1 |
| 1.2 Research Goals and Focus | 2 |
| 1.3 Organization of Thesis | 3 |
| II. Literature Review | 4 |
| 2.1 Flapping Actuator Design Choices | 4 |
| 2.1.1 Rotary Electric Motors | 5 |
| 2.1.2 Piezoelectric Actuators | 5 |
| 2.2 Characteristics of Piezoelectric Material | 7 |
| 2.2.1 Piezoelectric Power Electronics | 8 |
| 2.2.2 Mechanical Failure of Piezoelectric Ceramics | 9 |
| 2.2.3 Reorientation of the Piezoelectric Effect | 11 |
| 2.2.4 Piezoelectric Ceramic Properties | 13 |
| 2.3 Piezoelectric Actuator Design Choices | 15 |
| 2.3.1 Estimated Mass Requirements | 15 |
| 2.3.2 Types of Bending Actuators | 16 |
| 2.3.3 Actuator Driving Techniques | 18 |
| 2.3.4 Transmission Mechanism Design | 20 |
| 2.3.5 Manufacture of Piezoelectric Bending Actuators | 21 |
| 2.4 Analytical Analysis of Piezoelectric Actuators | 23 |
| 2.4.1 Euler-Bernoulli Piezoelectric Beam Analysis | 23 |

| | Page |
|---|------|
| 2.4.2 Lamination Theory Analysis for Bimorph Actuators | 25 |
| 2.5 Experimental Testing of Piezoelectric Actuators | 32 |
| 2.6 Statistical Analysis Techniques | 33 |
| 2.6.1 Hypothesis Testing | 33 |
| 2.6.2 Reliability Testing | 33 |
| 2.7 Chapter Summary | 34 |
| III. Methodology | 35 |
| 3.1 Preliminary Analytical Modeling | 35 |
| 3.1.1 Comparison of Models for a Rectangular Beam | 35 |
| 3.1.2 Predicted Effects of Design Variables on Actuator Performance . . | 36 |
| 3.2 Actuator Manufacture | 37 |
| 3.2.1 Construction Using Pyralux and Conductive Epoxy (Method 1) . . | 38 |
| 3.2.2 Construction Using Uncured Carbon Fiber (Method 2) | 43 |
| 3.3 Preliminary Model Validation | 45 |
| 3.3.1 Actuator Designs Used | 46 |
| 3.3.2 Free Displacement Measurement | 46 |
| 3.3.3 Blocked Force Measurement | 48 |
| 3.4 Secondary Force and Displacement Testing | 49 |
| 3.4.1 Primary Effects Testing | 50 |
| 3.4.2 Width Effects Testing | 50 |
| 3.4.3 Rectangular Actuator Testing | 50 |
| 3.5 Operating Range Testing | 51 |
| 3.5.1 Maximum Stress Testing | 52 |
| 3.5.2 Maximum Strain Testing | 53 |
| 3.5.3 Hysteresis Analysis | 54 |
| 3.6 Manufacturing Analysis | 55 |
| 3.7 Final Optimization | 55 |
| 3.8 Chapter Summary | 56 |
| IV. Analysis and Results | 57 |
| 4.1 Preliminary Analytical Modeling | 57 |
| 4.1.1 Comparison of Models for a Rectangular Beam | 57 |
| 4.1.2 Predicted Effects of Design Variables on Actuator Performance . . | 57 |
| 4.2 Preliminary Actuator Testing | 59 |
| 4.2.1 Actuator Mass Results | 60 |
| 4.2.2 Free Displacement Results | 62 |
| 4.2.3 Blocked Force Results | 64 |
| 4.2.4 Preliminary Actuator Comparison | 67 |
| 4.3 Primary Effects Testing | 68 |

| | Page |
|---|------|
| 4.4 Width Effects Testing | 70 |
| 4.5 Rectangular Actuator Testing | 71 |
| 4.6 Commercial Actuator Testing | 72 |
| 4.7 Final Model Results | 73 |
| 4.7.1 Mass Results | 73 |
| 4.7.2 Free Displacement Results | 75 |
| 4.7.3 Blocked Force Results | 78 |
| 4.7.4 Final Analytical Effects Analysis | 80 |
| 4.8 Operating Range Testing | 81 |
| 4.8.1 Maximum Stress Testing | 81 |
| 4.8.2 Maximum Strain Testing | 82 |
| 4.8.3 Maximum Voltage Testing | 83 |
| 4.8.4 Recommended Operating Ranges | 85 |
| 4.8.5 Hysteresis Analysis | 87 |
| 4.9 Manufacturing Analysis | 90 |
| 4.9.1 Piezoelectric Layer Cracking | 90 |
| 4.9.2 Bonding Failure Between Layers | 90 |
| 4.9.3 Actuator Short Out | 91 |
| 4.9.4 Piezoelectric Burn Out | 92 |
| 4.9.5 Comparison of Manufacturing Methods | 93 |
| 4.10 Final Optimization | 96 |
| 4.11 Chapter Summary | 98 |
| V. Conclusions and Recommendations | 99 |
| 5.1 Research Goals | 99 |
| 5.2 Conclusions | 99 |
| 5.3 Recommendations for Future Work | 101 |
| Appendix: MATLAB Functions | 103 |
| Bibliography | 105 |

List of Figures

| Figure | Page |
|--|------|
| 2.1 Example of flapping with rotary motor. | 4 |
| 2.2 Example of flapping with a piezoelectric actuator. | 4 |
| 2.3 Control mechanism with added piezoelectric ceramic. | 6 |
| 2.4 Electric field causing a deformation at the atomic level. | 7 |
| 2.5 Dual and single stage drive circuits for high voltage gains. | 9 |
| 2.6 Three point bending test. | 10 |
| 2.7 Effects of exceeding the coercive field. | 12 |
| 2.8 <i>Manduca sexta</i> mass properties. | 16 |
| 2.9 Comparison of unimorph and bimorph actuators. | 17 |
| 2.10 Various actuator driving techniques. | 18 |
| 2.11 Simultaneous driving technique. | 20 |
| 2.12 Transmission mechanism. | 21 |
| 2.13 Bending deformation of a bimorph actuator. | 24 |
| 2.14 Piezoelectric bimorph actuator nomenclature. | 28 |
| 2.15 Effects of width ratio on normalized strain. | 29 |
| 3.1 Carbon fiber layer manufacture. | 39 |
| 3.2 Pyralux layer manufacture. | 39 |
| 3.3 Piezoelectric layer manufacture. | 40 |
| 3.4 Teflon mold manufacture. | 40 |
| 3.5 Actuator assembly, method one. Top half called out; bottom half symmetric. . . | 41 |
| 3.6 Clamp and actuator assembly in oven. | 42 |
| 3.7 Assembled actuators, before cut out. | 42 |
| 3.8 Wires connected to actuator. | 43 |

| Figure | Page |
|---|------|
| 3.9 Teflon mold for construction method 2. | 43 |
| 3.10 Uncured carbon fiber placed in Teflon mold. | 44 |
| 3.11 Actuator assembly, method two. Top half called out; bottom half symmetric. . . | 45 |
| 3.12 Experimental testing setup. | 46 |
| 3.13 Actuator during free displacement measurement. | 48 |
| 3.14 Actuator during blocked force testing. | 48 |
| 3.15 Improved excitation voltage for blocked force testing. | 49 |
| 4.1 Predicted effects of design variables on output parameters. | 59 |
| 4.2 Scaled estimates of first and second-order effects. | 60 |
| 4.3 Actuator mass, experimental vs. modeled. | 61 |
| 4.4 Actuator mass, experimental vs. modeled (corrected). | 62 |
| 4.5 Sample free displacement plot, experimental and modeled. | 63 |
| 4.6 Displacement/voltage, experimental vs. modeled. | 64 |
| 4.7 Displacement/voltage, experimental vs. modeled (corrected). | 65 |
| 4.8 Sample blocked force plot, experimental and modeled. | 66 |
| 4.9 Force/voltage, experimental vs. modeled. | 66 |
| 4.10 Force/voltage, experimental vs. modeled (corrected). | 67 |
| 4.11 Sample blocked force plot, improved testing method, $R^2 = 0.9712$ | 69 |
| 4.12 Experimental effects of design variables on output parameters. | 70 |
| 4.13 Actuator masses, model vs. experimental data. | 74 |
| 4.14 Actuator masses, adjusted model vs. experimental data. | 75 |
| 4.15 Free displacement, model vs. experimental data. | 76 |
| 4.16 Free displacement, adjusted model vs. experimental data. | 77 |
| 4.17 Blocked force, model vs. experimental data. | 78 |
| 4.18 Blocked force, adjusted model vs. experimental data. | 80 |

| Figure | Page |
|--|------|
| 4.19 Weibull plot of the maximum stresses in actuators. | 82 |
| 4.20 Weibull plot of the maximum strains in actuators. | 83 |
| 4.21 Shorting out across piezoelectric layer. | 84 |
| 4.22 Weibull plot of the maximum voltage field for parallel drive. | 85 |
| 4.23 Weibull plot of the maximum voltage field for simultaneous drive. | 86 |
| 4.24 Hysteresis effects on the path of an actuator. | 88 |
| 4.25 Hysteresis effects after high electric fields. | 89 |
| 4.26 Fractured piezoelectric layer. | 91 |
| 4.27 Pyralux bonding failure. | 92 |
| 4.28 Conductive epoxy overflow between layers. | 92 |
| 4.29 Actuator burn out. | 93 |
| 4.30 Displacement compared to driving voltage and current. | 94 |
| 4.31 Failure percentages from manufacturing method one. | 95 |
| 4.32 Failure percentages from manufacturing method two. | 95 |
| 4.33 Optimized designs. | 97 |

List of Tables

| Table | Page |
|---|------|
| 1.1 DARPA MAV requirements. | 1 |
| 2.1 Piezoelectric ceramic material properties. | 14 |
| 2.2 $d_{31}E_C/\rho$ for piezoelectric materials. | 14 |
| 2.3 PZT-5H properties. | 15 |
| 2.4 Actuator design variables. | 31 |
| 3.1 Model comparison factors. | 36 |
| 3.2 Design of experiments factors. | 37 |
| 3.3 Carbon fiber material properties for a single cured layer. | 38 |
| 3.4 Preliminary actuator designs. | 47 |
| 3.5 Width variation actuator designs. | 51 |
| 3.6 Rectangular actuator designs. | 51 |
| 4.1 Percent difference between lamination theory and Euler-Bernoulli | 57 |
| 4.2 k values, preliminary testing. | 68 |
| 4.3 k values, primary effects testing. | 70 |
| 4.4 k values, width effects testing. | 71 |
| 4.5 k values, rectangular actuator testing. | 72 |
| 4.6 Commercial actuator comparison at 150 V for a 60/20/0.6 strip actuator. | 73 |
| 4.7 Agreement of actuator mass to original and adjusted models. | 75 |
| 4.8 Extension ratio corrections. | 76 |
| 4.9 Agreement of free displacement to original and adjusted models. | 78 |
| 4.10 Agreement of blocked force to original and adjusted models. | 79 |
| 4.11 Effects of changing design variables. | 81 |
| 4.12 Weibull distribution summary. | 87 |

| Table | Page |
|--|------|
| 4.13 Measured hysteresis in effectiveness. | 89 |
| 4.14 Theoretical improvement from an arbitrary rectangular actuator. | 96 |
| 4.15 Optimized actuator comparison, experimental data. | 97 |

List of Symbols

| Symbol | Definition |
|-------------|--|
| A | area (meters ²); amplitude (volts) |
| $[A]$ | extensional stiffness matrix (newtons/meter) |
| $[B]$ | coupling stiffness matrix (newtons) |
| $[C]$ | combined stiffness matrix inverse |
| D | density |
| $[D]$ | bending stiffness matrix (newton-meters) |
| d | piezoelectric strain constant (meters/volts) |
| E | electric field (volts/meter); elastic modulus (newtons/meter) |
| F | force (newtons) |
| f | blocked force correction function |
| G | shear modulus (pascals); extension ratio parameter |
| I | current (amps); second moment of area (meters ⁴) |
| k | Weibull shape parameter; correction factor |
| l | length (meters) |
| M | moment (newton-meters); moment per unit width (newtons) |
| m | mass (kilograms) |
| N | normal loads (pascals); number of samples |
| P | load (newtons); free curvature |
| $[Q]$ | local stiffness matrix (newtons/meter) |
| $[\bar{Q}]$ | global stiffness matrix (newtons/meter) |
| R | radius of curvature (meters) |
| S | extensional strain (meters/meter); survivability rate (%) |
| s | compliance matrix elements (meters ² /newton); standard deviation |

| Symbol | Definition |
|------------|---|
| T | stress (pascals) |
| t | thickness (meters), time (seconds) |
| U | energy (joules) |
| V | voltage (volts) |
| w | width (meters) |
| y | distance from midplane (meters) |
| z | distance from midplane (meters) |
| Δ | fractional change |
| δ | displacement (meters) |
| ϵ | strain (meters/meter) |
| θ | arc length (radians) |
| κ | curvature (1/meters) |
| λ | Weibull scale parameter |
| ν | free deflection (meters); Poisson's ratio |
| ρ | density (kilograms/meters ³) |
| σ | normal stress (pascals) |
| τ | shear stress (pascals) |

Subscripts

| | |
|---------|------------------------|
| 0 | initial; base |
| b | blocked; bias |
| C | coercive |
| d | drive |
| $E - B$ | Euler-Bernoulli theory |
| ext | external |

| Symbol | Definition |
|--------|---------------------------|
| f | fracture; final; forced |
| i | initial |
| lam | laminated plate theory |
| m | mechanical; midplane |
| nom | nominal |
| P | free; parallel |
| p | piezoelectric; polarizing |
| r | ratio |
| S | simultaneous |
| tot | total |
| U | mechanical energy |
| x | cross sectional |

Superscripts

| | |
|---|-----------|
| ' | prime |
| 0 | mid-plane |

List of Acronyms

| Acronym | Definition |
|---------|---|
| AFRL | Air Force Research Laboratory |
| AFIT | Air Force Institute of Technology |
| BO | Burn Out |
| CF | Carbon Fiber |
| DARPA | Defense Advanced Research Projects Agency |
| DC | Direct Current |
| DoE | Design of Experiments |
| EF | Early Failure |
| FWMAV | Flapping Wing Micro Air Vehicle |
| MAV | Micro Air Vehicle |
| MD | Manufacturing Defect |
| MEMS | Microelectromechanical Systems |
| PZT | Lead zirconate titanate |
| TC | Testing Completed |
| WPAFB | Wright-Patterson Air Force Base |

DEVELOPMENT OF OPTIMIZED PIEZOELECTRIC BENDING ACTUATORS
FOR USE IN AN INSECT SIZED FLAPPING WING MICRO AIR VEHICLE

I. Introduction

1.1 Research Motivation

Research by the RAND corporation has shown that low Reynolds number flight for unmanned aerial systems is feasible due to technological advancements that have occurred in the past two decades [12]. With this, the Defense Advanced Research Projects Agency (DARPA) created the Micro Air Vehicle (MAV) Program, whose goal is to develop small, low speed MAVs with minimal acoustic signature which could be used for intelligence, surveillance, and reconnaissance missions, as well as entry into denied locations due to environmental or hostile hazards [8]. The original goals of the DARPA program are listed in Table 1.1.

Table 1.1: DARPA MAV requirements [8].

| Parameter | MAV Value |
|----------------|-----------------------|
| Size | <15 cm |
| Weight | 10-100 grams |
| Useful Payload | 1-18 grams |
| Endurance | 20-60 minutes |
| Airspeed | 30-65 km/hr and hover |
| Range | 1-10 km |

Flapping wing micro air vehicles (FWMAVs) that are insect sized are one option to meet these goals. Research has shown that the unsteady aerodynamics that result from flapping can allow a FWMAV to be more maneuverable than a comparably sized MAV in steady flight [28]. Flapping flight, when optimized, also has the ability to conserve 27% more power than comparable steady flight [28]. The rotational mechanism in the wings can also function to provide both lift and control [9]. Other benefits include low acoustic signature, vertical takeoff and landing, and the ability for autonomous flight which are all important characteristics if the FWMAV were to be used in a covert setting [45].

Research at the Air Force Institute of Technology (AFIT) has focused on using biomimicry to create a FWMAV that has a similar wing size and shape to the *Manduca sexta*, or hawk moth. By replicating the hawk moth's wing shape, size, and inertial properties, engineered wings have been created that produce about 1 gF of lift per wing [24]. Options for wing actuation include linear actuators, such as piezoelectric bimorph actuators, and DC rotary motors. For application in a hawk moth sized flight vehicle, which has a wingspan of 45-55 mm per wing [24], piezoelectric bimorph actuators are preferred because they are more efficient at this small scale [23] and allow for each wing's stroke angle to be actuated independently. By allowing each wing to be moved independently with piezoelectric actuators, up to five degrees of freedom are achievable [2].

1.2 Research Goals and Focus

The development of an insect sized FWMAV presents several challenges including control, power storage, lift generation, and wing actuation. This research focuses on the wing actuation, in particular the design of the piezoelectric actuators. Currently, commercially available actuators from Omega Piezo are used in testing. However, these actuators weigh 4.45 grams [26], which is much greater than the lift produced per wing. Therefore, in order for flight to occur the mass of these actuators must be reduced.

Existing models based on classical lamination theory for composites have already been developed by the Harvard Microrobotics Laboratory which suggest tapering the width of an actuator and adding a rigid extension to improve the energy density of the actuators [42]. However, the size of the FWMAVs produced by Harvard are much smaller than the hawk moth sized FWMAVs that AFIT is trying to develop.

In order to create actuators that are useful for the FWMAV research at AFIT, the models that have already been developed for actuator performance must be validated against experimental data. Additionally, custom manufacturing techniques should be examined in the process of experimental testing to determine how to produce actuators reliably and with minimal defects. Finally, the maximum operating range in which the actuators can be used should be determined. The operating range could be a function of the stress, strain, or electric field that the actuator experiences during use. Combining the results of these three research areas, actuators can be optimized for minimum mass to meet the requirements of a dual actuated FWMAV, with a total wingspan less than 11 cm and mass less than 2 grams.

1.3 Organization of Thesis

This thesis begins by describing previous research in piezoelectric actuators and their use in FWMAVs, which is detailed in Chapter II. Next, Chapter III discusses the methodology for the analytical and experimental testing and analysis of the actuators. The results and analysis from the testing are detailed in Chapter IV. Finally, Chapter V discusses the conclusions that were drawn from the results and provides suggestions for future work.

II. Literature Review

2.1 Flapping Actuator Design Choices

Presently, there are various actuator designs to power the flapping mechanism on a FWMAV, however most of these fall under two categories: rotary motors (small DC motors or internal combustion engines) and linear actuators (piezoelectric benders, solenoids, etc), which can be seen in Figures 2.1 and 2.2. Both of these sources have been used to achieve flight in a MAV. Rotary motors were successfully used in the Nano Hummingbird developed by AeroVironment [18], and piezoelectric actuators were successful in the flight of a 60 mg Microrobotic Fly at Harvard [40]. However, both of these systems have disadvantages which demonstrate the need for further research into the actuation mechanism.

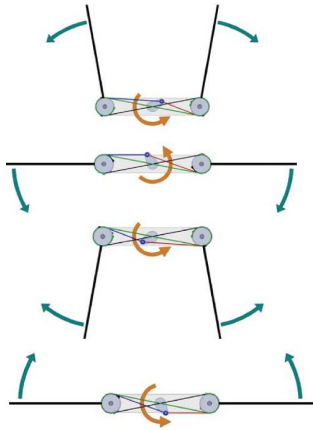


Figure 2.1: Example of flapping with rotary motor [18].

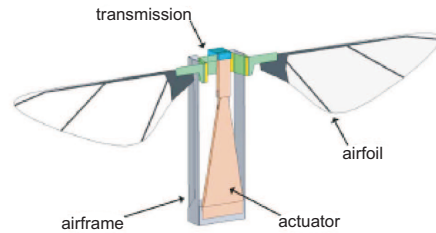


Figure 2.2: Example of flapping with a piezoelectric actuator [38].

2.1.1 Rotary Electric Motors.

In the case of the Nano Hummingbird, the total wing span was 16.5 cm [18], the propulsion motor was 3.65 grams (21% of the total mass), and the FWMAV was controlled through combined twist and rotation modulation of the wings, which added another 1.50 grams. While the Nano Hummingbird is an example of successful controlled flight, the use of a rotary motor as a flapping mechanism is not necessarily useful in the development of an insect-sized FWMAV with two independently actuated wings.

The utility of an electric motor in smaller MAVs degrades due to both efficiency and mass. Electric motors typically require some sort of gearing, an example of which is shown in Figure 2.1. As these motors are miniaturized, the losses due to friction in a gearbox become more apparent, which limits their practicality [23]. Also, electric motors require separate mechanisms for control which adds weight to the MAV; this can be seen in the case of the Nano Hummingbird, where the control mechanisms accounted for 9% of the overall MAV mass [18]. The frictional losses and control requirements are both serious issues that diminish the adequacy of using rotary motors for a flight vehicle that weighs less than 2 grams.

2.1.2 Piezoelectric Actuators.

Piezoelectric actuators, on the other hand, have the potential to be both lightweight enough to power insect sized FWMAVs and robust enough to allow control without adding unnecessary mass. The Harvard Microrobotic Fly has already demonstrated that it is possible to achieve necessary lift using piezoelectric actuators. However this occurred with the aid of guide wires for control and an external power source [40]. Despite this, further work on this concept has shown that three degrees of freedom are possible through independently altering the kinematics of each wing with the addition of another piezoelectric actuator, which can be seen in Figure 2.3 [11]. This allowed for modulating the lift force that each wing produced, which translated into altitude control [27].

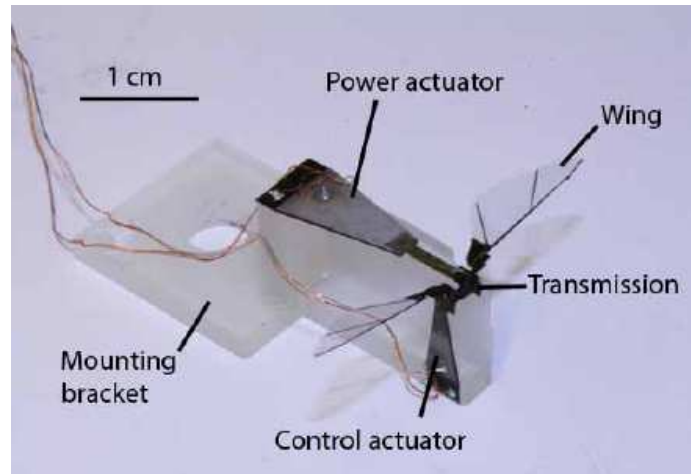


Figure 2.3: Control mechanism with added piezoelectric ceramic [11].

However, using the design shown in Figure 2.3 had two drawbacks: only three degrees of freedom were available for use in control and the added actuator only provided control but did not contribute to the flapping of the MAV, which was an inefficient use of resources. Ideally, the same actuators should be used for both actuation and control. This is possible by using one piezoelectric actuator per wing so that the stroke amplitude and frequency of each wing can be varied independently [20]. Through careful control techniques, five degrees of freedom have been possible with only two actuators using independently controlled wings [2].

Therefore, to optimize both the weight and maneuverability of an insect sized FWMAV, the best design choice utilizes two piezoelectric actuators for both power and control that operate each wing independently. This scheme that allows for a dramatic improvement in maneuverability over one and three degree of freedom systems. However, since there would be two piezoelectric actuators, the effects of the actuators on the weight would be doubled. In order to optimize the actuators for size, mass, displacement, and force there are many design variables with respect to the actuators that need to be studied. Therefore, a further understanding of the effects of piezoelectric material

properties, piezoelectric weaknesses, and the construction of piezoelectric beams on the overall actuator is required.

2.2 Characteristics of Piezoelectric Material

The piezoelectric effect was first discovered in 1890 by the Curie brothers, who observed that when a pressure was applied to certain materials, such as zinc blende, quartz, boracite, and others, an electrical charge was produced. The opposite effect, where an applied electrical charge produced a mechanical deformation was observed a year later [17].

A material becomes polarized when an electric field is applied, and for piezoelectric materials this causes a deformation. The deformation results from the polarized material causing the electrons and the nuclei to rearrange in such a way that the dimensions of the material are changed, as shown in Figure 2.4 [15].

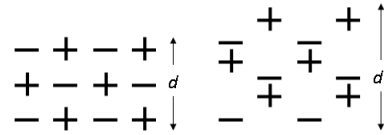


Figure 2.4: Electric field causing a deformation at the atomic level.

The first useful application of this effect came in the 1920's when quartz was used as a means of frequency control. More recently piezoelectric ceramics have found their way into microelectromechanical systems (MEMS), specifically in cantilever unimorph and bimorph actuator designs, which utilize a passive layer to induce a bending moment [4]. Two descriptive values for piezoelectric actuators are the blocked force, F_B , and the free displacement, δ_P [42]. The blocked force is the force generated at the tip of an actuator with zero displacement, and the free displacement is the displacement of the actuator tip without any applied external force. These values can be used to determine the mechanical energy

that an actuator is able to produce by calculating the area under the force-displacement curve. The mechanical energy, U_m can be calculated using Equation 2.1 [42].

$$U_m = \frac{1}{2} F_B \delta_P \quad (2.1)$$

Constructing piezoelectric actuators for use in FWMAVs utilizes the ability of the material to expand or contract with an applied electrical voltage. The capability of the piezoelectric material to produce mechanical motion is described by the piezoelectric strain constant (length/volt), which is denoted as d_{ij} , as shown in Equation 2.2, and has units of meters per volt. The piezoelectric constant specifies how much a material will deform in the j direction due to an applied electric field in the i direction [30].

$$d_{ij} = \frac{\text{strain developed (m/m)}}{\text{applied electric field (V/m)}} \quad (2.2)$$

2.2.1 Piezoelectric Power Electronics.

Using actuators made out of piezoelectric ceramics poses several challenges, not the least of which are the high voltage fields required to operate them, which are on the order of 200 V/mm [38]. For a very small MAV, the electronics required to provide these voltage fields could pose a weight problem because most compact energy sources provide outputs below 5 volts, which requires a gain between 50 and 100 [14]. Therefore, lightweight and efficient circuits will be required on free-flying flight vehicles.

There are several options available in order to provide this large voltage input, which include boost converters, transformers, and hybrid converters. Boost converters, which include an inductor, transistor, diode, and capacitor work by rapidly changing the current across the inductor and using the higher voltage produced to charge the capacitor; however at high voltages this approach becomes less efficient due to losses in conduction and the switching [10]. Commercially available micro transformers are available which can

provide amplification from 5 to 250 volts, however these weigh about 4 grams [29], which are too heavy for the required application.

A hybrid approach that utilizes a boost converter with several cascading charge pumps has been demonstrated by Harvard's MAV group to have a low mass, at 225 mg, with a relatively high efficiency, of above 60% [10]. Further refinement has dropped the weight and size of the drive circuits to 90mg for a dual-stage circuit for use in powering a bimorph actuator, as shown in Figure 2.5 [14]. This shows that despite the high voltages required to drive the piezoelectric beams, lightweight electronics can be produced that still allow for flight.



Figure 2.5: Dual and single stage drive circuits for high voltage gains [14].

2.2.2 Mechanical Failure of Piezoelectric Ceramics.

The goal of this research is to optimize the piezoelectric actuators for strength, displacement, and weight. However, for the most power to be produced from a given actuator, the drive voltages must be as high as possible. To find the maximum usable voltage, the failure criteria for the piezoelectric material must be known. The brittleness of piezoelectric materials is its biggest weakness, particularly when stress and electric field concentrations are present near defects or electrodes [43]. Therefore, a thorough understanding of how to determine the failure strength of piezoelectric materials is necessary.

One such way to determine the fracture stress (σ_f) of a piezoelectric ceramic is to perform a three point bending test, as shown in Figure 2.6, which applies a known load to a piece of piezoelectric material until failure. Using this test, the fracture stress can be solved for through Equation 2.3, where P_f is the load at fracture [33].

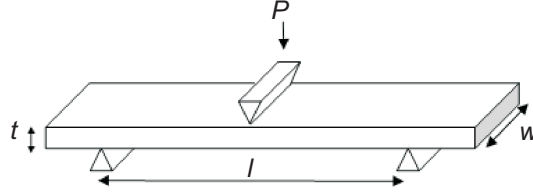


Figure 2.6: Three point bending test.

$$\sigma_f = \frac{3 * l}{2wt^2} P_f \quad (2.3)$$

Lead zirconate titanate ceramic type 5H (PZT-5H), the type of piezoelectric ceramics currently used at AFIT due to the material's high piezoelectric constant, has been determined through three point bending testing to have a fracture strength of 114.8 MPa, with a 95% confidence interval the actual strength is 112.8 and 116.9 MPa. However, research has also shown that when the piezoelectric ceramics are used in a composite, which would be the case for piezoelectric actuators, the strength can increase by over 30%. One possible explanation for this strength increase is that the bonding process increases the shear strength on the surface of the ceramics [32].

Due to the differences in the ceramic strength when bonded in a composite compared to the non-bonded crystal, as well as possible differences due to an applied stress or an applied voltage, the actual strength of powered piezoelectric actuators may be different from this data, and the actual failure levels should be more thoroughly investigated.

2.2.3 Reorientation of the Piezoelectric Effect.

Besides brittle fracture, piezoelectric ceramics can also experience a failure or minimization of the piezoelectric effect due to depolarization and subsequent piezoelectric constant degradation. Initially, the polarization within a piezoelectric ceramic is internally random, which cancels out any net polarization. In order for the ceramics to be useful, a relatively large electric field ($> 3000 \text{ V/mm}$) is applied to initially polarize the ceramics [33]. However, high voltage fields, stresses, and vibrations can all affect this initial polarization, reorient the domain, and cause a degradation of the piezoelectric constants in the material.

At lower applied voltage fields, the relationship between the strain produced and the field is mostly linear, which is what would be predicted by Equation 2.2. However, as the strength of the field increases, there is a polarization reorientation which causes hysteresis effects as the strain deviates from the linear region. Hysteresis effects are usually observed as the electric field becomes greater than about 100 V/mm , however depoling of the material can still occur under long term driving [33]. Hysteresis and depoling caused by high driving voltages mean that linear models significantly over predict the power which can be developed from piezoelectric materials [41].

Piezoelectric ceramics also have a critical electric field, referred to as the coercive field, after which the hysteresis effects cause a “butterfly” shaped curve, which can be seen in Figure 2.7. This radical hysteresis is caused by a permanent change in the ferroelectric domain status and radically changes the effects of an applied voltage on the piezoelectric ceramic. Soft ceramics are especially sensitive to this effect when driven with an electric field opposite the poling direction [33].

“Soft” ceramics are those that have a coercive field between $10 - 100 \text{ V/mm}$ while “hard” ceramics have a coercive field larger than 100 V/mm [33]. Due to the difference in coercive fields, hard ceramics are less likely to experience any hysteresis effects, which is

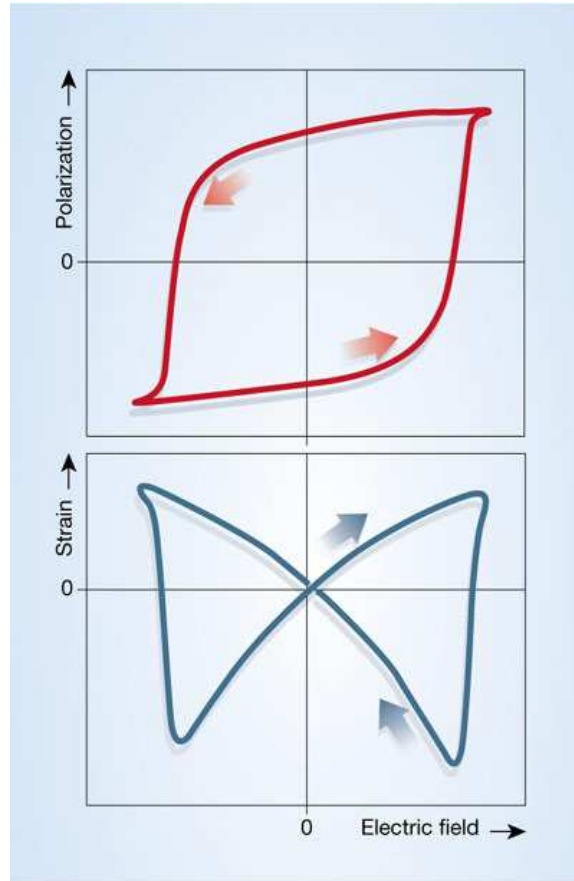


Figure 2.7: Effects of exceeding the coercive field [6].

a favorable trait. However, hard ceramics also require larger electric fields to produce the same strain. Therefore, for use in FWMAV applications where power is of concern, soft ceramics tend to be more suitable.

Externally applied compressive static and cyclic stresses have also been shown to affect the piezoelectric effect. Under loading in the range of 10 to 70 MPa, significant degradation has been observed, especially in soft ceramic materials. When static loads of 30 MPa were applied to PZT-5H ceramics, the d_{33} coefficient was 50% of the original value; after 70 MPa, the coefficient was only 25% of the original value. Cyclic loading also seemed to increase the amount of degradation [1]. Piezoelectric bending actuators are

typically only concerned with the d_{31} coefficient, not the d_{33} coefficient. The d_{31} coefficient applies to elongation perpendicular to the applied electric field while the d_{33} coefficient describes elongation parallel to the applied electric field. While the values are different, there may be a similar effect on the d_{31} coefficient caused by applied stresses.

Vibrational loads, in addition to causing mechanical fracture, have also been observed to be associated with a domain reorientation of piezoelectric actuators. This reorientation has been noticed especially with respect to soft ceramics with high driving fields. Also, during domain reorientation, the magnitude of the current, admittance, and temperature of the actuator has been observed to increase both significantly and abruptly [16]. Since the purpose of this research is to develop piezoelectric bimorph actuators to quickly flap wings, vibrational failure issues will certainly be important.

2.2.4 Piezoelectric Ceramic Properties.

There are several commercially available sheet ceramics which can be used in the construction of custom piezoelectric bimorph actuators. Table 2.1 summarizes two of the single crystal ceramic sheets available from Piezo Systems, Inc. [30]. The polarizing field, E_p , is the electric field that is applied to initially polarize the piezoelectric ceramic. If a ceramic becomes depolarized, then applying this field should reorient the material. The initial depolarizing field, $E_{C,i}$, is the electric field that causes domain reorientation to begin and the coercive field, $E_{C,f}$, is essentially the final depolarizing field, which was explained in Section 2.2.3. The density and elastic modulus are all standard mechanical properties.

The best piezoelectric material for weight consideration will be able to achieve the greatest elongation with the least mass (δ_{max}/m). Equation 2.4 shows how this elongation can be calculated as a function of the piezoelectric constant, depolarizing field, and the cross sectional area, A_x .

$$\frac{\delta_{max}}{m} = \frac{l_p \epsilon_{max}}{\rho l_p w t} = \frac{d_{31} E_C}{\rho} \frac{1}{A_x} \quad (2.4)$$

Since the cross sectional area is a function of the geometry and not a material property, the only term that matters is $d_{31}E_C/\rho$. The best material choice will maximize this value. Table 2.2 gives a comparison for both the initial depolarization field and the coercive depolarization field. In both cases, PZT-5H is more advantageous for use in lightweight actuators than other options.

Table 2.1: Piezoelectric ceramic material properties [30].

| | | | PZT-5H | PZT-5A |
|----------------------------|-----------|-------------------|-------------------------|---------------------------|
| Piezoelectric Constant | d_{31} | m/V | 320×10^{-12} | 190×10^{-12} |
| Polarizing Field | E_p | V/m | $> 1.5 \times 10^6$ | $> 2 \times 10^6$ |
| Initial Depolarizing Field | $E_{C,i}$ | V/m | $\approx 3 \times 10^5$ | $\approx 5 \times 10^5$ |
| Coercive Field | $E_{C,f}$ | V/m | $\approx 8 \times 10^5$ | $\approx 1.2 \times 10^6$ |
| Density | ρ | kg/m ³ | 7800 | 7800 |
| Elastic Modulus | E_3 | N/m ² | 5.0×10^{10} | 5.2×10^{10} |
| | E_1 | N/m ² | 6.2×10^{10} | 6.6×10^{10} |

Table 2.2: $d_{31}E_C/\rho$ for piezoelectric materials.

| | PZT-5H | PZT-5A |
|-------------------------|------------------------|------------------------|
| Initial Depolarization | 1.231×10^{-8} | 1.218×10^{-8} |
| Coercive Depolarization | 3.282×10^{-8} | 2.923×10^{-8} |

Piezo Systems, Inc. supplies PZT-5H in three thicknesses, 0.127 mm, 0.191 mm, and 0.267 mm [30]. The voltage that correlates to the polarizing and depolarizing fields

can be calculated by multiplying the electric field by the piezoelectric ceramic thickness ($V = E \times t_p$). The applied voltages for each thickness of PZT-5H are given in Table 2.3.

2.3 Piezoelectric Actuator Design Choices

2.3.1 Estimated Mass Requirements.

Utilizing two independently actuated wings, AFIT research has focused on developing a FWMAV that is of comparable size to the *Manduca sexta*, which is more commonly referred to as the hawk moth. On average, each wing of the hawk moth is between 45 and 55 millimeters and able to produce about 1 gF of lift. By matching the structural properties of the biological wing, manufactured wings of comparable size and weight have also been able to produce about 1 gF of lift [24]. This means that a flight vehicle which is the same size as the hawk moth must have a total mass less than 2 grams.

Table 2.3: PZT-5H properties [30].

| Ceramic Thickness | | .127 mm (.005 in.) | .191 mm (.0075 in.) | .267 mm (.0105 in.) |
|------------------------------|-----------|-----------------------|------------------------|------------------------|
| Polarizing Voltage | V_p | 190.5 | 286.5 | 400.5 |
| Initial Depolarizing Voltage | $V_{C,i}$ | 38.1 | 57.3 | 80.1 |
| Coercive Voltage | $V_{C,f}$ | 101.6 | 152.8 | 213.6 |

In order to estimate how much of the total mass is available for each subsystem, the natural mass properties of the hawk moth can be examined, and mechanical analogies can be developed. Figure 2.8 shows the average mass of different sections of the *Manduca sexta*. Mechanically, the head can be analogous to control mechanisms, the abdomen to power, and the thorax to the flapping mechanism. For the *Manduca sexta*, the thorax has an average mass of 0.5840 grams [24]. Therefore, if a dual actuated design is used, each

piezoelectric actuator assembly and transmission mechanism should have a mass of about 0.29 grams.

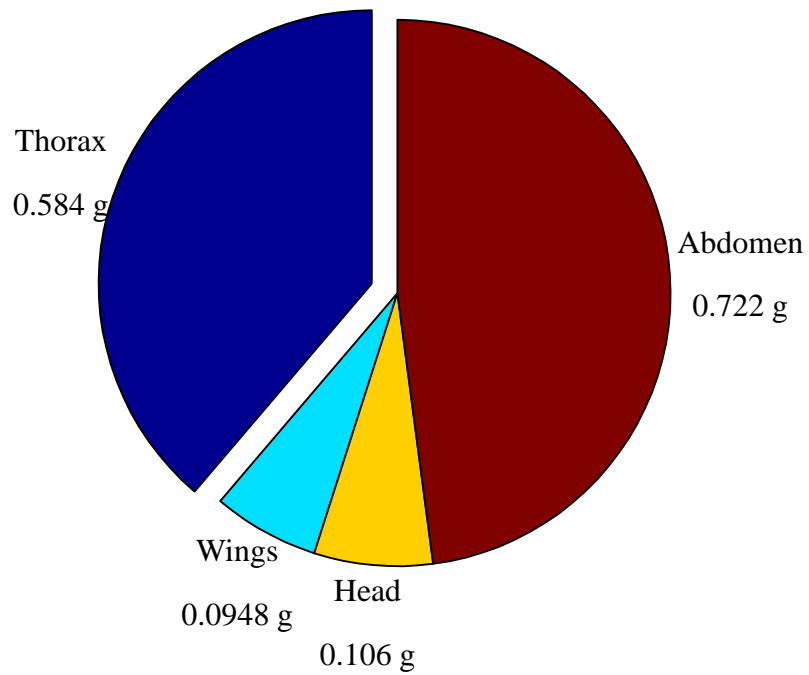


Figure 2.8: *Manduca sexta* mass properties [24].

2.3.2 Types of Bending Actuators.

Two ways that piezoelectric material can be used to create bending actuators is through unimorph and bimorph designs. In both of these designs, piezoelectric material is bonded to a passive layer so that the strains induced from the applied electric field generate a curvature along the length of the actuator. Unimorph actuators use only one piezoelectric layer combined with a passive layer, while a bimorph actuator uses two piezoelectric layers and a passive layer. Examples of a unimorph and bimorph actuators are shown in Figure 2.9.

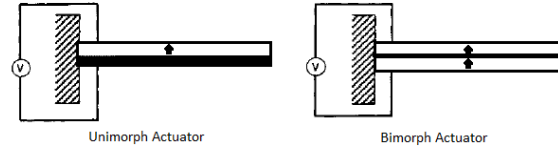


Figure 2.9: Comparison of unimorph and bimorph actuators [34].

Unimorph actuators have been able to achieve 180° stroke motion for a FWMAV, which shows that these actuators could be used in FWMAVs [31]. These actuators are lighter than bimorph actuators because they only have one piezoelectric layer. Also, in the construction of custom actuators, unimorphs only require two layers to be bonded, which makes assembly simpler.

On the other hand, bimorph actuators can simply be seen as unimorph actuators with an additional piezoelectric layer added. While unimorph actuators are lighter than bimorph actuators with equivalent geometry and electric field strength, bimorph actuators are able to produce twice the deflection as unimorphs [34]. The increase in deflection can be used to offset the increase in weight seen in bimorphs. Unimorph actuators also require that the electric field be applied opposite the direction of the piezoelectric ceramic poling, which can quickly lead to hysteresis effects as the ceramics become depoled [33]. Therefore, piezoelectric bimorph actuators appear to be a better choice than unimorph actuators.

In the construction of bimorph actuators, the piezoelectric crystals can either be connected in series or in parallel. A series connection means that the two piezoelectric layers are poled opposite each other so that an electric voltage is applied through the entire thickness to induce bending. A connection in parallel means that each piezoelectric layer is poled in the same direction. With the parallel connection, a voltage is applied opposite in each layer to induce bending. In both cases, bending is created by one piezoelectric layer expanding while the other contracts [35].

Currently, FWMAV bench tests at AFIT have used piezoelectric strip actuators manufactured by Omega Piezo Technologies, Inc., which are the equivalent of parallel poled bimorph actuators. The 20×60 mm actuators that are currently used have a maximum published voltage of 150 volts in the polarized direction, a free deflection of 2.6 mm, and a blocked force of 0.30 N. These actuators have a central electrode made of stainless steel which is bonded to two piezoelectric ceramic plates [26]. However, the mass of a single actuator is 4.45 grams, which is much too heavy to be used with a FWMAV that potentially produces only about 2 gF of lift [24].

2.3.3 Actuator Driving Techniques.

Several techniques are available to provide power to piezoelectric actuators, which depend upon the poling direction of the piezoelectric ceramics and the number of drive sources available. Figure 2.10 gives examples of each technique. Ideally, the driving technique that is used would work to ensure that hysteresis effects do not develop.

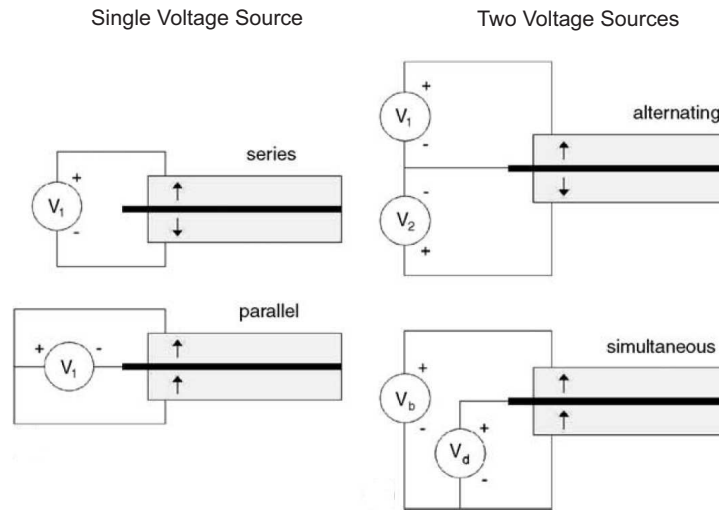


Figure 2.10: Various actuator driving techniques [42].

Series and parallel driving techniques both require only one voltage source to provide power to the bimorph actuators. For the series case, the piezoelectric layers are poled in opposite directions and a wire is attached to the outside of each piezoelectric ceramic. This is the simplest driving method, however this method requires twice the voltage compared to other techniques to create the same electric field and one piezoelectric layer is always being driven opposite the poling direction, which increases hysteresis effects [42].

For parallel driving, the piezoelectric layers are both poled in the same direction, and the passive middle layer is grounded. The electric field is created by applying an equal voltage to the outer layer of each piezoelectric ceramic. This technique overcomes the issue of doubling the voltage to create an electric field, however the piezoelectric ceramic layers will still need to be charged opposite of the poling direction in order to move in both directions [42].

Both of the driving techniques that utilize a single drive source experience the issue of creating an electric field antiparallel to the poling direction of the piezoelectric ceramics, which could cause depoling with a field of only about 5×10^4 V/m. In order to solve this problem, two driving sources can be used in either an alternating drive configuration or a simultaneous drive configuration. For an alternating drive, each piezoelectric layer is driven individually by a separate drive source [42].

While the alternating drive configuration does keep each actuator charged parallel to the poling, two separate driving sources are required for each actuator. A more economical technique is to use a simultaneous drive method. This method initially charges each actuator with a bias voltage, V_b , and then charges the central passive layer with the drive voltage. At the neutral state, the drive voltage is half of the bias voltage, or $V_b/2$. The drive voltage can then be varied from 0 to V_b [41]. An example of how this method works is shown in Figure 2.11. This technique prevents charging in the opposite direction of poling and allows for a common ground and common bias voltage source across all actuators [42].

The simultaneous drive technique should prevent easily depoling the actuators while still not requiring a large amount of extra electronics, which makes it the best choice for a FWMAV.

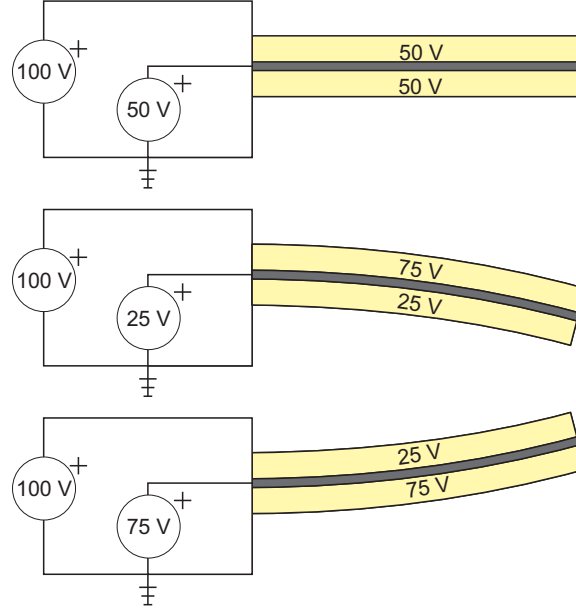


Figure 2.11: Simultaneous driving technique.

2.3.4 Transmission Mechanism Design.

Piezoelectric actuators produce tip displacements that are typically on the order of ± 1 mm, and the FWMAV requires a wing stroke angle of $\pm 60^\circ$ [24]. In order to achieve this result, a transmission mechanism that has linkages similar to Figure 2.12 has been used. The linkage lengths $L_1 - L_4$ must be specified in order to define the linkage, which can be analytically shown in Equation 2.5 [39]. However, this equation is not very useful for the general linkage design because it cannot be analytically solved. If θ_w (stroke angle) and δ (actuator tip deflection) are assumed to be small, then Equation 2.5 can be reduced to Equation 2.6, where T is the transmission ratio. While Equation 2.6 is not valid for larger stroke angles, it shows that linkage L_3 plays the largest role in the transmission ratio.

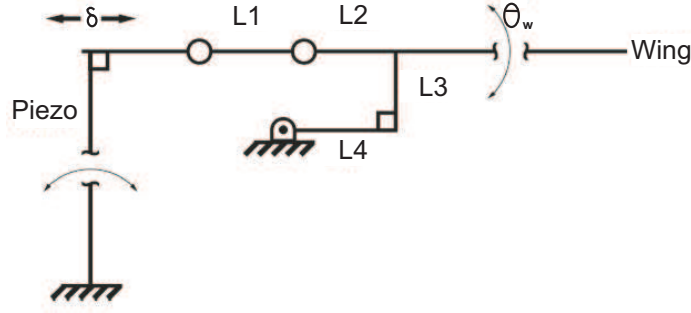


Figure 2.12: Transmission mechanism [24].

$$\theta_w = \cos^{-1} \left(\frac{\delta^2 - 2\delta L_1 + eL_3^2}{2L_3 \sqrt{(L_1 - \delta)^2 + L_3^2}} \right) + \tan^{-1} \left(\frac{L_3}{L_1 - \delta} \right) - \frac{\pi}{2} \quad (2.5)$$

$$T \equiv \frac{\theta_w}{\delta} \approx \frac{1}{L_3} \quad (2.6)$$

These results show that for any given actuator displacement (whether large or small), there is a linkage design that will allow the wing to be flapped with $\pm 60^\circ$ deflection. However, a safe assumption is that as the required displacement decreases, the required force increases since the same amount of mechanical energy will be needed. Therefore, the mechanical energy that an actuator produces is the most important output design variable.

2.3.5 *Manufacture of Piezoelectric Bending Actuators.*

While commercially produced piezoelectric bending actuators are available, specific weight and size requirements dictate that custom actuators be produced for FWMVs. The fabrication of custom actuators also allows for a thorough analysis of the design of each mechanism so that optimized actuators can be developed. While the general process of bonding two active piezoelectric layers to a middle passive layer is the same for all manufacturing techniques, there are variations in the bonding process, connection methods, and material choice for different manufacturing techniques.

Three processes have been used to bond the active and passive layers of a piezoelectric actuator. Non-conductive epoxy has been used in the design of unimorphs [31], sheet adhesives (such as DupontTM Pyralux) has been used in the construction of microelectromechanical systems (MEMS) [37], and the epoxy in uncured pre-impregnated (prepreg) carbon fiber has also been used in bending [42] and curved [44] actuators. The use of uncured carbon fiber, while eliminating the need for an extra bonding agent, makes the final actuator more difficult to assemble due to challenges in working with the carbon fiber.

When the epoxy in the prepreg carbon fiber is used as a bonding agent, there is no need for an additional connection method between the layers of the actuator [44]. However, if a non-conductive epoxy or sheet adhesive is used, then there must be some method to connect the piezoelectric layers to the passive layer so that current can flow through the entire actuator. This connection can be accomplished by creating a slight overhang of the piezoelectric ceramic, and then using a conductive epoxy to connect the passive and active layers [31]. Wires can also be connected to the outer layer of the piezoelectric ceramics by using conductive epoxy or using a soldering flux [31].

The last choice in the manufacture of the piezoelectric actuators is the selection of a passive layer material. Typically, the passive layer is both stiff and electrically conductive. Steel is commonly used in commercial actuators, and it has also been used in the construction of custom actuators as well because a stiffer passive layer has been shown to increase the output force of an actuator [34]. However, steel also dramatically increases the weight of the actuator. Therefore, carbon fiber has been used as a passive layer in weight sensitive applications, with fiberglass added to increase the stiffness and to act as an electrical insulator around the entire actuator [42]. Custom actuators manufactured at AFIT have also used carbon fiber, but without the use of fiberglass because the AFIT FWMAV design does not require the tip of the actuator to be electrically insulated [1].

2.4 Analytical Analysis of Piezoelectric Actuators

Several analytical solutions have been proposed for predicting the performance of piezoelectric bimorph actuators. Approaches utilizing the Euler-Bernoulli beam theory [34] and laminated beam analysis [42] have been created for determining the blocked force and displacement of an actuator excited by a voltage. The Euler-Bernoulli approach assumes a rectangular actuator shape, while the laminated beam analysis allows for the actuator to be tapered along the width. By tapering along the width, the actuators can be designed for optimal energy density [42].

2.4.1 Euler-Bernoulli Piezoelectric Beam Analysis.

Bimorph actuators function by using the piezoelectric strains to create a curvature in the beam. The Euler-Bernoulli beam theory can be used to analyze the performance of an actuator by treating these internal strains as internal moments that generate a curvature [36]. This analysis assumes that there is perfect bonding between the layers, the beam is a rectangular shape, and the only loads are internal to the beam and caused by the piezoelectric effect [34]. If T_i is defined as the stress in the i th direction, and the principal direction along the length of the beam, then $T_2 = T_3 = T_4 = T_5 = T_6 = 0$ [34].

Since the only loads acting on the actuator are internal extensional loads from the piezoelectric layers, the extensional strains in each layer are described in Equation 2.7, where s_{ij} are elements of the mechanical compliance matrix.

$$S_1 = s_{11}T_1 + d_{31}E_3 \quad (2.7)$$

The internal loads in each layer can be solved for by rearranging Equation 2.7. For the passive layer, the piezoelectric constant, d_{31} , is zero. Also, $(s_{11})^{-1}$ is actually the Young's modulus of each layer, so that E_p can be used for the piezoelectric layer and E_m can be used for the middle passive layer [34].

The extensional strain, S_1 , can be written as a function of the curvature of the beam and position along the y -axis. Figure 2.13 shows the nomenclature and axis for the beam

curvature, where the mid-plane does not undergo any extensional deformation. Since the curvature is defined as $1/R$, where R is the radius of curvature, the extensional strain is given in Equation 2.8.

$$S_1 = \frac{l' - l}{l} = \frac{(R + y)\theta - R\theta}{R\theta} = \frac{y}{R} = \kappa y \quad (2.8)$$

After making the substitutions for Young's modulus and the extensional strains, the internal loads are given in Equation 2.9 for the piezoelectric layers and Equation 2.10 for the middle layer [34].

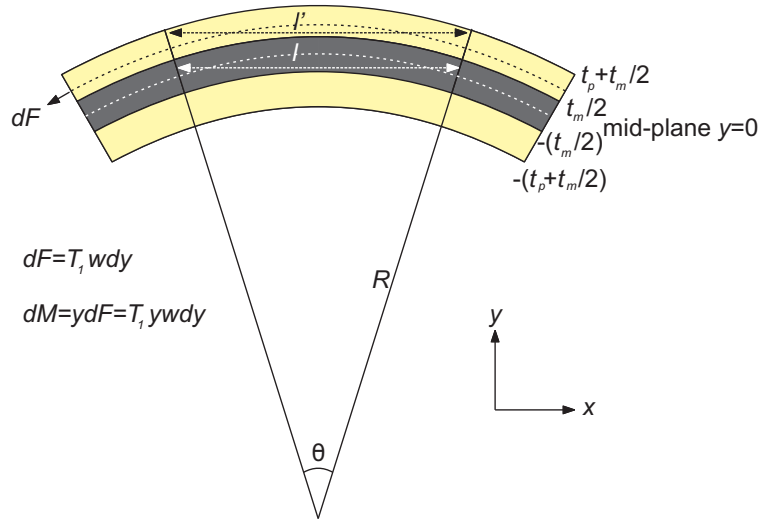


Figure 2.13: Bending deformation of a bimorph actuator [34].

$$T_{1,p} = E_p(\kappa y) \pm E_p d_{31} E_3 \quad (2.9)$$

$$T_{1,m} = E_m(\kappa y) \quad (2.10)$$

The moments in the actuator can be calculated by first determining that the differential moment is $dM = T_1 w dy$, where w is the actuator width. By using Equations 2.9 and 2.10, the total internal moment can be solved for by integrating throughout the width of the actuator. The resulting moment is given in Equation 2.11 [34].

$$M = E_p \kappa w \left(\frac{t_m^2 t_p}{2} + t_m t_p^2 + \frac{2t_p^3}{3} \right) + E_m \kappa w \frac{t_m^3}{12} - w E_p d_{31} E_3 (t_m t_p + t_p^2) \quad (2.11)$$

In order to solve for the free deflection of the tip, the external moments on the actuator are zero ($M = 0$). Therefore, Equation 2.11 can be set to zero. This constraint allows for the curvature of the actuator to be solved for, which is shown in Equation 2.12.

$$\kappa = \frac{6E_p d_{31} E_3 (t_m t_p + t_p^2)}{E_p (3t_m^2 t_p + 6t_m t_p^2 + 4t_p^3) + E_m t_m^3} \quad (2.12)$$

The deflection of the beam as a function of the position along the beam (x) and the curvature is given in Equation 2.13. Substituting for ($x = l$) and the curvature yields the free deflection at the tip of the actuator, which is given in Equation 2.14. [34]

$$v(x) = \frac{\kappa x^2}{2} \quad (2.13)$$

$$\delta_P = \frac{6E_p d_{31} E_3 (t_m t_p + t_p^2) l_p^2}{2E_p (3t_m^2 t_p + 6t_m t_p^2 + 4t_p^3) + E_m t_m^3} \quad (2.14)$$

The blocked force can also be solved for using beam theory. For a constant width, the displacement due to a force applied at the tip of the actuator is given in Equation 2.15

$$\delta_f = \frac{F_b l_p^3}{3E_p I} \quad (2.15)$$

The total deflection for the blocked force is zero, so $\delta_P = \delta_F$. Using this condition, the blocked force can be calculated in Equation 2.16.

$$F_b = \frac{3w(t_m + 2t_p)^2 E_p}{8l_p} \frac{2t_m/t_p + 1}{(t_m/2t_p + 1)^2} d_{31} E_3 \quad (2.16)$$

2.4.2 Lamination Theory Analysis for Bimorph Actuators.

Classical lamination theory can also be used to predict the behavior of piezoelectric bimorph bending actuators. Lamination theory uses the properties and stacking sequence of individual layers (lamina) within the laminate to determine the behavior of the multi-directional laminate. In order for the behavior of a laminate to be accurately predicted, the following assumptions and restrictions apply [7, p. 158]:

1. Each layer is quasi-homogeneous and orthotropic.
2. The laminate and each layer within are in a state of plane stress ($\sigma_z = \tau_{xz} = \tau_{yz} = 0$) because the lateral dimensions are much larger than the thickness.
3. The thickness of each layer is much larger than the displacements.
4. Throughout the laminate, displacements do not experience discontinuities.
5. In-plane displacements vary linearly with respect to the laminate thickness.
6. A line normal to the middle surface remains straight and normal after deformation.
7. Stress-strain relationships and strain-displacement relationships are linear.
8. Normal transverse strain, ϵ_z , is zero. Therefore the transverse displacement is independent of thickness.

Assumption 3 has questionable validity for the application to bimorph actuators because the expected tip displacements will be several times larger than the actuator thickness; the other assumptions seem reasonable for this analysis.

The mid-plane strains, ϵ^0 , and mid-plane curvatures, κ , can be expressed as a function of the lamina stiffnesses, thicknesses, stresses, and moments. For a piezoelectric actuator, this can be expressed according to Equation 2.17 [42]. The curvature is related to displacement by $d^2\delta(x)/dx^2 = \kappa_x$, where the displacement of the actuator is $\delta(x)$.

$$\begin{bmatrix} \epsilon^0 \\ \kappa \end{bmatrix} = \begin{bmatrix} A & B \\ B & D \end{bmatrix}^{-1} \left(\begin{bmatrix} N_{ext} \\ M_{ext} \end{bmatrix} + \begin{bmatrix} N_p \\ M_p \end{bmatrix} \right) \quad (2.17)$$

In Equation 2.17, $[A]$, $[B]$, and $[D]$ are the laminate stiffness matrices. These matrices are defined by the geometry, material properties, and stacking sequence of each layer. $[A]$, defined in Equation 2.18, is the extensional stiffness matrix, which relates in-plane loads

to in-plane strains. $[B]$ is the coupling stiffness, defined in Equation 2.19, which relates moments to in-plane strains and in-plane loads to curvatures. $[D]$, the bending stiffness matrix, relates moments to curvatures and is defined in Equation 2.20. $[Q]_n$ is defined as the local stiffness matrix, and $[\bar{Q}]_n$ is the global stiffness matrix for each layer. z is the height of each layer with respect to the midplane [7].

$$[A] = \sum_n [\bar{Q}]_n (z_n - z_{n-1}) \quad (2.18)$$

$$[B] = \frac{1}{2} \sum_n [\bar{Q}]_n (z_n^2 - z_{n-1}^2) \quad (2.19)$$

$$[D] = \frac{1}{3} \sum_n [\bar{Q}]_n (z_n^3 - z_{n-1}^3) \quad (2.20)$$

The effects of the piezoelectric ceramic on the midplane strains and curvatures are defined in Equations 2.21 and 2.22, respectively. Not only are the in-plane loads and moments from the piezoelectric effect a result of the geometry and stiffness of the laminate, but also the piezoelectric constants, d_{3j} , the electric field through the ceramic, E_3 , and the poling direction (1 or -1), p [42].

$$N_p = \sum_n [\bar{Q}]_n [d_{3j}] (z_n - z_{n-1}) E_3 p \quad (2.21)$$

$$M_p = \frac{1}{2} \sum_n [\bar{Q}]_n [d_{3j}] (z_n^2 - z_{n-1}^2) E_3 p \quad (2.22)$$

To simplify the nomenclature, the inverse of the combined stiffness matrix, $\begin{bmatrix} A & B \\ B & D \end{bmatrix}^{-1}$, can be defined as $[C]$. Combining this with Equation 2.17, the curvature of a piezoelectric actuator without a load, P , can be determined. When no external loads are applied, the free curvature and the actual curvature are equal ($P = \kappa_x$). The free curvature as a function of the applied electric field is defined in Equation 2.23. The free displacement (δ_P) of

an actuator with a piezoelectric ceramic length l_p can be determined using the curvature, which is shown in Equation 2.24. If a rigid extension of length l_{ext} is added to the tip of the actuator, then the displacement is defined in Equation 2.25, and the free displacement is calculated in Equation 2.26. The extension ratio, l_r , is defined as the ratio of the extension length to the length of the piezoelectric ceramic ($l_r = l_{ext}/l_p$) [42]. Figure 2.14 shows the different dimensions of a tapered actuator with an extension.

$$P(E_3) = C_{41}N_{x,p}(E_3) + C_{42}N_{y,p}(E_3) + C_{44}M_{x,p}(E_3) + C_{45}M_{y,p}(E_3) \quad (2.23)$$

$$\delta_P(l_p) = \frac{Pl_p^2}{2} \quad (2.24)$$

$$\delta(l_p) = \frac{Pl_p^2}{2} + \left. \frac{d\delta(x)}{dx} \right|_{x=l_p} l_{ext} \quad (2.25)$$

$$\delta_P(l_p) = \frac{Pl_p^2}{2}(1 + 2l_r) \quad (2.26)$$

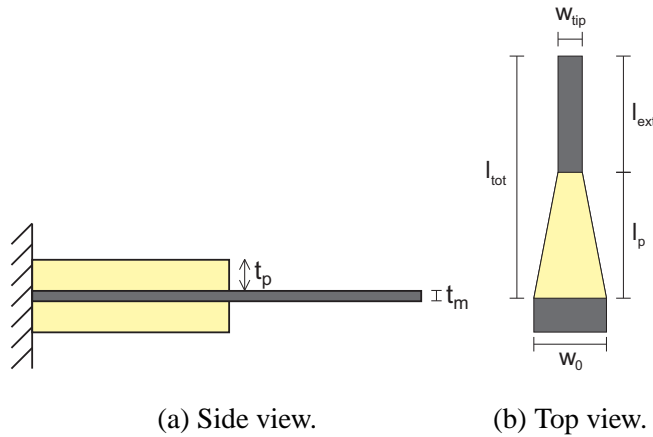


Figure 2.14: Piezoelectric bimorph actuator nomenclature.

If an external force is applied at the tip of the actuator, then an external moment, $M_x(x)$ is created. In this case the curvature is defined as $\kappa_x = P(E_3) + C_{44}M_x(x)$, which can be

written explicitly in terms of the external force, F , and the width profile, $w(x)$, as shown in Equation 2.27.

$$\frac{d^2\delta(x)}{dx^2} = P(E_3) - \frac{C_{44}F(l_p - x)}{w(x)} \quad (2.27)$$

The width profile can be expressed in terms of variables that allow for an easier comparison between actuators. For a trapezoidal width profile, these variables are the nominal width, w_{nom} , which is the width at $x = l_p/2$, and the width ratio, $w_r = w_0/w_{nom}$, where w_0 is the base width. Using this nomenclature, the width profile can be expressed as in Equation 2.28. For a rectangular actuator, the greatest strains are exhibited closest to the base. However, by tapering the actuator so that the base is wider than the tip (a width ratio greater than one), normalized peak strains can be reduced, as shown in Figure 2.15 [42].

$$w(x) = w_{nom} \left(\frac{2(l - w_r)}{l} x + w_r \right) \quad (2.28)$$

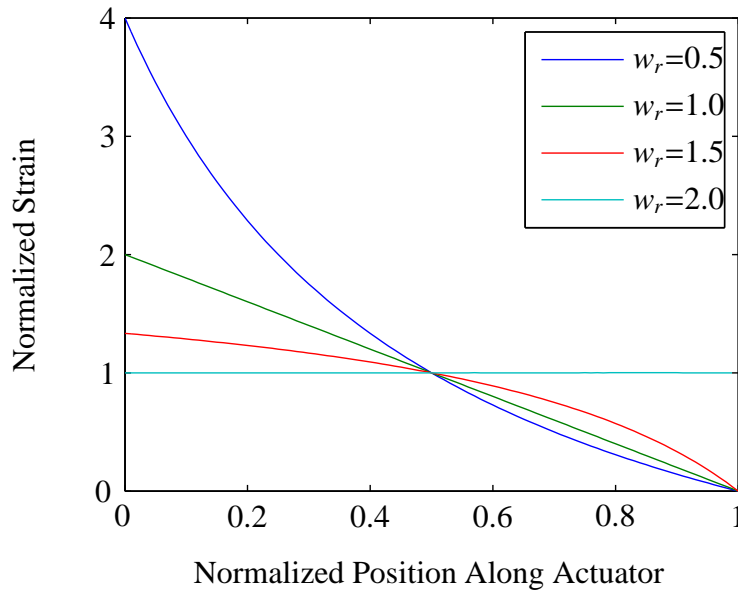


Figure 2.15: Effects of width ratio on normalized strain [42].

Combining Equations 2.27 and 2.28, yields Equation 2.29, which is an expression for the total curvature as a function of the geometry. The total curvature can be integrated twice at the boundary $x = l$ to solve for the displacement at the end of an actuator without a free extension, and the result is shown in Equation 2.30. The total curvature is a function of the free displacement, δ_P , and the displacement due to a force, δ_f [42].

$$\frac{d^2\delta(x)}{dx^2} = P(E_3) - \frac{C_{44}F}{w_{nom}} \left[\frac{l-x}{(2(1-w_r)/l)x + w_r} \right] \quad (2.29)$$

$$\delta(l) = \frac{Pl_a^2}{2} - \frac{C_{44}F}{w_{nom}} \left[\frac{(w_r-2)^2 \ln((2-w_r)/w_r) - 6 + 10w_r - rw_r^2}{8(1-w_r)^3} \right] \quad (2.30)$$

If a rigid extension is added, then the displacement due to an applied force can be determined by substituting Equation 2.30 in to Equation 2.25. The result for the displacement can be seen in Equation 2.31. $G_{l_{ext}}(w_r, l_r)$ is a function of both the length ratio and width ratio, and this parameter is defined as $G_{l_{ext}}(w_r, l_r) = (g_a + g_b)/g_c$, where g_a , g_b , and g_c are defined in Equations 2.32, 2.33, and 2.34 [42].

$$\delta_f(l + l_{ext}) = -\frac{C_{44}F_{ext}l^3}{3w_{nom}} G_{l_{ext}}(w_r, l_r) \quad (2.31)$$

$$g_a = 6(w_r - 1)(3 + rl_r - 2w_r - 4l_rw_r), \quad (2.32)$$

$$g_b = 3(-2 - 2l_r + w_r + 2l_rw_r)^2 \ln\left(\frac{2-w_r}{w_r}\right), \quad (2.33)$$

$$g_c = 8(1-w_r)^3 \quad (2.34)$$

The blocked force is defined as the force that the piezoelectric actuator produces when the total displacement is zero. Therefore, in order to solve for the blocked force, the free displacement and forced displacement should add to equal zero ($0 = \delta_P + \delta_f$). Using this constraint, and solving for the externally applied force, the blocked force is given in Equation 2.35 [42].

$$F_{b,ext} = \frac{3P(E_3)w_{nom}}{2C_{44}l_p} \frac{(1 + 2l_r)}{G_{l_{ext}}(w_r, l_r)} \quad (2.35)$$

Equations 2.26 and 2.35 can then be used to predict the free displacement and blocked force of a piezoelectric bimorph actuator of trapezoidal geometry. If the same type of piezoelectric material and carbon fiber are used so that the material properties are similar, then the design choices for creating different actuators can be summarized as in Table 2.4. These design choices are able to fully define the other design variables, such as the nominal width and extension ratio.

Table 2.4: Actuator design variables.

| Variable | Definition |
|-----------|----------------------------------|
| l_{tot} | Actuator Length |
| l_r | Extension Ratio |
| w_0 | Base Width |
| w_r | Width Ratio |
| t_p | Piezoelectric Layer Thickness |
| CF Layup | Carbon Fiber Passive Layer Layup |

However, the formulation for the blocked force does not provide a solution for a rectangular beam ($w_r = 1$), which makes a comparison to Euler-Bernoulli impossible. This can be corrected by setting $w(x)$ to a constant in Equation 2.27. By following the same process as above, the blocked force without an extension can be solved for using Equation 2.36.

$$F_b = \frac{P}{2} \frac{8w}{3C_{44}l_p} \quad (2.36)$$

2.5 Experimental Testing of Piezoelectric Actuators

In order to compare the analytical models described in Section 2.4 to the performance of real actuators, experimental testing of the actuators is necessary. Two results which can easily be compared to the models are the free displacement measurement and the blocked force measurement. Piezoelectric actuators could also be fully characterized by their performance under realistic loading conditions utilizing a mass-spring-damper system.

The free displacement of an actuator has been measured with both strain gauges and with optical sensors. Strain gauges have been placed on the actuators to measure the curvature and determine the tip displacement. However, difficulties were encountered with strain gauge wiring and the possibility of nonlinearities resulting from the presence of the strain gauges [41]. Therefore, optical measurement techniques were used which were non-intrusive to the system. Optical measurements of the displacement were taken by using the reflection of a laser off of the actuator tip to determine the free displacement, δ_p [31].

In addition to the free displacement, the blocked force that an actuator produces also helps to characterize the actuator. The blocked force has been measured by positioning the tip of the actuator in contact with a force sensor. As the actuator is excited, the sensor measures a force, F_1 . Since the sensor also deforms, a displacement, δ_1 , is measured optically. The blocked force, F_b , can then be calculated from Equation 2.37, which corrects for the small displacement of the sensor [31].

$$F_b = \frac{F_1}{1 - \delta_1/\delta_p} \quad (2.37)$$

Piezoelectric actuators have also been tested using a mass-spring-damper system that mimics realistic loads that would be encountered in flight. One technique to simulate these forces was to attach a small permanent magnet to the tip of the piezoelectric actuator. An electromagnet was situated close to the permanent magnet. A charge was then applied to simulate the thorax through a spring stiffness and drag through linear and nonlinear

damping [25]. While this approach definitely provided a more realistic loading scenario, this form of testing is unnecessary for comparing experimental results to the model predictions for displacement and blocked force. However, further testing of piezoelectric actuators would benefit from an analysis of the effects of realistic loading scenarios.

2.6 Statistical Analysis Techniques

After the data is acquired through experiments, statistical techniques are useful to determine if the results are statistically significant. Two techniques which can be utilized are hypothesis testing and reliability testing.

2.6.1 Hypothesis Testing.

In order to compare one or two sets of data to a known mean or to each other, hypothesis testing is useful. This form of analysis examines the possibility that two sets of data come from different means, and provides a p value that is a representation of this possibility. A t -test is a type of hypothesis testing that can compare two different sets of data to determine if the data has two different means. For a t -test, the test statistic can be calculated from Equation 2.38 [22].

$$t = \frac{\bar{x} - \bar{y}}{\sqrt{\frac{s_x^2}{n} + \frac{s_y^2}{m}}} \quad (2.38)$$

The p value is then defined as the probability of observing a test statistic that is more extreme than what was calculated. A low p value (less than 0.10 or 0.05) would show that the data came from different means, while a higher p value does not provide any significant information.

2.6.2 Reliability Testing.

Another important technique that is useful is reliability testing. Through reliability testing, the survival rate for the actuators under intense loading conditions can be predicted. The Weibull distribution, defined by the parameters λ and k , assumes that below a certain

value, such as zero, there is no physical chance of failure occurring. The cumulative distribution function for the Weibull distribution is given in Equation 2.39 [22].

$$F(x; \lambda, k) = 1 - e^{-(x/\lambda)^k} = P(X \leq x) \quad (2.39)$$

The cumulative distribution function is the chance of failure occurring at or below a certain value of x . The value x can be a maximum stress, time, number of cycles, or any other metric that describes a failure threshold. This equation can also be used to solve for the survivability, S , which is the percent of samples that will survive beyond a certain value. The survivability function is shown in Equation 2.40.

$$S(x) = P(X > x) = 1 - F(x) = e^{-(x/\lambda)^k} \quad (2.40)$$

2.7 Chapter Summary

Through the review of previous literature, a thorough understanding of the piezoelectric effect was used to understand analytical models which used either Euler-Bernoulli beam theory or classical lamination theory to predict the performance of bending bimorph actuators. Various experimental techniques were also examined to provide a basis for testing, and statistical analysis techniques were discussed that would help to examine the experimental data. Using this review of previous work as a background, the methodology used in this thesis is detailed in the next chapter.

III. Methodology

In the production of piezoelectric bending actuators, there are several design variables that can be used to create an actuator that has favorable characteristics in terms of output force, displacement, and weight. These design variables affect both the geometry and composition of the actuator. The geometry is modified by choosing the length, base width, width ratio, and extension length. The composition is determined by the selection of the piezoelectric ceramic thickness and the carbon fiber layup orientation. Through changing these variables, both analytically and experimentally and comparing results, the validity of the performance models was determined.

3.1 Preliminary Analytical Modeling

Analytical models for the performance of piezoelectric bimorph actuators in combination with a design of experiments were used to determine the predicted effects of each design parameter. First, the Euler-Bernoulli model and the composite lamination model, defined in Section 2.4, were compared for rectangular actuators in order to determine if there were any major differences between the two models. Then, the lamination theory model was used to determine the effects of varying the width of the actuator and adding a rigid extension to the tip of the actuator.

3.1.1 Comparison of Models for a Rectangular Beam.

In order to compare the Euler-Bernoulli model and the classical lamination theory model for rectangular actuators, several variables were modified that involved the type and size of the piezoelectric layer, the composition of the passive layer, and the geometry of the actuators. The variables that were changed are shown in Table 3.1. A full factorial design was utilized so that 729 (3^6) designs were analyzed for the free displacement, blocked force, and mechanical energy. The models were then compared by measuring the mean and

standard deviation of the percentage difference for the displacement, force, and mechanical energy, where the percentage difference is defined in Equation 3.1.

$$\% \text{ Diff} = \frac{X_{lam} - X_{E-B}}{X_{lam}} \quad (3.1)$$

Table 3.1: Model comparison factors.

| | Level 1 | Level 2 | Level 3 |
|---|----------|--------------|------------------|
| Young's Modulus, Piezo (GPa) | 80 | 76 | 59 |
| Piezoelectric Constant (m/V $\times 10^{-12}$) | 400 | 320 | 90 |
| Actuator Length (m) | 0.075 | 0.050 | 0.025 |
| Width (m) | 0.0075 | 0.0050 | 0.0025 |
| PZT Thickness (mm) | 0.267 | 0.191 | 0.127 |
| CF Layup (degrees) | [0/90/0] | [0/0/90/0/0] | [0/0/0/90/0/0/0] |

3.1.2 Predicted Effects of Design Variables on Actuator Performance.

The classical lamination theory model, which is outlined in Section 2.4.2, was used for further analysis because it allows for the width ratio and extension ratio to be modified for each actuator. This analysis does not take into account any non-linearities that may result from large strains or electric fields in the actuator. MATLAB was used to create a full-factorial design with three levels for each factor. The total length of the actuator and extension was set at 50 mm for simpler comparison. The values for each factor are shown in Table 3.2.

Using these factors as inputs into the model, 243 (3^5) different possible actuators were analyzed. JMP, a statistical and data analysis software package, was used to analyze the data using a design of experiments (DoE). Two utilities in JMP which were used were the

prediction profiler and the screening tool. The prediction profiler showed how each design variable affected each output parameter. If a model was used in which each variable was not changed individually, then the JMP algorithms calculated a prediction of what each effect was with confidence intervals. The screening tool showed if second-order effects could be anticipated by calculating which variables (or combination of variables) had a large effect on the outputs [13]. The JMP predictions for the preliminary model would be useful for narrowing the scope of actuator designs that need to be explored experimentally.

Table 3.2: Design of experiments factors.

| | Level 1 | Level 2 | Level 3 |
|-----------------------------|----------|--------------|------------------|
| Extension Ratio, l_r | 1 | 0.75 | 0.5 |
| Base Width, w_0 (mm) | 15 | 17.5 | 20 |
| Width Ratio, w_r | 1.5 | 1.625 | 1.75 |
| Piezo Thickness, t_p (mm) | 0.267 | 0.191 | 0.127 |
| CF Layup (degrees) | [0/90/0] | [0/0/90/0/0] | [0/0/0/90/0/0/0] |

3.2 Actuator Manufacture

After the analytical modeling was accomplished, experimental results were needed to verify the results. In order to accomplish this, custom actuators were manufactured out of active layers of Lead Zirconate Titanate (PZT-5H) and a passive layer of carbon fiber. These actuators were manufactured using two techniques to bond the piezoelectric ceramics to a passive layer, which used either Pyralux (a sheet adhesive produced by Dupont) with silver-conductive epoxy or uncured carbon fiber. In general, each technique used Corel Draw to create files that could be used to cut out layers of each material on an LPKF

Protolaser U. These layers were then assembled together by providing a combination of heat and pressure.

3.2.1 Construction Using Pyralux and Conductive Epoxy (Method 1).

The first technique that was used to manufacture actuators used Pyralux as a bonding agent between the carbon fiber and piezoelectric ceramic. This process is detailed below.

1. Using pre-impregnated carbon fiber, the desired layup for the passive middle layer was created. This carbon fiber was then pressed and heated in an LPKF Multipress S so that it would cure. The press applied 100 N/cm^2 of pressure at 192°C for 120 minutes. The specifications for each layer of carbon fiber are shown in Table 3.3.

Table 3.3: Carbon fiber material properties for a single cured layer.

| E_1 | E_2 | G_{12} | ν_{12} | ρ | $t_c f$ |
|-------|-------|----------|------------|-----------------|---------------|
| GPa | GPa | GPa | | kg/m^3 | μm |
| 420 | 5.51 | 4.83 | 0.25 | 1.39 | 61.8 |

2. The cured carbon fiber was then cut to the desired shape using the laser. This layer is the passive middle layer in the bimorph actuator. The Corel Draw file and corresponding carbon fiber cut out can be seen in Figure 3.1.
3. The Pyralux was then removed from its plastic backing, placed on a sheet of porous Teflon, and cut to the desired shape using the laser. This layer provides a means to bond the carbon fiber to the piezoelectric ceramics. However, since Pyralux is non-conductive, a small hole was cut out to allow for silver-conductive epoxy to provide an electrical connection between actuator layers. The conductive epoxy was produced by MG Chemicals, had an operating temperature between -30 and 90°C ,

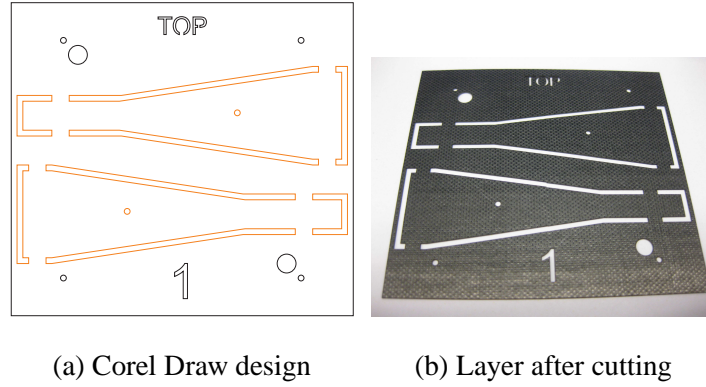


Figure 3.1: Carbon fiber layer manufacture.

and a volume resistivity of 0.38 ohm-cm at 25°C. Figure 3.2 shows the Corel Draw file and the resulting Pyralux layer used in this process, including the hole for the conductive epoxy.

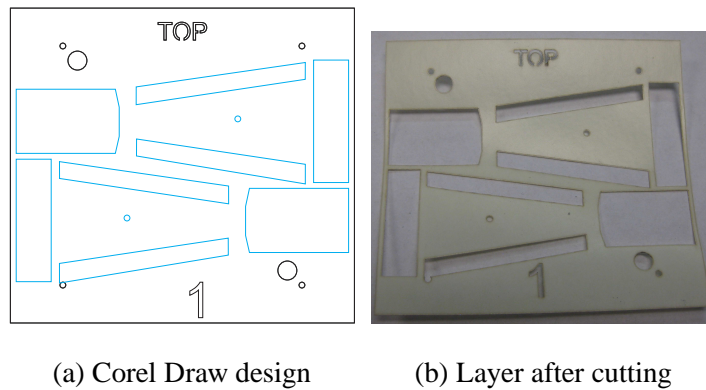


Figure 3.2: Pyralux layer manufacture.

4. The piezoelectric ceramic was scored using the laser, and then the individual actuator layers were carefully snapped off. The piezoelectric ceramics constitute the active layers in the bimorph actuator. The Corel Draw file, scored PZT sheet, and resulting actuator layer can be seen in Figure 3.3.

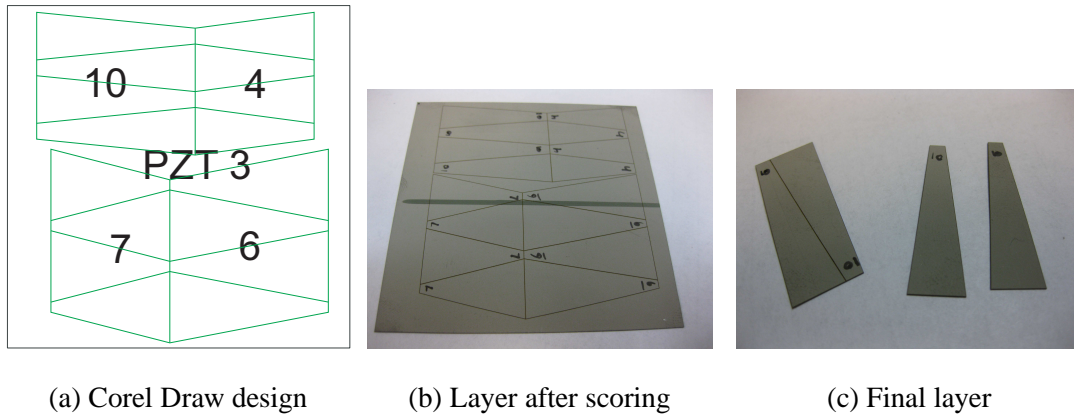


Figure 3.3: Piezoelectric layer manufacture.

5. Several layers of non-porous Teflon were cut out to act as a mold to hold the piezoelectric ceramics in place. Figure 3.4 shows the Corel Draw file used to cut out the Teflon, an individual piece of Teflon, and the open mold created from the Teflon. These layers not only ensure alignment of the ceramics, but also prevent the Pyralux and conductive epoxy from adhering to the clamp.

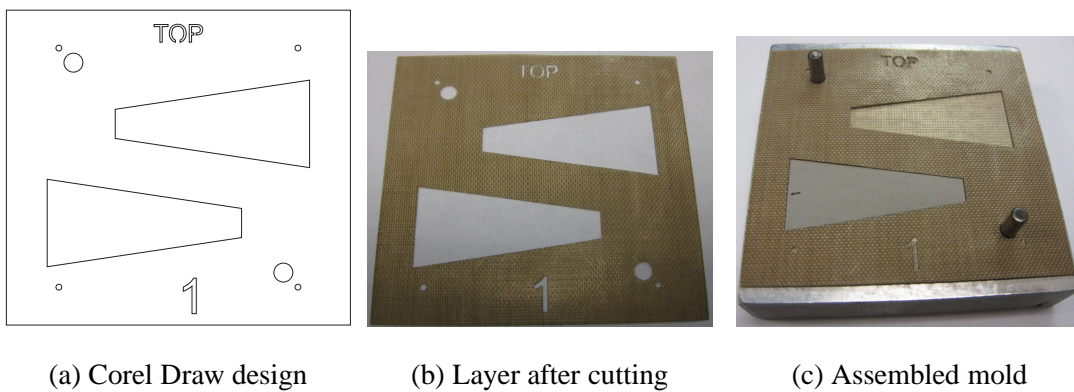


Figure 3.4: Teflon mold manufacture.

6. Felt and non-porous Teflon were also cut to cover the ends of the clamp. The non-porous Teflon prevented any leakage of the epoxy or Pyralux from reaching the felt, and the felt ends helped to prevent the fragile piezoelectric ceramic layers from cracking.

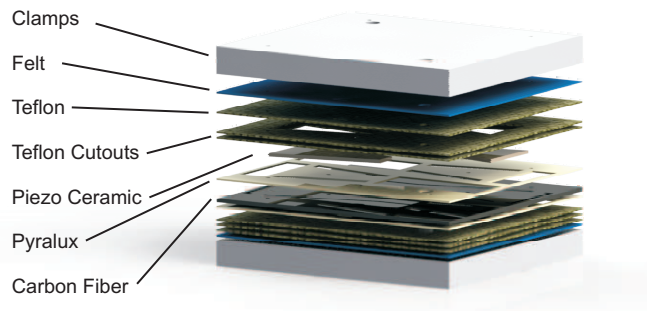


Figure 3.5: Actuator assembly, method one. Top half called out; bottom half symmetric.

7. Each layer was assembled in metal clamps, as shown in Figure 3.5. The piezoelectric ceramics needed to be poled in the same direction, with the positive pole facing up so that parallel or simultaneous driving methods could be used. With each layer of Pyralux, a small drop of silver conductive epoxy was added to ensure electrical conductivity. A 'C' clamp was then used to apply slight pressure. Sufficient pressure was required to ensure that the Pyralux would bond the layers; however too much pressure would fracture the piezoelectric ceramics. The entire assembly is placed in an Omegalux LMF-3550 oven, as seen in Figure 3.6, baked for one hour at 350 degrees Fahrenheit, and then allowed to cool.
8. After the entire assembly was cooled, the actuators were removed, and the assemblies resembled Figure 3.7. Each individual actuator was then cut out by hand, without the need to use the laser.



Figure 3.6: Clamp and actuator assembly in oven.

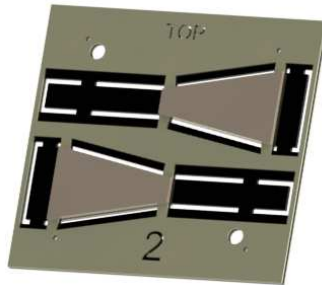


Figure 3.7: Assembled actuators, before cut out.

9. Wires were attached to the actuator using silver conductive epoxy. The white wire was attached to the carbon fiber base, the red wire to the positive poling direction, and the black wire to the negative poling direction. A heat gun was used so that the silver conductive epoxy would cure more quickly. Figure 3.8 shows the attached wires.

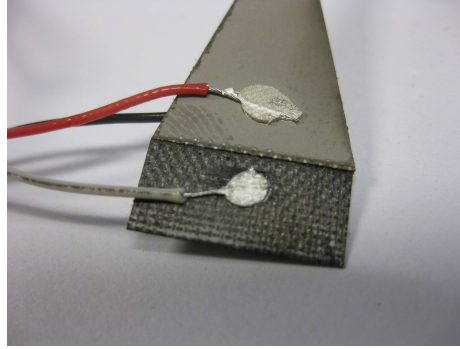


Figure 3.8: Wires connected to actuator.

3.2.2 Construction Using Uncured Carbon Fiber (Method 2).

1. Similar to method 1, the piezoelectric ceramic was scored using the laser, and then the individual actuator layers were carefully snapped off. These constitute the active layers in the bimorph actuator.
2. Several layers of non-porous Teflon were cut out to act as a mold to hold the piezoelectric ceramics and uncured carbon fiber in place. This can be seen in Figure 3.9.

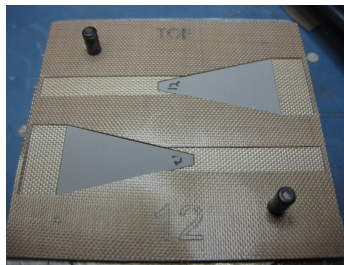


Figure 3.9: Teflon mold for construction method 2.

3. Felt, non-porous Teflon, porous Teflon, and a cotton bleeder cloth were also cut to cover the ends of the clamp. The non-porous Teflon prevented any leakage of the

epoxy, the porous Teflon allowed the epoxy to flow from the carbon fiber to the bleeder cloth, and the felt ends helped to prevent the fragile piezoelectric ceramic from cracking.

4. Using pre-impregnated carbon fiber, the desired layup for the passive middle layer was created. While still uncured, the desired shape for the passive layer was cut out using the laser to be placed in the Teflon mold, as shown in Figure 3.10.

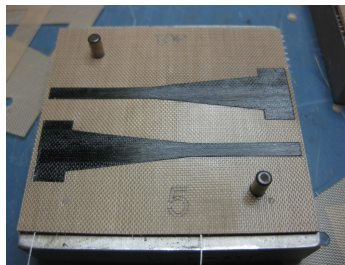


Figure 3.10: Uncured carbon fiber placed in Teflon mold.

5. Each layer was assembled in metal clamps, similar to method 1. The piezoelectric ceramics needed to be poled in the same direction, with the positive pole facing up. The carbon fiber was uncured; therefore there was not any need for Pyralux or conductive epoxy. Unlike method 1, a bleeder cloth was placed in the clamp as well to absorb excess epoxy. The final assembly in the clamps for this method can be seen in Figure 3.11. A ‘C’ clamp was then used to apply slight pressure. Enough pressure was required to ensure that the carbon fiber and epoxy will bond the layers; however too much pressure would fracture the piezoelectric ceramics. The entire assembly was baked for two hours at 350 degrees Fahrenheit in order to cure the carbon fiber epoxy, and then allowed to cool. After the entire assembly cooled, the actuators were removed.

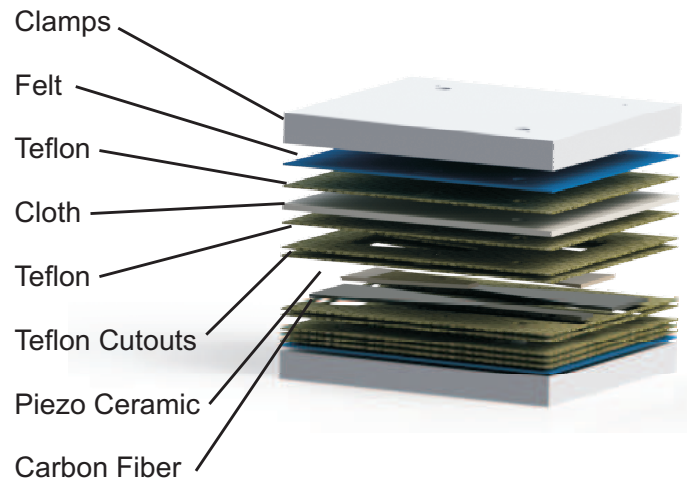


Figure 3.11: Actuator assembly, method two. Top half called out; bottom half symmetric.

6. Wires were attached to the actuator using silver conductive epoxy. The white wire was attached to the carbon fiber base, the red wire to the positive poling direction, and the black wire to the negative poling direction. A heat gun was used so that the silver conductive epoxy would cure more quickly.

3.3 Preliminary Model Validation

Preliminary experimental testing was accomplished with the goal of validating the trends of the analytical model and modifying the model, if necessary, to reflect the experimental data. In order to accomplish this, the mass, free displacement, and blocked force were measured for each actuator. The mass of each actuator was measured without wires attached using an Ohaus Voyager PRO balance, which has a resolution of 0.1 mg and a maximum capacity of 210 grams.

Each actuator was then excited using the voltage output from a Trek amplifier, which received a signal from a National Instruments USB-6229 multifunction input/output box that was controlled via MATLAB. The input/output box could provide ± 10 V, which was then amplified by a factor of 30 by the Trek amplifier. This means that the maximum driving voltages were ± 300 V.

The actuators were manually positioned using micro-manipulators so that the displacements and forces could be accurately measured. Figure 3.12 shows the entire setup used for testing. For the preliminary testing, the actuators were excited using the parallel, non-simultaneous driving technique (see Section 2.3.3).

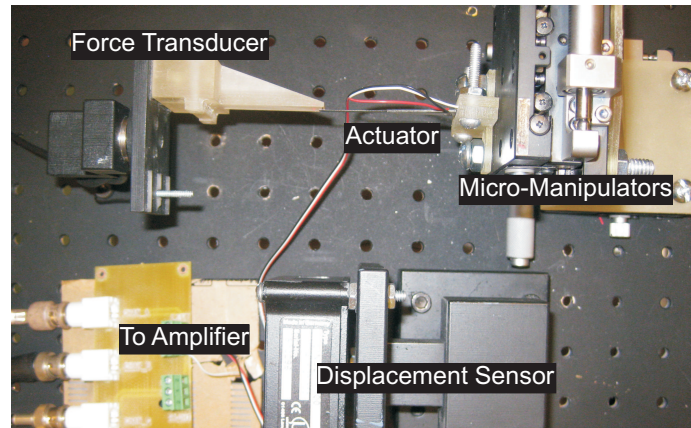


Figure 3.12: Experimental testing setup.

3.3.1 Actuator Designs Used.

For the preliminary testing, the primary goal was to validate the analytical model. Instead of making one actuator for every possible combination of design variables, a design of experiments approach was used so that twelve different actuators could be created to determine the first-order effects of each variable. For the preliminary testing, this was accomplished by using the specifications in Table 3.4 and the first manufacturing method, which used Pyralux and silver-conductive epoxy.

3.3.2 Free Displacement Measurement.

In order to measure the free displacement of each actuator, the base was clamped so that the actuator was free to move at the tip. Using micro-manipulators, the tip of the actuator was placed within the focal range of the displacement sensor. The displacement

Table 3.4: Preliminary actuator designs.

| Design | l_{tot} | l_r | w_0 | w_r | t_p | CF Layers |
|--------|-----------|-------|-------|-------|-------|-----------|
| | mm | | mm | | mm | |
| 1 | 50.0 | 0.5 | 20 | 1.5 | 0.127 | 5 |
| 2 | 50.0 | 1 | 20 | 1.5 | 0.191 | 7 |
| 3 | 50.0 | 1 | 15 | 1.5 | 0.127 | 7 |
| 4 | 50.0 | 1 | 15 | 1.5 | 0.267 | 3 |
| 5 | 50.0 | 0.5 | 15 | 1.75 | 0.191 | 3 |
| 6 | 50.0 | 0.5 | 20 | 1.75 | 0.267 | 7 |
| 7 | 50.0 | 1 | 20 | 1.75 | 0.267 | 5 |
| 8 | 50.0 | 0.5 | 20 | 1.5 | 0.191 | 3 |
| 9 | 50.0 | 0.5 | 15 | 1.75 | 0.127 | 7 |
| 10 | 50.0 | 0.5 | 15 | 1.5 | 0.267 | 5 |
| 11 | 50.0 | 1 | 15 | 1.75 | 0.191 | 3 |
| 12 | 50.0 | 1 | 20 | 1.75 | 0.127 | 5 |

sensor used in testing was a Micro-Epsilon optoNCDT 1800 optoelectronic displacement measurement system. This measurement system, which has a resolution of 2 micrometers, works by using optical triangulation by projecting a modulated point of light onto the target surface and measuring the intensity of the reflection [21]. An example of how the actuator was setup for free displacement measurement can be seen in Figure 3.13.

During testing, each actuator was excited with voltage that increased linearly from -50 V to +50 V. The goal of this testing was to determine the relation between the applied voltage and the free displacement, which could then be compared with the

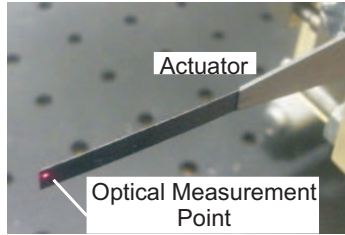


Figure 3.13: Actuator during free displacement measurement.

analytical model predictions. The applied ± 50 V should be below the expected failure of the piezoelectric ceramics while still providing enough data determine the voltage-displacement relationship.

3.3.3 *Blocked Force Measurement.*

The blocked force was measured using the same clamps as the free displacement, but the actuator was prevented from moving in one direction. The force that the actuator applied to the test stand was measured using an ATI Nano-17 Titanium Force/Torque Sensor. The Nano-17 has a resolution down to 0.149 gram-force, or 1.46 millinewtons [3]. In order to calculate the blocked force, any significant displacement should have been measured so that Equation 2.37 could be used. However, any tip displacement that resulted from this testing was below the resolution of the optoNCDT 1800, so the displacement was assumed to be zero. Any displacement away from the tip of the actuator was not taken into account for the blocked force calculation. The setup for this test can be seen in Figure 3.14.

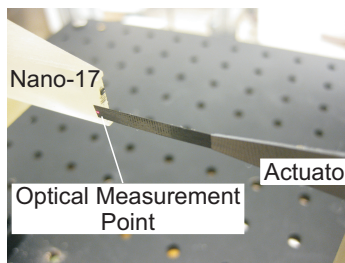


Figure 3.14: Actuator during blocked force testing.

For each blocked force test, the voltage was varied similar to the free displacement test, from ± 50 V. However, only the results from either the positive or negative voltage were relevant. In order to determine if different poling directions had different results, the actuator was flipped around and tested again so that the results could be compared.

3.4 Secondary Force and Displacement Testing

After the preliminary testing, more actuators were created without the use of Pyralux using the second manufacturing method, detailed in Section 3.2.2. Testing was accomplished for both the free displacement and blocked force once again.

The free displacement and blocked force testing were accomplished using the same setup as before. However, the excitation voltage for the blocked force testing was now varied in a stair step fashion so that a time average could be taken at each step of the force to minimized the effect of noise in the results. An example of the excitation voltage for the blocked force testing is given in Figure 3.15. Also, in addition to the parallel

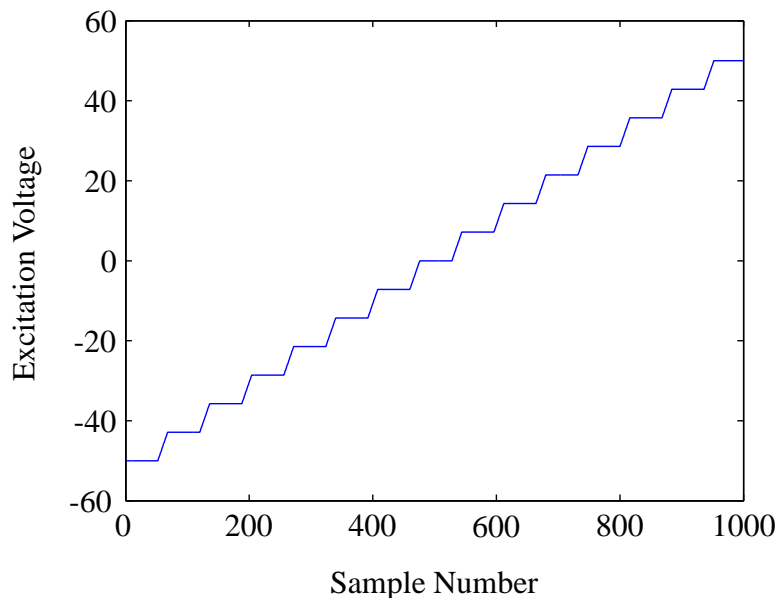


Figure 3.15: Improved excitation voltage for blocked force testing.

driving methods that were used in the preliminary testing, simultaneous driving methods were also used in this testing. The purpose of using both driving methods was to determine if the driving method affected the actuator output, and if so, what the effects were. At lower electric fields, the two driving methods should produce similar results. However, at higher electric fields the simultaneous driving method was expected to show less hysteresis because the electric fields are applied parallel to the poling direction of the piezoelectric ceramics (see Section 2.3.3).

3.4.1 Primary Effects Testing.

Using the revised methods for manufacturing and testing, the first set of testing recreated the same actuators used in the preliminary testing, detailed in Table 3.4, and tested them under the same conditions to confirm the effects of changing the design variables of each actuator.

3.4.2 Width Effects Testing.

All of the actuators used in the preliminary testing and primary effects testing used actuators that had a base width of either 20 mm or 15 mm and a piezoelectric length of 25 mm or 33.3 mm. This means that the ratio of the base width to the piezoelectric length ($\frac{w_0}{l_p}$) ranges from 0.45 to 0.8. However, the actuators created by the Harvard Micro-robotics Lab, where the original model was developed, had a ratio of around 0.2 [42]. In order to determine if any differences were from the width effects, eight more actuator designs were created and tested, the dimensions of each are in Table 3.5.

3.4.3 Rectangular Actuator Testing.

One of the main objectives of this research is to find an optimal actuator design. In order to determine how much improvement tapered actuators with an extension have over standard rectangular actuators, the performance of standard rectangular actuators must also be analyzed. Therefore, the actuators detailed in Table 3.6 were manufactured and tested to determine their performance characteristics.

Table 3.5: Width variation actuator designs.

| Design | l_{tot} | l_r | w_0 | w_r | t_p | CF Layers |
|--------|-----------|-------|-------|-------|-------|-----------|
| | mm | | mm | | mm | |
| 13 | 50.0 | 1 | 3.5 | 1.5 | 0.267 | 5 |
| 14 | 50.0 | 1 | 3.5 | 1.75 | 0.267 | 5 |
| 15 | 50.0 | 1 | 5.0 | 1.5 | 0.267 | 5 |
| 16 | 50.0 | 1 | 5.0 | 1.75 | 0.267 | 5 |
| 17 | 50.0 | 1 | 7.0 | 1.5 | 0.267 | 5 |
| 18 | 50.0 | 1 | 7.0 | 1.75 | 0.267 | 5 |
| 19 | 50.0 | 1 | 9.0 | 1.5 | 0.267 | 5 |
| 20 | 50.0 | 1 | 9.0 | 1.75 | 0.267 | 5 |

Table 3.6: Rectangular actuator designs.

| Design | l_{tot} | l_r | w_0 | w_r | t_{PZT} | CF Layers |
|--------|-----------|-------|-------|-------|-----------|-----------|
| | mm | | mm | | mm | |
| 21 | 32.0 | 0 | 15.0 | 1 | 0.127 | 3 |
| 22 | 32.0 | 0 | 10.0 | 1 | 0.127 | 3 |
| 23 | 40.3 | 0 | 15.0 | 1 | 0.127 | 3 |
| 24 | 40.3 | 0 | 10.0 | 1 | 0.127 | 3 |

3.5 Operating Range Testing

Each actuator that did not fail during the previous testing was retested to determine the maximum stress, strain, and electric field that the bimorph actuators achieved before

failure. This testing was the key to optimizing the bimorph actuators for size and weight because an actuator that could be driven at a higher voltage or withstand a greater load would most likely be the optimal design choice. Testing for the maximum stress was accomplished in a similar manner to the blocked force testing, and testing for the maximum strain was accomplished in a manner similar to the free displacement testing. By comparing the maximum stress, strain, and electric field at failure for each actuator, a reliable operating range for the actuators could be determined. Also, the effects of previous loading, known as hysteresis, can be investigated in this testing.

In order to determine the appropriate operating ranges in regards to the stresses, strains, and electric fields, the data was assumed to follow a Weibull Distribution, detailed in Section 2.6.2. After the Weibull parameters were determined, Equation 2.40 was solved for the threshold values that yield various survival percentages, which can be seen in Equation 3.2.

$$x = \lambda (-\ln(S))^{1/k} \quad (3.2)$$

3.5.1 Maximum Stress Testing.

Maximum stress was determined using the same experimental setup as the blocked force testing, which is detailed in Section 3.3.3. This test setup was used because in free displacement testing, the stresses in the piezoelectric layer do not vary with the width profile, but blocked force testing causes a moment to be generated in the actuator that varies the stress throughout the length of the actuator. This variation in stress is the driving theory behind tapering the width profile, which is detailed in Section 2.4.2.

The difference between the failure testing and the blocked force testing previously accomplished is that for the failure testing the voltage was continuously increased until the piezoelectric actuator failed. The point of failure was apparent because the applied force dramatically dropped to zero.

The maximum stress that caused the actuator to fail can be determined by using the maximum blocked force and the actuator geometry. Equation 3.3 gives the failure stress as a function of the blocked force at the end of a rigid extension ($F_{b,ext}$), the width ($w(x)$), and the distance from the base of the actuator (x). For any actuator that has a width ratio less than 2.0, the maximum strain, and hence stress, occurs at $x = 0$. This simplifies the equation for stress further.

$$\sigma_x(x) = \frac{M_x(x)(t/2)}{(1/12)t^3} = \frac{6F_{b,ext}(l_{ext} + (l_p - x))}{w(x)t^2} = \frac{6F_{b,ext}l_{tot}}{w_0t^2} \quad (3.3)$$

3.5.2 Maximum Strain Testing.

The determination of the maximum strains on the actuators was accomplished using the same experimental setup as the free displacement testing, which is detailed in Section 3.3.2. The free displacement setup was used because there are no external forces on the actuator, which means the strains would not be influenced from an outside load.

The difference between this testing and the free displacement testing was that in the free displacement testing the voltage was varied between two values that were not expected to cause failure. However, with the maximum strain testing, the voltage was increased by slowly increasing the amplitude of an oscillating voltage, which is described in Equation 3.4, where $A(t)$ is a linearly increasing amplitude, t is the time, and ω is the frequency of the oscillating function.

$$V(t) = A(t) \sin(\omega t) \quad (3.4)$$

Once the maximum strain was reached, the measured displacement dramatically dropped off. The maximum strains in the piezoelectric layer were determined from the maximum free deflection. Equation 3.5 gives the general equation for strain in any laminate layer as a function of the distance from the midplane, z [7].

$$\epsilon_x = \epsilon_x^o + z\kappa_x \quad (3.5)$$

The curvature, κ_x , could be determined from rearranging Equation 2.26, which yielded Equation 3.6. The maximum strain occurred at the maximum height through the thickness, z_{max} , which is calculated from Equation 3.7.

$$\kappa_x = \frac{2\delta_p}{l_p^2 (1 + l_r)} \quad (3.6)$$

$$z_{max} = \frac{1}{2}t_{cf} + tpzt \quad (3.7)$$

For parallel driving methods, the midplane strain, ϵ_x° , was zero because the two piezoelectric layers counter the extensional strains. However, if a simultaneous drive method was used then the midplane strain could be estimated from the applied voltage and published d_{33} coefficient using Equation 3.8.

$$\epsilon_x^\circ = d_{33} (E_{3,upper} + E_{3,lower}) = d_{33} \frac{V_{upper} + V_{lower}}{t_p} \quad (3.8)$$

By inserting Equations 3.6, 3.7, and 3.8 into Equation 3.5, the maximum strain in the piezoelectric layer can be solved as a function of the measured displacement, actuator dimensions, piezoelectric constant, and applied voltage. Equation 3.9 gives the final calculation of the maximum strain.

$$\epsilon_x = d_{33} \frac{V_{upper} + V_{lower}}{t_p} + \left(\frac{1}{2}t_{cf} + t_p \right) \frac{2\delta_p}{l_p^2 (1 + l_r)} \quad (3.9)$$

3.5.3 Hysteresis Analysis.

Since testing for the maximum strain and voltage field drives the actuator using an oscillating voltage with increasing amplitude, the effects of hysteresis were also measured. Hysteresis can be observed by noting changes in the strains that result from the same applied voltage field after a stronger field was applied. Since one of the goals of a simultaneous driving technique was to minimize the effects of hysteresis, the two different driving techniques, parallel and simultaneous, were compared to observe whether there was a change in hysteresis effects between the two.

3.6 Manufacturing Analysis

Two methods of manufacturing the actuators were used. Method one utilized cured carbon fiber with Pyralux and conductive epoxy. Method two used uncured carbon fiber, and therefore did not require Pyralux or conductive epoxy. While the first method made construction easier because uncured carbon fiber can be difficult to handle, the repeatability and reliability differences between the two methods required investigation. In order to compare the different manufacturing methods, the number of successful actuators created without defects was compared for each manufacturing process. Also, the ultimate failure modes of the actuators were compared so that the improvements from one method to the other could be determined.

3.7 Final Optimization

Two parameters that could be used to define the requirements for an actuator are the maximum blocked force and maximum free displacement. Since the linkage that transmits the power from the actuator to the wing can be modified for different transmission ratios, as detailed in Section 2.3.4, a more appropriate measure for an actuator is the mechanical energy, which is a combination of the free displacement and blocked force. If the mechanical energy required to flap the wings on a FWMAV is known, then an optimized actuator can be created to meet these requirements by using the analytical model that has been corrected to match the experimental data.

Two ways in which the actuators could be optimized are through an exhaustive search method, which searches for the best actuator by looking at every combination of design variables, or a multivariate numerical optimization algorithm. While the multivariate numerical optimization routine would most likely be faster due to a smaller number of calculations, the numerical optimization has a chance to miss the best solution or fail to converge altogether [5]. The search method, while slower, guarantees that the best solution would be found, assuming that the search grid has a small enough resolution. The time

required to run a single simulation for an actuator is extremely small; therefore the search method is more appropriate for this application since the extra time required would not be too great.

3.8 Chapter Summary

This chapter discussed the analytical analysis comparing two models, different manufacturing techniques, actuator designs, experimental procedures, and design optimization. Through the analytical analysis, the differences of the Euler-Bernoulli and lamination theory model could be compared, which allowed for the selection of an appropriate model to use in further analysis. Constructing various actuators using different methods would allow the manufacturing methods to be analyzed and actuators to be constructed for further testing for blocked force, free displacement, and maximum operating ranges. This testing allows for the model to be compared to the experimental results, which can then be optimized through a search optimization routine. The results and analysis from this testing are detailed in the next chapter.

IV. Analysis and Results

4.1 Preliminary Analytical Modeling

4.1.1 *Comparison of Models for a Rectangular Beam.*

The first step in optimizing the piezoelectric actuators was to compare existing analytical models that used either lamination theory or Euler-Bernoulli beam theory to determine if there were any major differences. Table 3.1 shows variables were changed, as well as the range of each variable. As Table 4.1 shows, while there were differences that were on average slightly above 10% for the free displacement and blocked force for each model, the orders of magnitude were equivalent. Also, the total mechanical energy only had an average of less than 5% difference. This shows that regardless of the materials used, the predicted outputs for a rectangular actuator from both models roughly agreed. However, a variation with width could not be taken into account with the Euler-Bernoulli model. Therefore, the classical lamination theory model was more appropriate for the preliminary modeling of tapered actuators.

Table 4.1: Percent difference between lamination theory and Euler-Bernoulli

| | Mean % Difference | Standard Deviation |
|-------------------|-------------------|--------------------|
| Free Displacement | 15.0% | 9.87% |
| Blocked Force | -12.4% | 0.0497% |
| Mechanical Energy | 4.42% | 11.1% |

4.1.2 *Predicted Effects of Design Variables on Actuator Performance.*

Since the classical lamination theory model was more appropriate for the initial modeling, this model was used to determine the effects of different design variables on the

actuator performance. Ideally, only first-order changes would be apparent in the actuator output so that there would not be any coupling between different design variables. This would simplify analysis and optimization. Both the effects of each design variable and the relevance of second-order effects were determined from a design of experiments (DoE) analysis using the analytical lamination theory model.

The DoE approach first showed the effects of changes in each design variable on the output parameters in the prediction profiler, which can be seen in Figure 4.1. These results show which variables had the greatest effects on the design performance, as well as if changes in the design variables produced linear or non-linear effects. For example, a thicker piezoelectric layer increased the blocked force of an actuator, but decreased the free displacement. Another important result is that all of the effects appeared to be linear, with the exception of how the carbon fiber layup affected the free displacement of the actuator, which appeared to be slightly curved. Finally, the width profile did not have any effect on the free displacement, apparent by an examination of Equation 2.26, which is not a function of the width of the actuator.

The relative magnitude of first and second-order effects was also determined from this analytical DoE using the screening tool in JMP. Figure 4.2 shows the scaled estimates of the effects of each of the first and second-order effects. Scaled estimates are the coefficients which correspond to the effect of each factor which are normalized to have a mean of zero and a range of two [13]. For the analytical lamination theory model, the DoE approach showed that second-order effects did not play a large role in the performance of each actuator.

Since first-order effects played a much larger role than second-order effects, experimental testing could employ a partial factorial DoE, as opposed to a full factorial. For a partial factorial, second-order (and higher) effects were aliased with first-order effects so that only a subset of all possible actuators needed to be tested [13]. Using a partial factorial

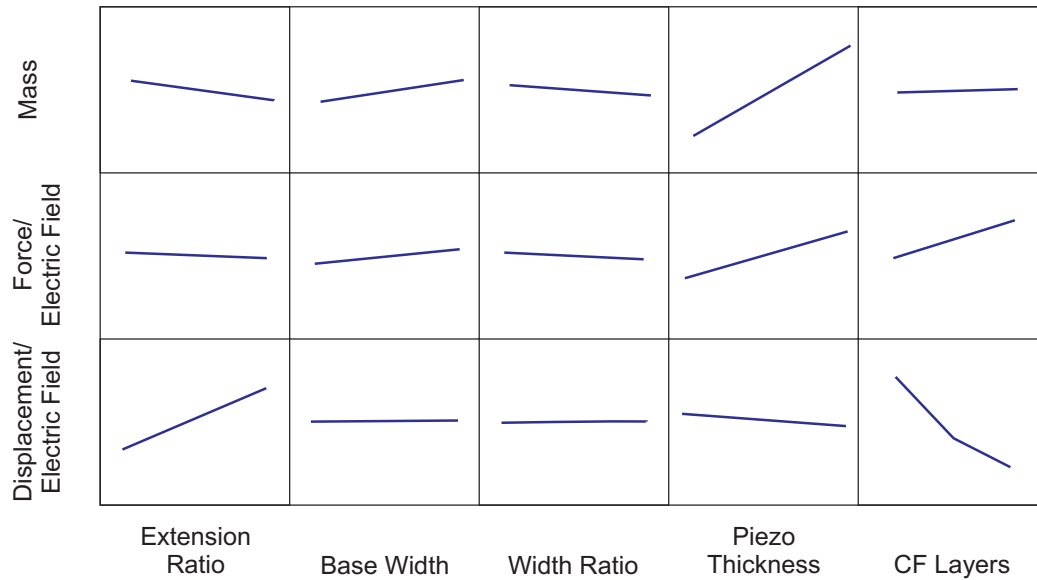


Figure 4.1: Predicted effects of design variables on output parameters.

changed the number of designs needed by at least an order of magnitude, which reduced the number of experimental tests that needed to be run.

4.2 Preliminary Actuator Testing

Using the actuator designs that were selected with the design of experiments and created with the first manufacturing method, which used Pyralux and conductive epoxy, free displacement testing was accomplished as described in Section 3.3.2 and the blocked force testing was accomplished as described in Section 3.3.3. Originally, each of the twelve actuator designs was to be manufactured twice, for a total of twenty-four different actuators. This group of actuators would provide a large enough sample size to reasonably compare the experimental results to the results predicted by the original lamination theory model. However, due to problems in the manufacturing process, only ten of the actuators were able to be measured for mass and only five of those were able to be tested for displacement and four for force in this phase of testing. The problems with the manufacturing process will be described in Section 4.9.

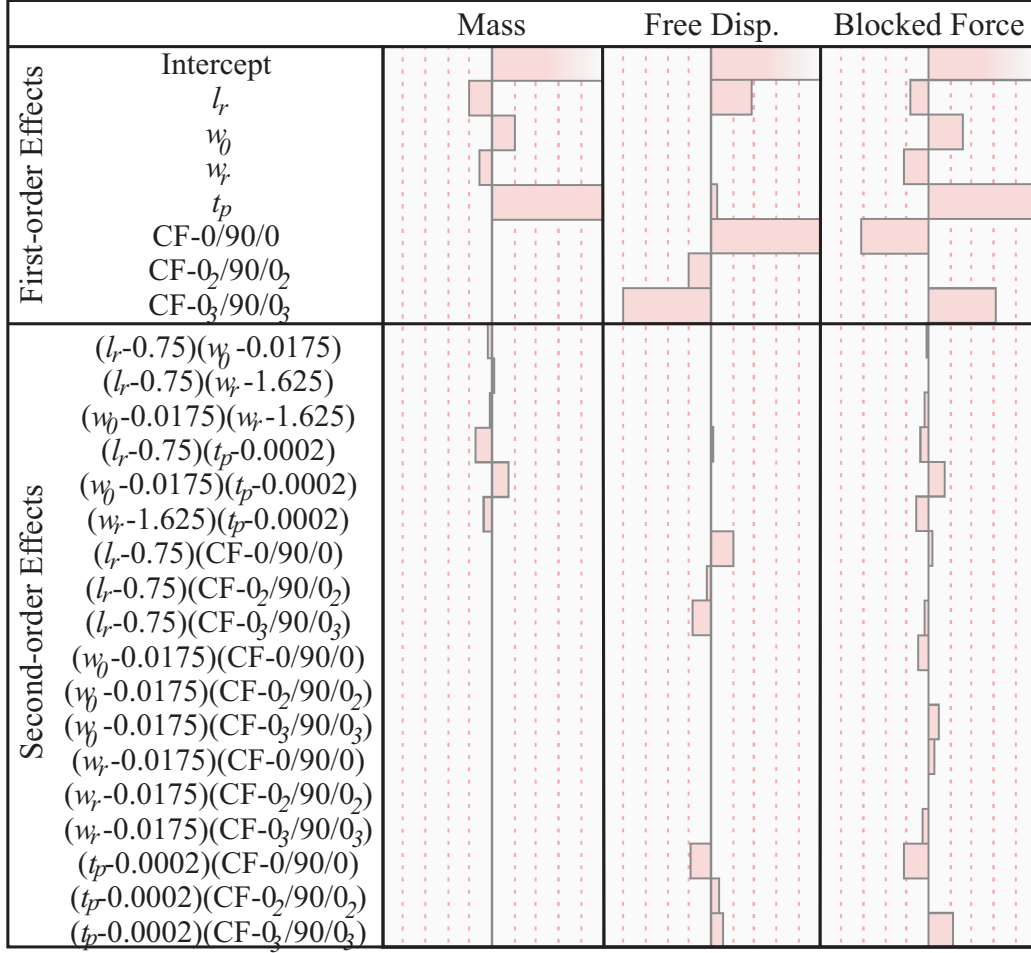


Figure 4.2: Scaled estimates of first and second-order effects.

4.2.1 Actuator Mass Results.

For each actuator that was manufactured with all of the components properly adhered (cracking was ignored), the mass of each actuator that was measured experimentally and the predicted mass from the lamination theory model are given in Figure 4.3. The predicted mass was calculated by determining the volume of the piezoelectric ceramic and the carbon fiber, and then multiplying by the respective densities. These results show that the masses did seem to correlate well between what the lamination theory model predicted and what the actuators actually weighed.

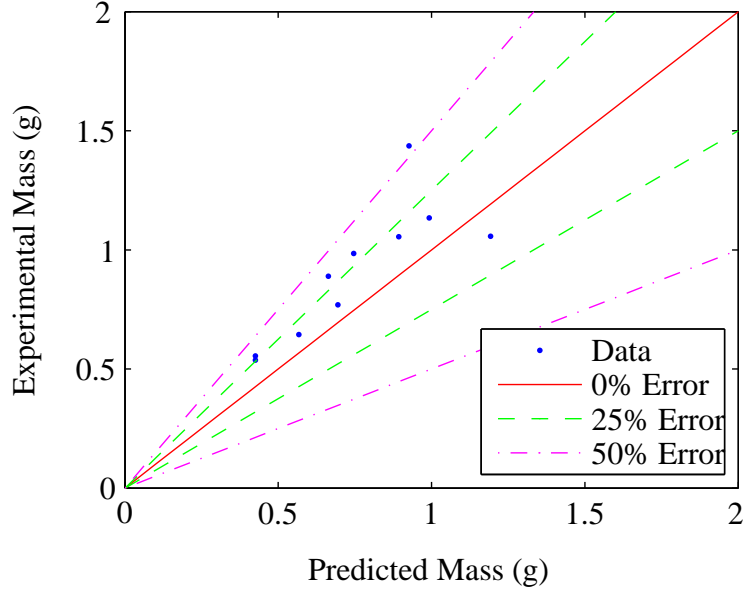


Figure 4.3: Actuator mass, experimental vs. modeled.

In order to make these comparisons easier, a correction factor, k was used to adjust the modeled data so that the experimental and modeled data would have similar means. The correction factor k could also be useful to determine the difference between the mean experimental and modeled results. The calculation for the correction factor is given in Equation 4.1, where N is the total number of samples for some result, X . If a perfect match was achieved, then the k value would be one. For the actuator mass, the k correction was 0.833.

$$k_X = \frac{1}{N} \sum_{i=1}^N \frac{X_{\text{model},i}}{X_{\text{experimental},i}} \quad (4.1)$$

By dividing the modeled data by the correction factor, the experimental and modeled data could again be plotted to better determine if the trends predicted by the model held true. The corrected lamination theory model data versus the experimental data are displayed in Figure 4.4. By using the correction factor, the modeled data did seem to fit the experimental

data much better. Further testing could show if the correction factors were applicable to empirically fit the models to reality.

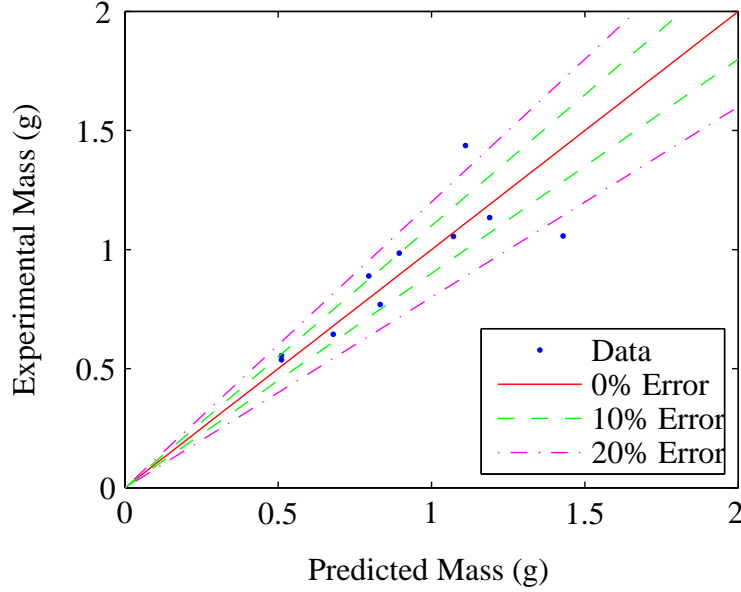


Figure 4.4: Actuator mass, experimental vs. modeled (corrected).

In order to determine how well the correction factor fitted the modeled data to the experimental data, the standard deviation of the ratio of modeled to experimental data was calculated from Equation 4.2. For the actuator mass, the standard deviation for the correction factor was 0.130. This standard deviation appeared quite small, which indicates that the lamination theory model did seem to predict trends that were observed experimentally.

$$s_X = \sqrt{\frac{1}{N-1} \sum_{i=1}^N (\theta_i - \bar{\theta})^2}, \text{ where } \theta_i = \frac{X_{\text{model},i}}{X_{\text{experimental},i}} \quad (4.2)$$

4.2.2 Free Displacement Results.

For each of the actuators that was tested, the free displacement was plotted against the applied voltage. On the same axis, the displacement predicted by the analytical lamination

theory model was also plotted to qualitatively show the difference between the experimental and analytical results. Figure 4.5 shows an example for actuator design 6.

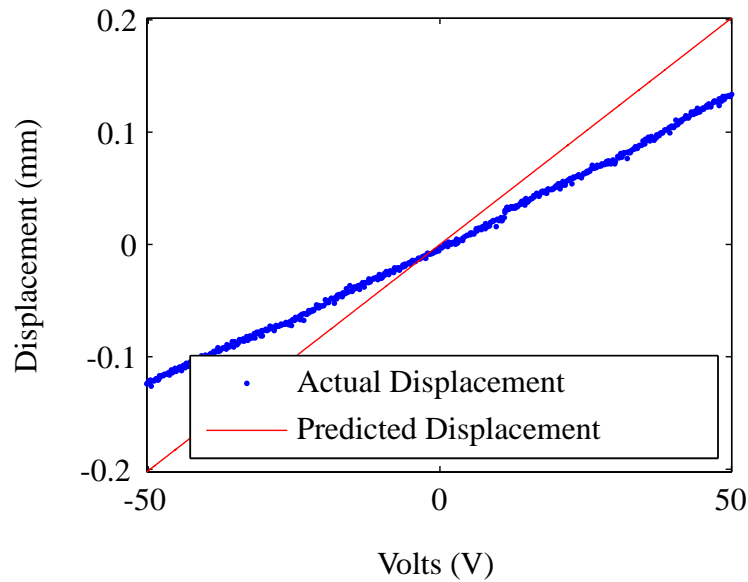


Figure 4.5: Sample free displacement plot, experimental and modeled.

The results of the free displacement testing showed that both the experimental and predicted free displacement vary linearly with voltage for the range tested. Therefore, an appropriate figure of merit to compare the two displacements would be the slope of a linear curve fit of the experimental and analytical data. Figure 4.6 shows a comparison of the slope for the experimental and modeled data for each actuator that was tested.

The displacement results showed that for every actuator produced, the modeled displacement exceeded the displacement that was achieved experimentally. One possible explanation is that the use of Pyralux and conductive epoxy changed properties of the actuator that are not accounted for in the lamination theory model. For example, the conductive epoxy may not have been providing charge to the entire piezoelectric layer evenly, the passive layer may have had a different stiffness than the lamination theory model

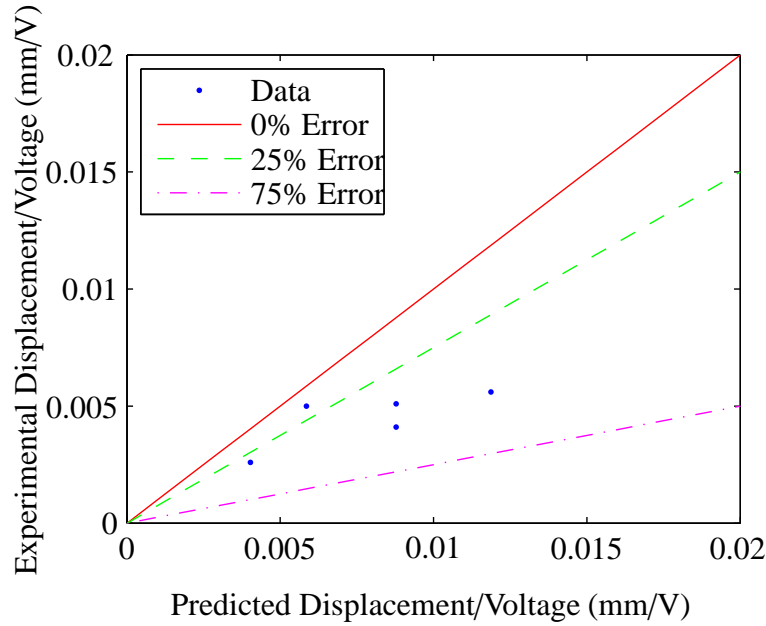


Figure 4.6: Displacement/voltage, experimental vs. modeled.

predicted, or the Pyralux did not bond the layers perfectly and prevented the actuator from functioning properly.

Despite the small sample size and large difference between the experimental and modeled data, some qualitative comparisons could still be made using the k correction. For the preliminary free displacement results, the k correction factor was 2.72. After the modeled data was corrected by this factor, the experimental data could be more easily compared, as shown in Figure 4.7.

Qualitatively, the experimental data seemed to follow similar trends to what was predicted by the lamination theory model because as the predicted displacement per voltage increased, the experimental results did as well. However, only five tests were accomplished; therefore any evidence was far from conclusive.

4.2.3 Blocked Force Results.

Similar to the preliminary free displacement testing, the blocked force was also measured and compared to the expected result from the analytical lamination theory model.

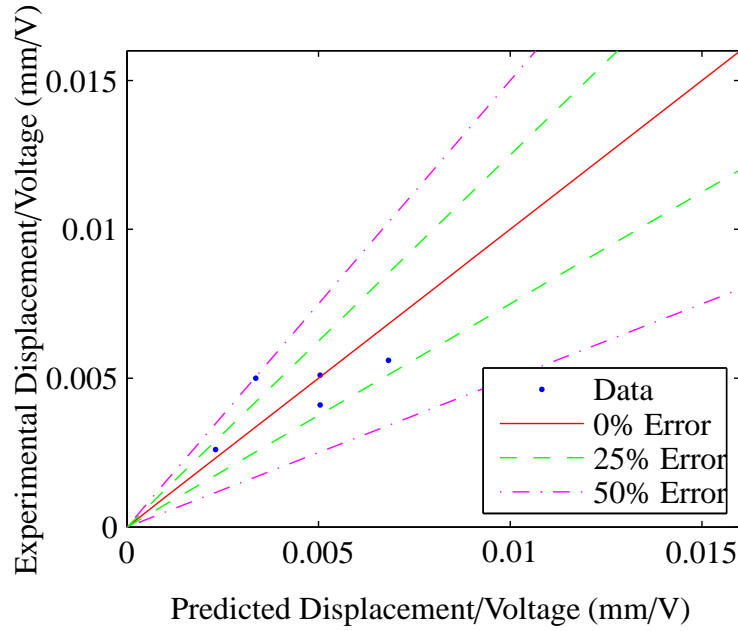


Figure 4.7: Displacement/voltage, experimental vs. modeled (corrected).

However, unlike the displacement results, only one poling direction was tested at a time due to the nature of the test set up. Figure 4.8 shows the blocked force variation with voltage from actuator 6 for both the experimental results and the results predicted from the lamination theory model. Due to the small magnitude of force developed and the resolution of the ATI Nano-17 force transducer, the experimental data appeared noisy, however there was still a clear linear trend of increasing blocked force with increasing voltage.

Since both the experimental and analytical data exhibited linear trends, the slopes of curve fits for the experimental data and analytical data could be compared. Figure 4.9 shows that there was a very large disparity (about 90% difference) between the experimental and analytical data.

The k correction factor used for the free displacement was also used to allow for a comparison of how different the lamination theory model and experimental data were. For the blocked force, the k correction was 9.20, which was much larger than for the free

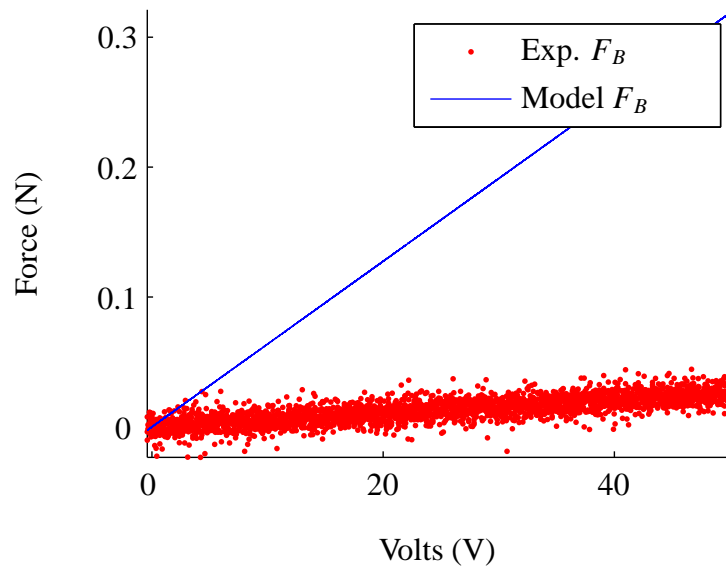


Figure 4.8: Sample blocked force plot, experimental and modeled.

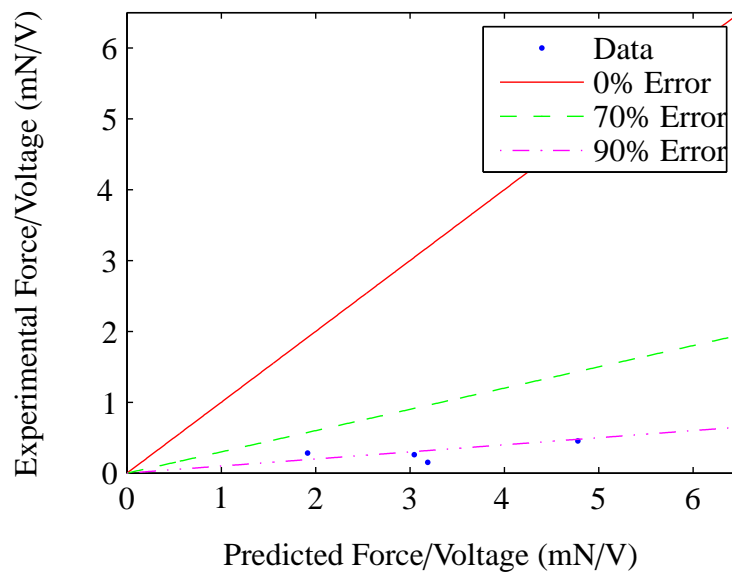


Figure 4.9: Force/voltage, experimental vs. modeled.

displacement. After this correction was applied to the modeled results, which can be seen in Figure 4.10, the blocked force trends could be qualitatively compared.

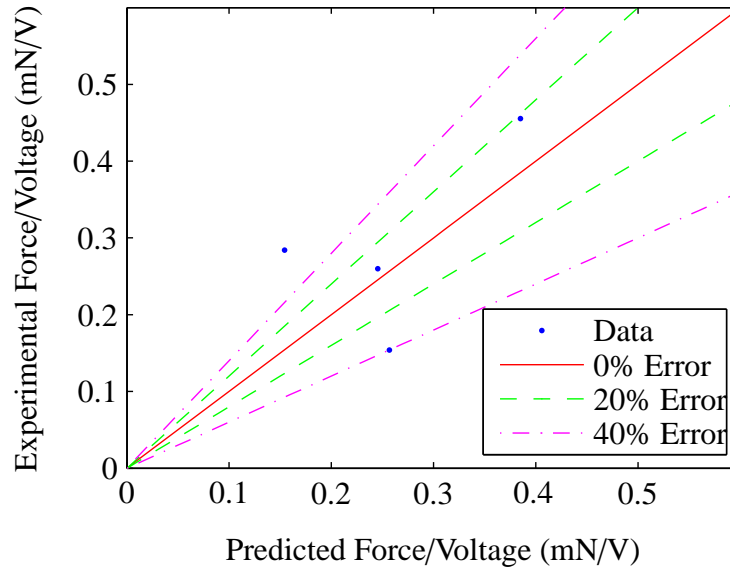


Figure 4.10: Force/voltage, experimental vs. modeled (corrected).

Qualitatively, the experimental and modeled data seemed to follow a similar trend; however the trend is less apparent for the blocked force than the trend was for the free displacement data. While most of the data fell within 25% for the free displacement, the blocked force testing seemed to have much higher variation.

4.2.4 Preliminary Actuator Comparison.

For the actuators produced in the preliminary testing, the results are summarized in Table 4.2. This data shows that the masses of the actuators were higher than predicted, but typically varied by a small amount which is evident by the small standard deviations. The free displacement was less than predicted, but also had a relatively low standard deviation. However, the average blocked force was off by over a factor of ten, and there was quite a large standard deviation. This means that either the lamination theory model was

very inaccurate, the actuators were not manufactured well, the blocked force could not be measured accurately, or some combination of those reasons was causing a large difference between the predicted and actual values.

Table 4.2: k values, preliminary testing.

| Output | k | s |
|-------------------|-------|-------|
| Mass | 0.833 | 0.130 |
| Free Displacement | 2.72 | 0.682 |
| Blocked Force | 9.20 | 4.53 |

4.3 Primary Effects Testing

During the preliminary testing, many different actuators developed defects that made them unusable for testing. One possible cause of the early failure rate was determined to be the use of the Pyralux and silver-conductive epoxy. In order to test this theory, more actuators were created that used the existing epoxy in the uncured carbon fiber to bond the actuator layers together. The actuators were created using the same designs used in the preliminary testing. Overall, these new actuators had a much lower failure rate, which is detailed in Section 4.9. Of the 24 actuators that were planned to be manufactured, 19 were usable, compared with 5 of 24 for the preliminary testing.

The free displacement was tested using the same technique as in the preliminary testing. The blocked force was tested using the same setup, but the excitation voltage was held constant at different levels so that a time average of the force could be taken to alleviate the effect of noise in the system. This technique is detailed in Section 3.4. Figure 4.11 shows what a sample of the average data looked like, as well as the linear

curve fit. Compared with the previous technique, using the averaged force provided much more repeatable results.

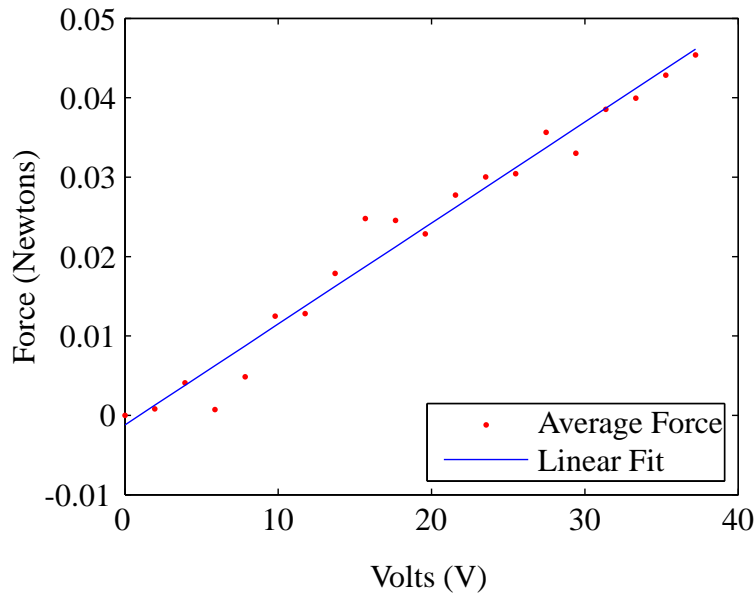


Figure 4.11: Sample blocked force plot, improved testing method, $R^2 = 0.9712$.

Table 4.3 shows the results of this testing. When compared with the results from the preliminary testing, the experimental results appear to have agreed more closely with what the lamination theory model predicts, especially with regard to the free displacement. However, the blocked force was still off by about a factor of over 4, with a large standard deviation.

The results from this testing could also be put into a design of experiments analysis to determine the primary effects of changing the design variables. Figure 4.12 shows how the design variables affected mass, force, and displacement. The solid lines in the figure are the predicted effects while the dashed lines are the confidence intervals on the effects [13]. While most of the results match very closely with the predicted effects in Figure 4.1, some are different. For example the experimental results showed that a larger extension ratio

Table 4.3: k values, primary effects testing.

| Output | k | s |
|-------------------|-------|-------|
| Mass | 0.734 | 0.107 |
| Free Displacement | 2.11 | 0.671 |
| Blocked Force | 4.36 | 1.29 |

decreases the displacement and a thicker piezoelectric layer increases the displacement, while the original analytical lamination theory model predicted the opposite effects.

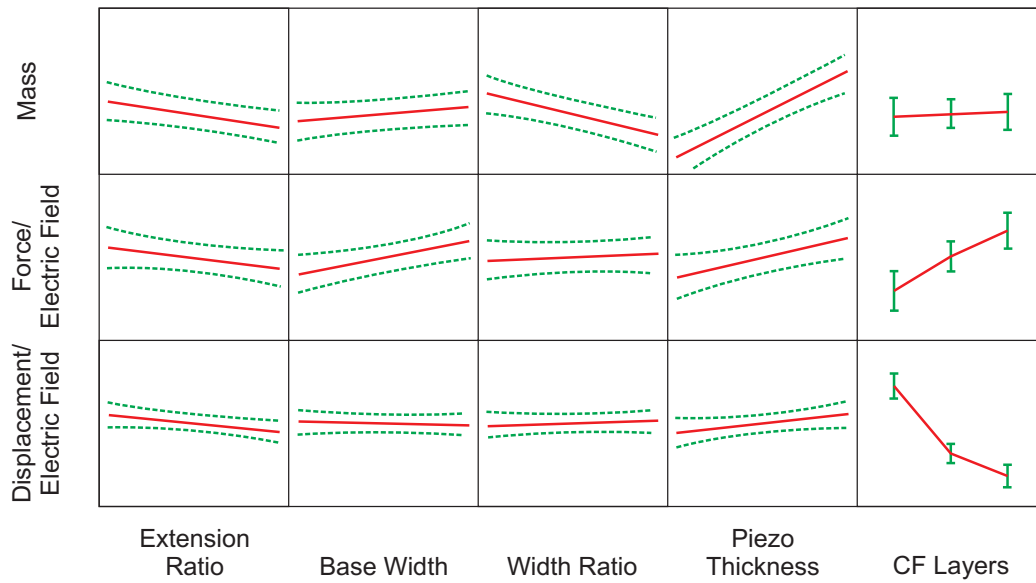


Figure 4.12: Experimental effects of design variables on output parameters.

4.4 Width Effects Testing

The free displacement results from the primary effects testing seemed to be in the right ballpark of what the lamination theory model predicted, however the blocked force varied dramatically. As the analytical design of experiments in Figure 4.1 shows, the base

width and width ratio of an actuator should have been the only variables that affected the blocked force and not the free displacement. Therefore, the effect of different widths was investigated to determine if this was the source of inconsistency between the lamination theory model and reality. The results for this testing are summarized in Table 4.4, which shows that the mass and blocked force results were more accurate than before, but the predicted free displacement has a larger difference from the lamination theory model.

Table 4.4: k values, width effects testing.

| Output | k | s |
|-------------------|-------|--------|
| Mass | 0.746 | 0.0545 |
| Free Displacement | 2.65 | 0.212 |
| Blocked Force | 3.92 | 1.32 |

4.5 Rectangular Actuator Testing

The last group of testing that was accomplished involved creating purely rectangular actuators that did not have any tapering or rigid extensions. The purpose of this testing was to determine if rectangular actuators matched what the lamination theory model predicted. Only four different types of actuators were made, however the width and length of each actuator were varied. Table 4.5 summarizes the results of this testing. These results show that the mass, free displacement, and blocked force were much closer to the predictions of the analytical lamination theory model, with the mass predictions being spot on. Since these results are closer, the large differences that have been observed may arise from the tip extensions or tapered widths.

Table 4.5: k values, rectangular actuator testing.

| Output | k | s |
|-------------------|------|-------|
| Mass | 1.02 | .0317 |
| Free Displacement | 1.56 | 0.257 |
| Blocked Force | 3.63 | 0.360 |

4.6 Commercial Actuator Testing

In previous FWMAV testing at AFIT, commercially available 60/20/0.6 strip actuators purchased from Omega Piezo were used. These actuators weigh 4.45 grams and have a stainless steel middle layer. These commercial actuators are 60 mm x 20 mm and 0.6 mm thick. In order to determine the validity of the experimental set up and the published data, these actuators were also tested for blocked force and free displacement. The predicted actuator outputs were also computed using models that used lamination theory and Euler-Bernoulli beam theory. The piezoelectric constants were estimated to be the same as PZT-5H, and the modulus of elasticity for steel was estimated to be 196 GPa, which is the average for all stainless steels [19].

The published actuator specifications, the experimental results, and predicted outputs are summarized in Table 4.6. These values were all calculated or tested at 150 V, which was the published maximum voltage the strip actuator could handle.

The published values and measured values are very close, which shows that the experimental setup for measuring force and displacement was valid. However, the analytical results for the free displacement were low and the predicted blocked force results were too high; these under and over predictions balanced each other out, and the mechanical energy the actuator produced was close to the modeled predictions.

Table 4.6: Commercial actuator comparison at 150 V for a 60/20/0.6 strip actuator.

| | δ_p (mm) | F_B (N) | U (mJ) | D_U (J/kg) |
|-----------------------|-----------------|-------------|-------------|---------------|
| Published [26] | ≥ 2.6 | ≥ 0.30 | ≥ 0.39 | ≥ 0.0876 |
| Measured | 2.47 | 0.39 | 0.4817 | 0.1082 |
| Lamination Model | 1.33 | 0.856 | 0.5696 | 0.128 |
| Euler-Bernoulli Model | 1.47 | 0.704 | 0.5168 | 0.111 |

4.7 Final Model Results

Combining the results from the primary effects testing (Section 4.3), the width effects testing (Section 4.4), and the rectangular actuator testing (Section 4.5), a more complete picture of what the lamination theory model predicted compared to what happened in reality was created. Using this data, the initial analytical lamination theory model that has been used was modified to closely match the experimental results.

4.7.1 Mass Results.

Initially, the experimental mass results for all of the actuators was larger than what was predicted by the model. Figure 4.13 shows how the results for the mass varied with respect to the predicted mass. Typically, most of the data fell between 0% and 50% error. However, there were a few outliers whose mass was much greater than expected.

These differences were most noticeable in actuators that had a large amount of carbon fiber area, which was interesting because relative to the mass of the entire actuator, the carbon fiber was the lightest portion and the piezoelectric material was the heaviest. Several adjustments were made so that the lamination theory model and experimental data match better. These adjustments involved including the mass of the rigid extension, which was previously ignored, and multiplying the mass of the carbon fiber by an empirical value

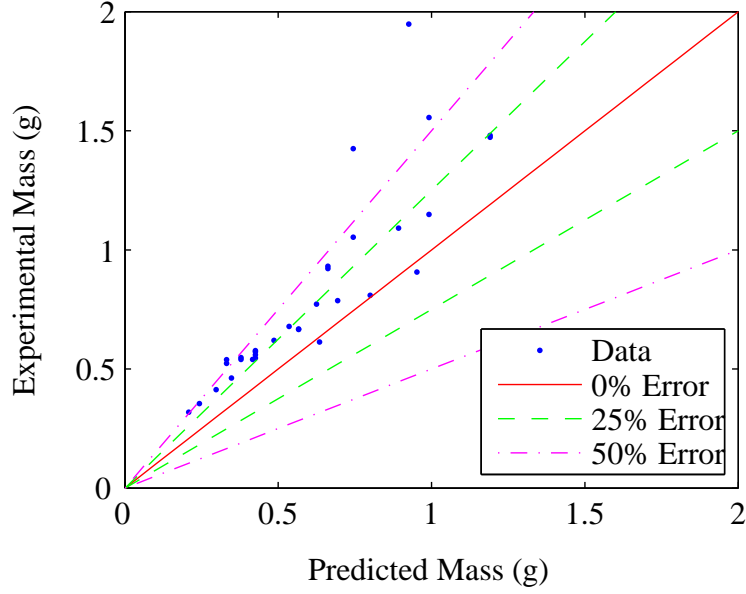


Figure 4.13: Actuator masses, model vs. experimental data.

so the model matched the data. This empirical value accounted for variation due to the epoxy in the carbon fiber, and was referred to as ζ . The empirical value that worked best to minimize the spread and difference from the experimental data was 94.0, and the equation for the adjusted mass can be seen in Equation 4.3. While this correction did not reflect the physics of the actuator, the value helped the lamination theory model agree with what was observed. After making these adjustments, Figure 4.14 shows that the experimental mass and predicted mass agreed much more closely, mostly within a 10% error.

$$m = m_p + m_{cf}(1 + \zeta), \text{ where } \zeta = 94.0 \quad (4.3)$$

Table 4.7 shows the difference in the agreement between the lamination theory model and reality before and after these adjustments were made, which further confirmed that these adjustments improved the ability of the lamination theory model to predict what the mass of each actuator would be.

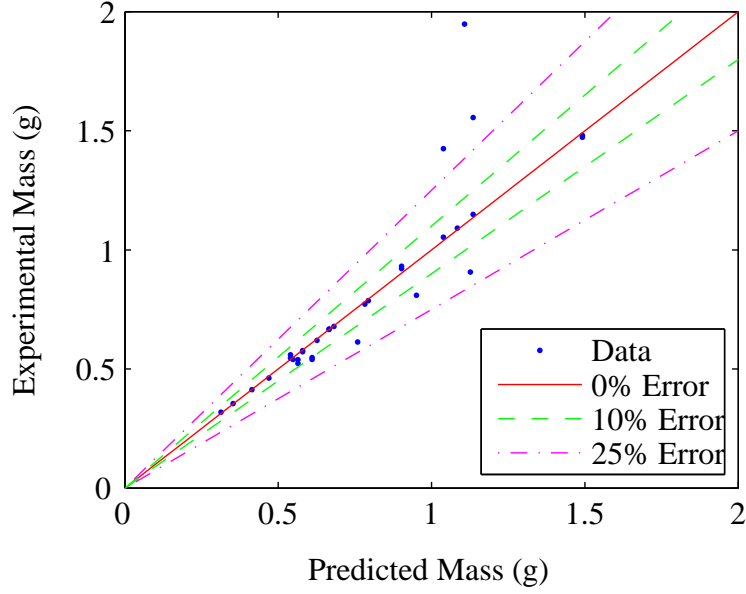


Figure 4.14: Actuator masses, adjusted model vs. experimental data.

Table 4.7: Agreement of actuator mass to original and adjusted models.

| | k | s |
|----------|-------|-------|
| Original | 0.763 | 0.124 |
| Adjusted | 1.00 | 0.128 |

4.7.2 Free Displacement Results.

When the free displacement testing was accomplished, all of the data fell between a 25% and 75% difference compared with the original lamination theory model, which can be seen in Figure 4.15.

When these results were examined more closely, there seemed to be some correlation between the extension ratio (l_r) and the amount that the lamination theory model and experimental data varied for the free displacement. For actuators without an extension, such

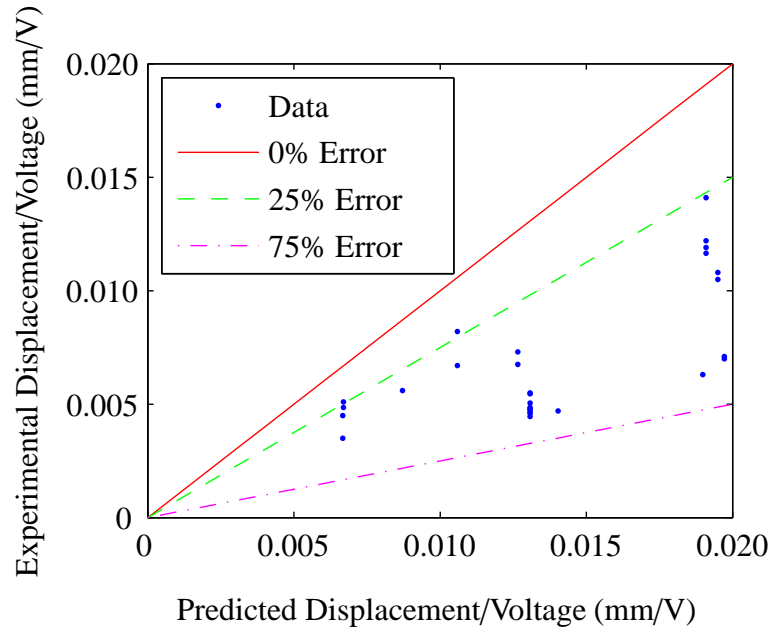


Figure 4.15: Free displacement, model vs. experimental data.

as the rectangular actuators, the displacement results matched closer than the actuators with an extension. For extension ratios of 0.5, the k value for free displacement was close to that of actuators without an extension. However, as the extension ratio increased to 1, the free displacements began to vary from the lamination theory model much more. Table 4.8 shows what the original mean k value for each extension ratio was and the standard deviation of k .

Table 4.8: Extension ratio corrections.

| l_r | k | s |
|-------|------|-------|
| 0.0 | 1.57 | 0.257 |
| 0.5 | 1.61 | 0.199 |
| 1.0 | 2.77 | 0.216 |

In order to correct for the differences in the extension ratio, the original displacement was multiplied by a second-order function of the extension ratio. This adjustment is shown in Equation 4.4. The values used in this correction were obtained from fitting the values for $1/k$ to a quadratic equation. These values did not explain why the free displacement was off, but merely allowed the model to be closer to the experimental data.

$$\delta_P(l_r) = \delta_{P,0}(-0.490l_r^2 + 0.204l_r + 0.645) \quad (4.4)$$

As Figure 4.16 shows, the displacement results agreed much better with what the model predicted after applying this correction. This is also evident in Table 4.9, which shows that the standard deviation was lower than original, and also lower than any one grouping of length ratios.

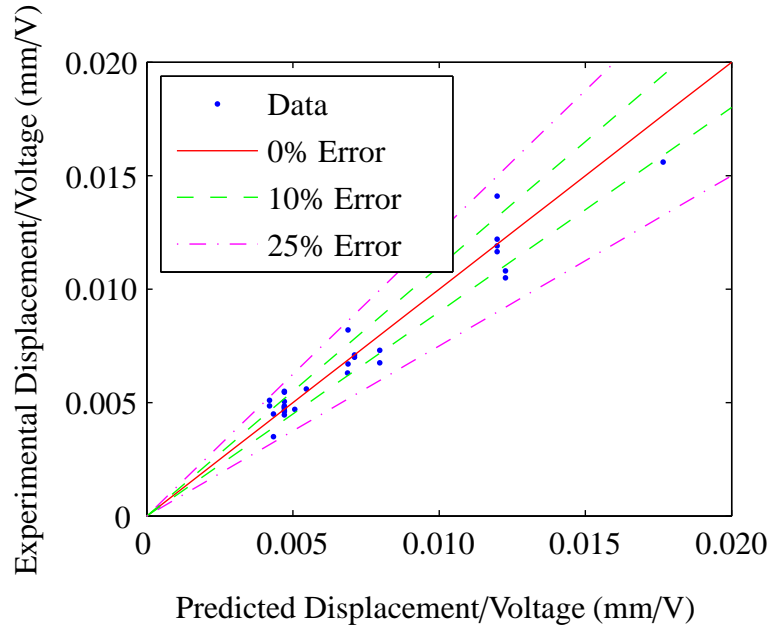


Figure 4.16: Free displacement, adjusted model vs. experimental data.

Table 4.9: Agreement of free displacement to original and adjusted models.

| | k | s |
|----------|------|-------|
| Original | 2.17 | 0.634 |
| Adjusted | 1.00 | 0.106 |

4.7.3 Blocked Force Results.

Unlike the results for free displacement and mass, the results for the blocked force were dramatically different from what the lamination theory model predicted. As Figure 4.17 shows, most of the data fell between 70% and 90% difference.

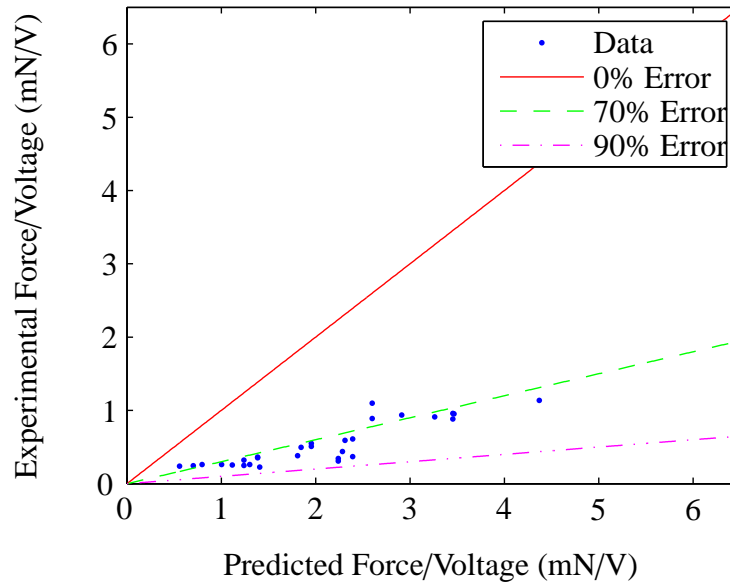


Figure 4.17: Blocked force, model vs. experimental data.

Unfortunately, there were no clear trends with regard to any one of the design variables that signified larger variations from the lamination theory model. In order to find viable correction factors so that the blocked force from the model could be closer to the observed

data, several curve fits were constructed which consisted of design variables (or design variables multiplied by each other) plotted against the values for $1/k$. The curve or curves with the highest coefficients of determination (R^2) were then used to correct the predicted forces to the actual forces.

For the blocked force, the piezoelectric layer thickness, t_p , multiplied by the base width, w_0 , seemed to correct the data quite well, with a small standard deviation. Geometrically, $t_p \times w_0$ is equivalent to the base cross sectional area of one of the piezoelectric layers. Equation 4.5 shows the correction factor that was developed, where t_p and w_0 are in millimeters. Similar to the mass and free displacement corrections, the adjustments for blocked force did not help to explain why the experimental and predicted results were different, but merely allowed the model to predict reality.

$$F_B(t_p, w_0) = F_{B,0} (0.0307(w_0 t_{pzt})^2 - 0.206(w_0 t_{pzt}) + 0.523) \quad (4.5)$$

After this correction was applied, which is shown in Figure 4.18, most (but not all) of the experimental results lie within 25% of the predicted values. This improvement is evident in Table 4.10 which shows how much closer the new modeled results compared to the predicted results.

Table 4.10: Agreement of blocked force to original and adjusted models.

| | k | s |
|----------|------|-------|
| Original | 4.15 | 1.22 |
| Adjusted | 1.00 | 0.223 |

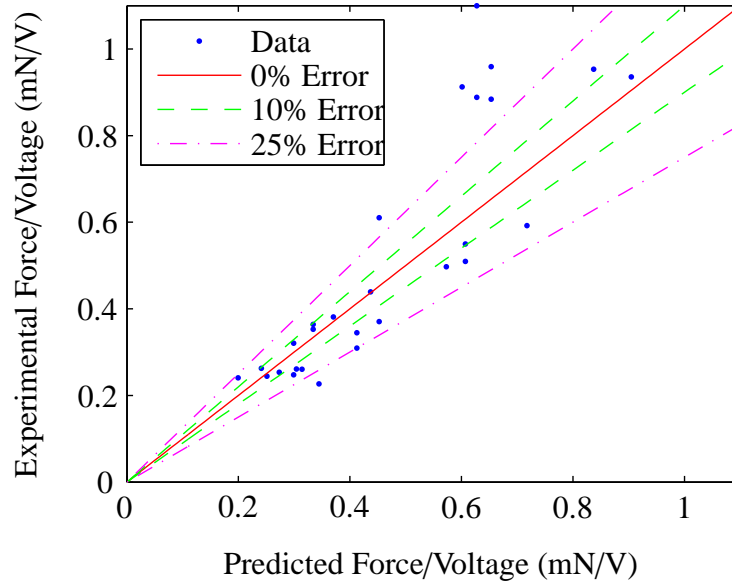


Figure 4.18: Blocked force, adjusted model vs. experimental data.

4.7.4 Final Analytical Effects Analysis.

Using the adjusted model, another full factorial design of experiments was created, which could be compared with the experimental results. The summary of the results are shown in Table 4.11, which assumes a constant electric field strength. As the table shows, the adjusted analytical model and experimental model do tend to agree on how each design variable affects the output.

However, there were three slight differences with regard to the effects of the piezoelectric layer thickness on free displacement, the base width on blocked force, and width ratio on blocked force. While these differences were apparent, none of the differences had strong effects which were opposite. Therefore, the model and experimental data do seem to agree in this respect as well.

Table 4.11: Effects of changing design variables.

| | Mass | Free Displacement | Blocked Force |
|-----------|------|-------------------|---------------|
| t_p | ↑↑ | ↑↓ | ↑↑ |
| CF Layers | ↑↑ | ↓↓ | ↑↑ |
| l_{tot} | ↑↑ | ↑↑ | ↓↓ |
| l_r | ↓↓ | ↓↓ | ↓↓ |
| w_0 | ↑↑ | = = | ↑↑ |
| w_r | ↓↓ | = = | = ↓ |

Red: Experimental, Blue: Analytical

Double Arrow: strong correlation, Single Arrow: weak correlation

4.8 Operating Range Testing

After the actuators were tested for blocked force and free displacement with electric drive fields that were well within ranges that were expected to not cause any failure or hysteresis, the actuators were retested to determine the maximum stresses and strains that they could withstand. During this testing, parallel and simultaneous drive methods were used for various actuators to determine if any differences were apparent. Using this data, Weibull plots of the maximum stresses, strains, and voltages were used to determine safe operating ranges for the custom manufactured actuators. The hysteresis effects from repeatedly applying high electric fields was also examined and compared for both driving methods.

4.8.1 Maximum Stress Testing.

The maximum stress that each actuator encountered was determined by first conducting tests of the maximum blocked force for several actuators. Then, using

Equation 3.3, the maximum stress was calculated. After fitting the data to a Weibull distribution, the results were plotted in Figure 4.19.

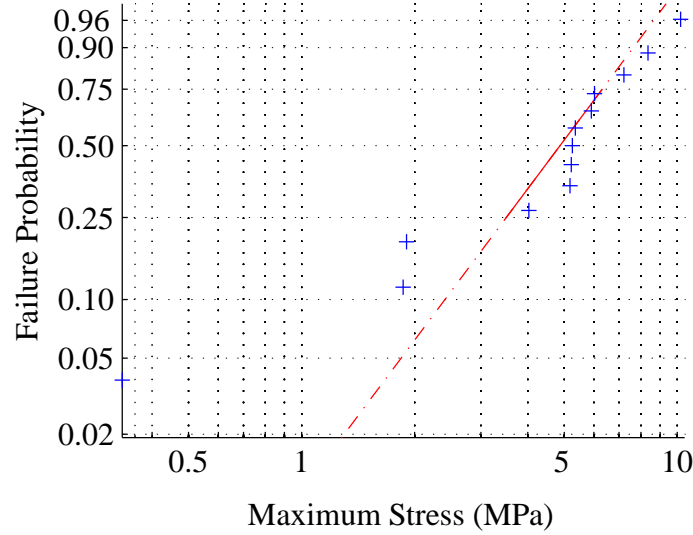


Figure 4.19: Weibull plot of the maximum stresses in actuators.

As the results show, the highest maximum stress is only slightly above 10 MPa. However, the actual strength was expected to be over 110 MPa [32]. One possible explanation is that the maximum stress was not the cause of the actuator failure. This theory is also supported by qualitative observations of the failure events, which typically showed some form of actuator burn out or short out, as opposed to brittle fracture, at higher electric fields.

4.8.2 *Maximum Strain Testing.*

Through continually increasing the amplitude of the electric field in free displacement testing, the maximum displacement that each actuator could achieve was determined. Once the point of maximum displacement was reached, the displacement of the actuator would return to a value of around zero even with increasing electric fields. By using the maximum

displacement and Equation 3.9, the maximum strains achieved could be calculated and fit to a Weibull distribution, as seen in Figure 4.20.

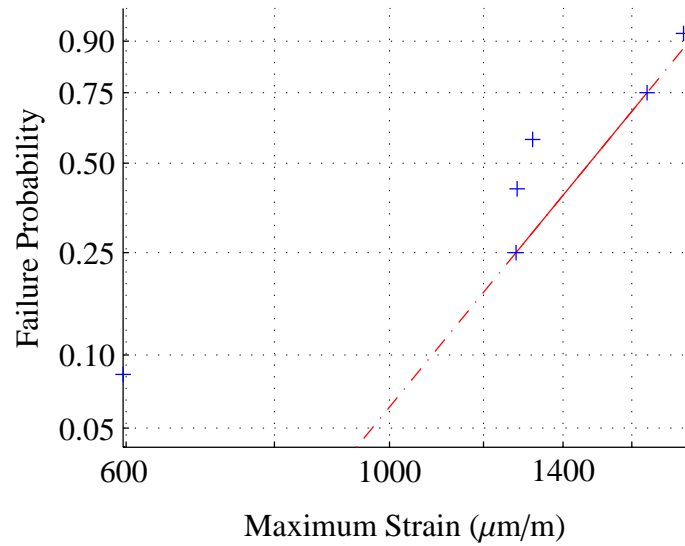


Figure 4.20: Weibull plot of the maximum strains in actuators.

As this figure shows, the maximum strain ever achieved was $1770 \mu\text{m/m}$, and the predicted maximum strain was $1800 \mu\text{m/m}$. While these values are close, most of the maximum strains achieved in the actuators were below $1400 \mu\text{m/m}$. The point just past the maximum displacement was also typically accompanied by some visible and audible sparking, which is evidence of shorting out; however, there were never any visible cracks in the experiments that were carried out. The lack of cracking and strains below the expected maximum seem to imply that the maximum strain was not the method of failure.

4.8.3 *Maximum Voltage Testing.*

The maximum electric field that caused failure in the maximum stress and strain testing was also investigated to determine if the electric field strength could be a more reliable way to predict the actuator failure, and hence determine safe operating ranges. All of the failures that occurred either happened due to an electrical burn out or short out, which

implies that the fracture stresses and strains were not reached. These electrical failures are discussed more thoroughly in Sections 4.9.3 and 4.9.4. Sometimes the shorting out could be visible within the piezoelectric layer, an example of which is shown in Figure 4.21.

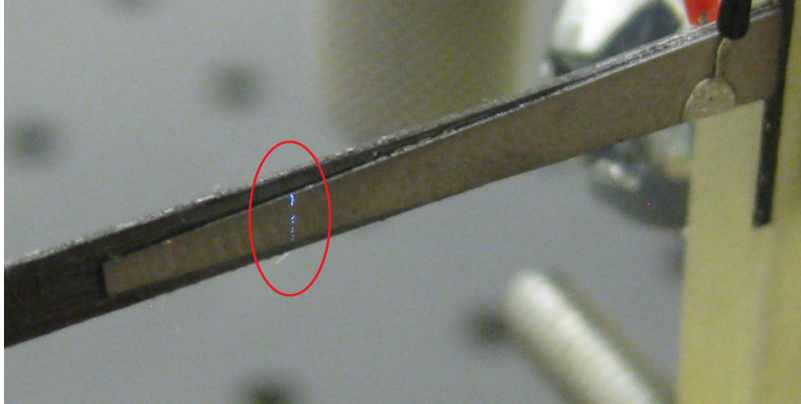


Figure 4.21: Shorting out across piezoelectric layer.

The tests for maximum stress and strain were accomplished using both parallel and simultaneous driving methods, which meant that the two methods could be compared to determine if the simultaneous driving method was truly more beneficial by allowing stronger electric fields to be applied to actuators.

The Weibull plot of the maximum electric fields for the parallel driving method is shown in Figure 4.22. All of the maximum electric fields were at or above the published coercive field of 800 V/mm [30].

For the simultaneous driving method, the Weibull plot of maximum electric fields is shown in Figure 4.23. Looking at the plot, there was a grouping of maximum electric fields at 1125 V/mm. These do not necessarily represent the maximum electric field, but only the maximum electric field that could be achieved in the system because the NI input/output box can only provide ± 10 V, so the maximum voltage that could be achieved

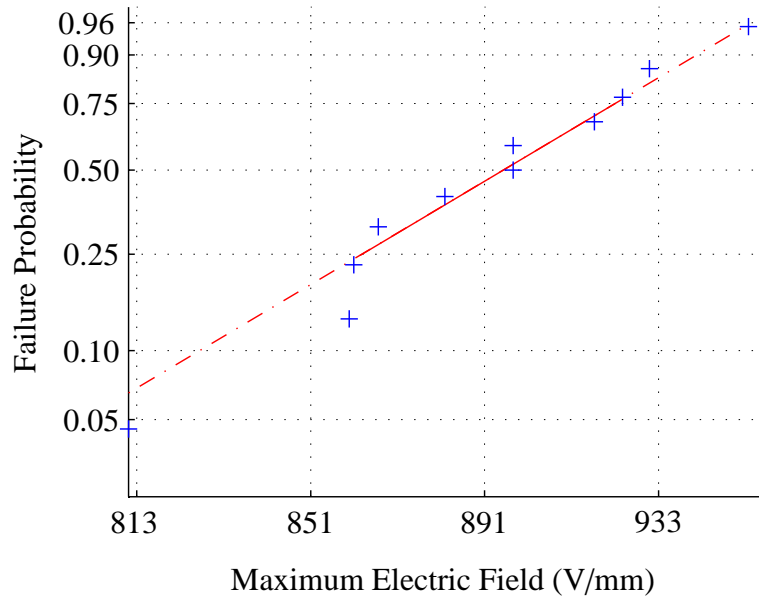


Figure 4.22: Weibull plot of the maximum voltage field for parallel drive.

was ± 300 V. For thinner piezoelectric materials, this was not an issue, but for the thickest material ($t_p = 0.267$ mm), the electric field was maxed out at 1125 V/mm.

As the results from analyzing the maximum electric field showed, the simultaneous driving method seemed to have the ability to provide higher driving fields than the parallel method; however, the simultaneous method also experienced failure at lower electric fields than the parallel method. Since the simultaneous driving method typically required twice the electric field to achieve the same effects as the parallel method and did not allow more than twice the electric field strength, the parallel method seems to be more advantageous from the perspective of the maximum fields that could be achieved.

4.8.4 Recommended Operating Ranges.

Through the previous testing for the maximum stresses, strains, and electric fields that an actuator could withstand, the Weibull parameters λ and k were determined for each failure mechanism. Equation 2.40 was rearranged to solve for the predicted failure level for

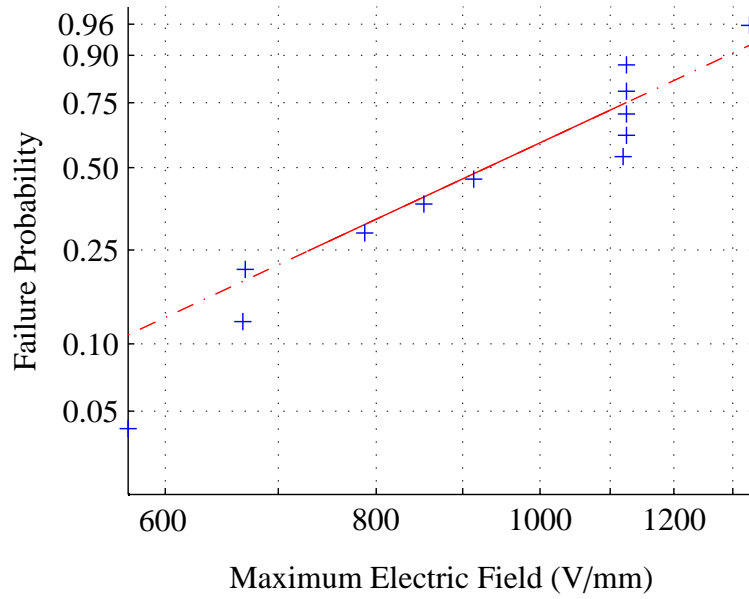


Figure 4.23: Weibull plot of the maximum voltage field for simultaneous drive.

different survival rates, which is shown in Equation 3.2 and reprinted here for convenience.

$$x = \lambda (-\ln(S))^{1/k}$$

For the stress, strain, and electric fields (both simultaneous and parallel), the Weibull parameters are summarized in Table 4.12, as well as the predicted failure levels for 90%, 75%, and 50% survival rates.

As previously mentioned, the stress and strain were unlikely to be the actual causes of failure in each actuator due to the lack of visible cracking in the piezoelectric layers. Also, the simultaneous driving method, while potentially allowing a higher electric field in each layer, needs to have twice the field for the same amount of parallel driving. Therefore, anything below the maximum electric field should be considered within the safe operating range and parallel driving methods should be used. Also, the electric field should be driven as close to the maximum as possible because the hysteresis analysis showed that as higher fields were applied, the actuators became more effective.

Table 4.12: Weibull distribution summary.

| | Weibull parameters | | Survival Rate | | |
|---|--------------------|-------|---------------|------|------|
| | λ | k | 90% | 75% | 50% |
| $E_{S,max}$ (V/mm) | 1040 | 4.85 | 654 | 805 | 965 |
| $E_{P,max}$ (V/mm) | 923 | 21.8 | 833 | 872 | 908 |
| ϵ_{max} ($\mu\text{m}/\text{m}$) | 1400 | 4.356 | 860 | 1100 | 1300 |
| σ_{max} (MPa) | 5.72 | 1.925 | 1.78 | 2.99 | 4.72 |

4.8.5 Hysteresis Analysis.

During the maximum strain testing, the actuators were excited with an oscillating electric field that was slowly increased in amplitude. In addition to determining the maximum strain that each actuator could withstand, the data also helped to describe how the actuators were affected by hysteresis. Figure 4.24 shows the path of the actuator as the voltage was increased. By looking at the differences in the hysteresis of parallel and simultaneous driving methods, any advantage to one driving method over the other could be determined.

There are two important forms of hysteresis that affected the actuators. The first form is that when the voltage was returned to zero, the actuators did not “reset” to their initial position, but instead went to some location that was determined by the maximum electric fields already experienced by the actuator. The second form of hysteresis is that as higher voltages were applied, the average slope of the displacement versus voltage curve changed so that the actuators became more effective. Figure 4.25 shows this change in effectiveness as a ratio to the original displacement versus voltage; the figure also shows how the displacement at zero volts changed. Repeated tests of multiple actuators has shown that

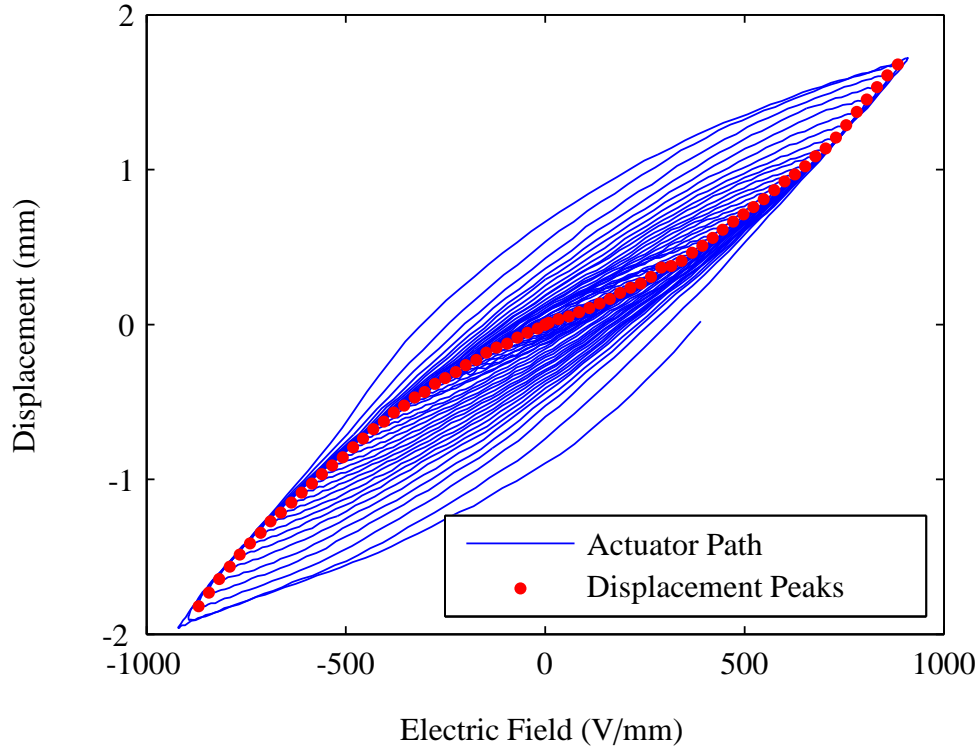


Figure 4.24: Hysteresis effects on the path of an actuator.

the changes in effectiveness did not carry over once the testing was completed; basically the actuators cannot be “pre-charged” to perform better.

Of these two forms of hysteresis, the change in effectiveness was the most important with regards to modeling and determining if there were any advantages to using simultaneous driving methods over parallel methods. As Figure 4.25 shows, the actuator exhibited a largely linear change in effectiveness as a function of the applied electric field; this trend also held true for other actuator designs. Since the trend is linear, the slope of the change in effectiveness versus the applied electric field ($\frac{m_\delta/m_{\delta,0}}{E_{max}}$) could be determined for each test. This slope was denoted by Δm_δ . Table 4.13 shows a summary of the hysteresis effects for both parallel and simultaneous drive methods.

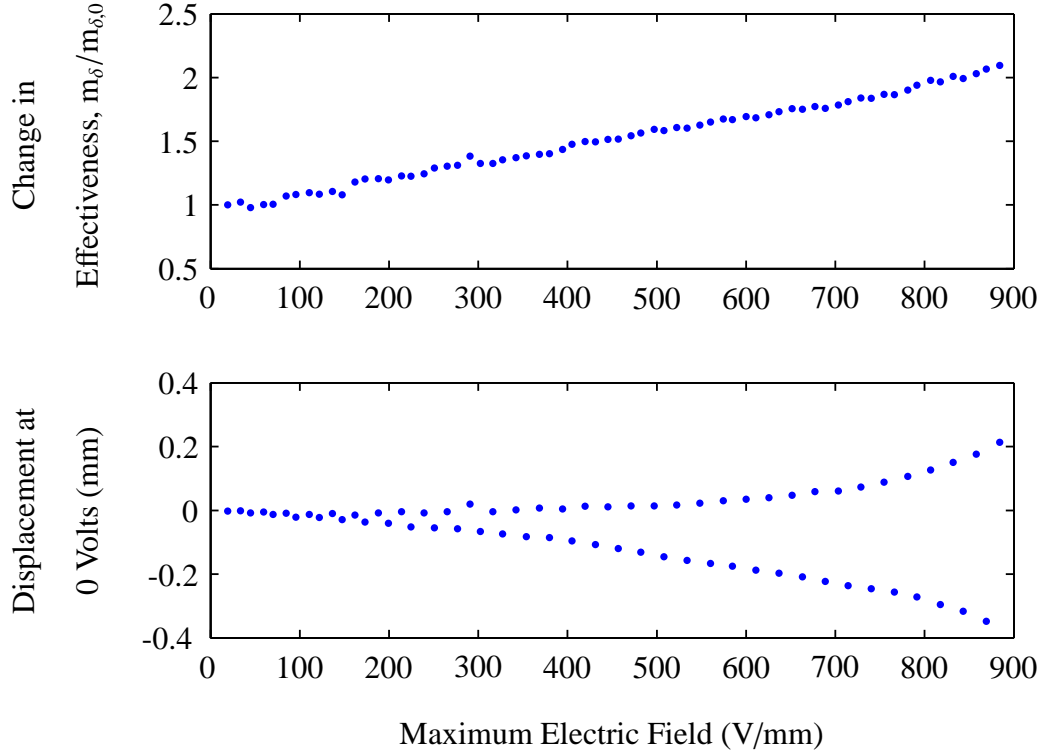


Figure 4.25: Hysteresis effects after high electric fields.

Table 4.13: Measured hysteresis in effectiveness, $\frac{m_\delta/m_{\delta 0}}{E_{max}}$ (mm/kV).

| Drive Method | $\Delta \bar{m}_\delta$ | s | N |
|--------------|-------------------------|-------|-----|
| Parallel | 1.04 | 0.277 | 8 |
| Simultaneous | 1.16 | 0.276 | 4 |
| All | 1.08 | 0.271 | 12 |

Table 4.13 shows that both the parallel and simultaneous driving methods had values for Δm_δ that were close. A two-tailed t -test was used to determine if the mean for the parallel and simultaneous driving methods were statistically different. This statistical test yielded a p value of 0.493, which meant that the two driving methods were not

statistically different (but due to the nature of the t -test, the methods cannot be said to be definitively equal, either). Therefore, an appropriate correction for the hysteresis effects was determined to be $\Delta m_\delta = 1.08$, which is shown in Equation 4.6, where E_{max} has units of kV/mm.

$$m_\delta = (1.08E_{max} + 1) m_{\delta,0} \quad (4.6)$$

4.9 Manufacturing Analysis

Four types of manufacturing defects were found using manufacturing method one, and these defects are piezoelectric short out, actuator burn out, bonding failure, and ceramic cracking. These defects ranged in severity and appeared to have various causes, some of which were unknown.

4.9.1 *Piezoelectric Layer Cracking.*

The first manufacturing problem that was apparent involved cracking of the piezoelectric ceramic during manufacturing. This failure mode was caused by too much pressure being applied during the Pyralux bonding process and a lack of care when the actuators were removed from the clamps. Sometimes the specimens only exhibited small cracks along the edges, while other times the entire piezoelectric ceramic was cracked. The cracking essentially cut out the electrical connection to parts of the ceramic, which rendered those sections useless. A fractured piezoelectric layer can be seen in Figure 4.26. Unfortunately, there is not a solution to fix the piezoelectric material once it has cracked.

4.9.2 *Bonding Failure Between Layers.*

While cracking of the piezoelectric material was caused by too much pressure, too little pressure caused the Pyralux to fail to successfully bond the carbon fiber to the piezoelectric ceramic. This is apparent in Figure 4.27, which shows the separation between the passive and active layers. The severity of this failure mode depended upon how much of the Pyralux failed to bond. Figure 4.27 shows that the tip of the piezoelectric layer failed

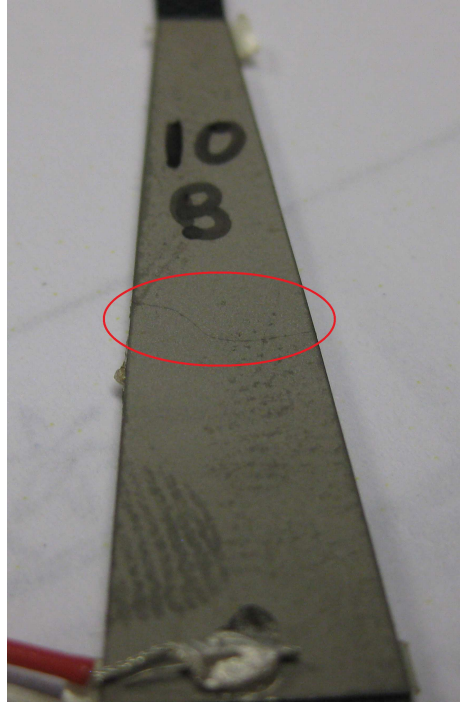


Figure 4.26: Fractured piezoelectric layer.

to bond and began to peel off. This bonding failure has also occurred for entire actuators. If there was only a small portion of the actuator that did not bond, then the actuator would still function, but not as effectively.

4.9.3 Actuator Short Out.

Another manufacturing failure mode was a short circuit of the piezoelectric layers due to an overflow of epoxy. This was most apparent when the silver conductive was used, but there were also some instances of shorting out with the epoxy when using uncured carbon fiber. When the actuator was clamped together, some of the epoxy squeezed out of the edges, which can be seen in Figure 4.28. This defect created an electrical connection (short) between the outer and inner layers of the actuators that prevented the high voltages that are required to drive the actuator from being applied. The solution to this problem

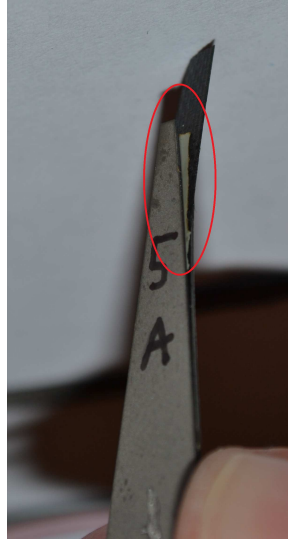


Figure 4.27: Pyralux bonding failure.

was to take a sharp knife and carefully scrape away the excess epoxy so that strong electric fields could be applied.



Figure 4.28: Conductive epoxy overflow between layers.

4.9.4 Piezoelectric Burn Out.

The only unexplained defect was a situation in which the actuator appeared to burn out from both high and low electric fields. For low voltage burn out, this defect was not immediately apparent when looking at an untested actuator, but the application of low

voltages caused the actuator to start smoking slowly. The results of this burning can be seen in Figure 4.29. One possible explanation was that due to the small location that the voltage must travel through, the Pyralux or conductive epoxy heated up and began to burn.

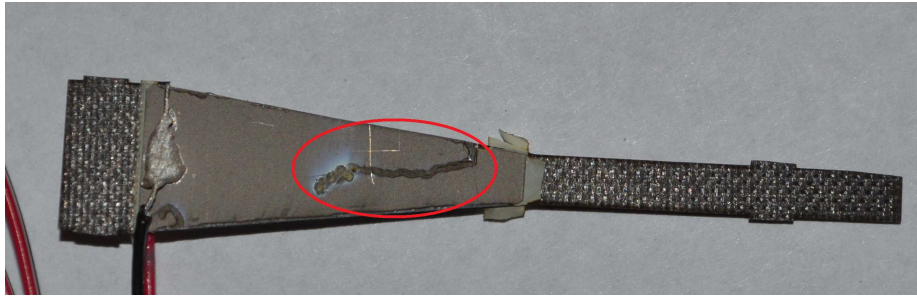


Figure 4.29: Actuator burn out.

For high field burn out, an explanation could be that the piezoelectric ceramics experienced a reorientation of the poles, which has been observed to cause an abrupt and significant increase in current and temperature [16]. If this temperature and current rise was happening, parts of the actuator, such as the Pyralux, may have ignited. During testing for the maximum voltage in Section 4.8.3, some of the actuators experienced high voltage burn out. The current and electric field supplied to the actuator, as well as the resulting displacement, are shown in Figure 4.30. This figure shows a large spike in current at the onset of burn out. The abrupt increase in current supported the theory that the burn out was due to shorting, and the current causing resistive heating and igniting part of the actuator.

4.9.5 Comparison of Manufacturing Methods.

The final outcome for each actuator could be grouped into one of four categories: manufacturing defect (MD), burn out (BO), early failure (EF), and testing completed (TC). Manufacturing defects included cracking and shorting out along the edges that could not be fixed. Burn out encompassed any premature burning out of the actuator below expected

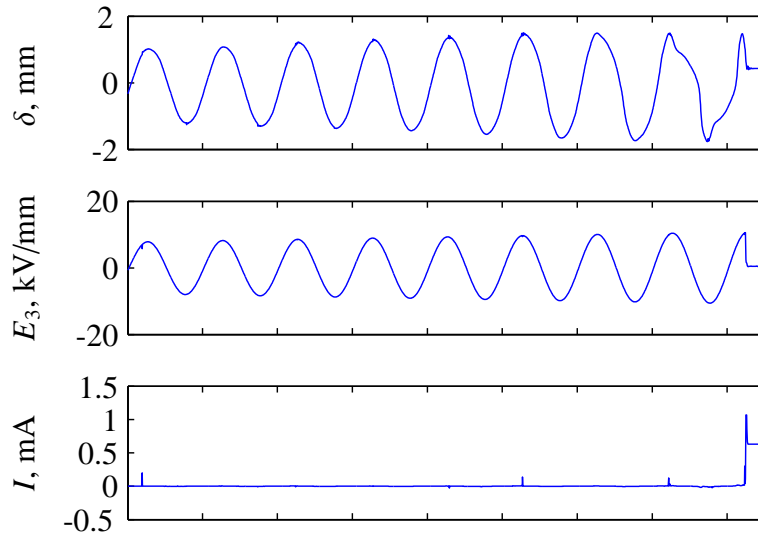


Figure 4.30: Displacement compared to driving voltage and current.

failure levels. An early failure was defined as anything that caused the actuator to stop working after some data was already gathered. Testing completed included all actuators that were able to successfully finish all of the free displacement and blocked force tests.

Figure 4.31 shows the outcome for all of the actuators created using the first manufacturing method. For this method, only about a fifth of all actuators that were produced successfully finished the experimental testing. The majority had some form of manufacturing defect, and a large amount also experienced burn out or early failure.

For the second manufacturing method, the story is quite different. Figure 4.32 shows that for this method, 75% of the actuators were able to complete experimental testing. Most of these improvements came from reductions in the manufacturing defects and early burn out. While the rate of early failures was reduced, the amount was not dramatically significant. Through this comparison, using uncured carbon fiber in the actuator manufacture offers a dramatic improvement over using Pyralux and conductive epoxy to bond the layers together.

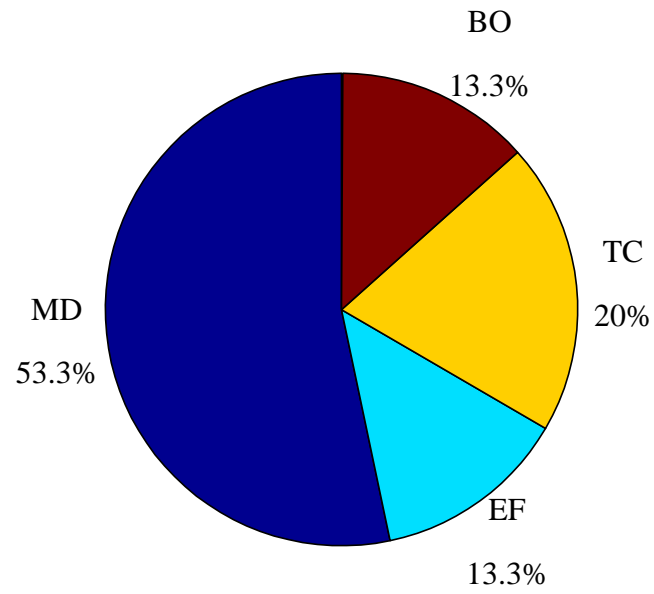


Figure 4.31: Failure percentages from manufacturing method one (15 Samples).

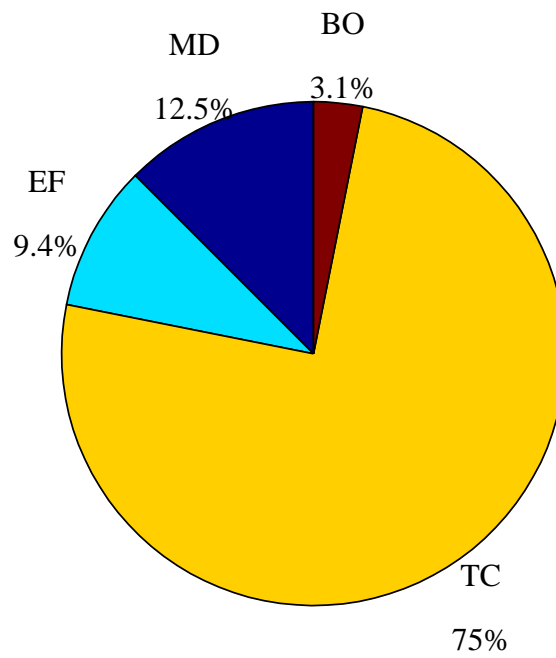


Figure 4.32: Failure percentages from manufacturing method two (32 Samples).

4.10 Final Optimization

The general goal of this project was to develop an optimized actuator for a known requirement of output mechanical energy. In order to show that this is possible, three designs were considered for analytical comparison. For this comparison, the maximum electric driving field was set at 800 V/mm, which should give a survival rate of over 90%.

The first design created was an arbitrary rectangular actuator with dimensions of 50 mm x 10 mm, referred to as design (A). This design was not optimized, but the intent was to create a reference point to compare other designs against. The output mechanical energy was predicted to be 0.0590 mJ using the adjusted model. Each design in this analysis was required to produce at least this mechanical energy at the same electric field.

The two optimized designs were another rectangular actuator and a tapered actuator with an extension, with requirements that the total length was between 40 and 60 mm and the base width was between 5 and 20 mm. The optimized rectangular actuator, design (B), was created by setting the extension ratio to zero and the width ratio to one in the optimization routine. The optimized tapered actuator, design (C), was created by removing the restrictions on the extension ratio and width ratio. These actuators were optimized using the adjusted models. Table 4.14 gives a summary of these actuators and Figure 4.33 shows what the designs look like.

Table 4.14: Theoretical improvement from an arbitrary rectangular actuator.

| Design | t_p | CF Layers | l_{tot} | l_r | w_0 | w_r | m | D_U | Savings |
|--------|---------------|-----------|-----------|-------|-------|-------|------|--------|---------|
| | μm | | mm | | mm | | mg | J/kg | |
| (A) | 191 | 5 | 50 | 0 | 10 | 1 | 1800 | 0.0328 | 0% |
| (B) | 267 | 3 | 42.2 | 0 | 5 | 1 | 972 | 0.0606 | 46.0% |
| (C) | 267 | 3 | 42.2 | 0.833 | 5 | 1.667 | 353 | 0.167 | 80.4% |

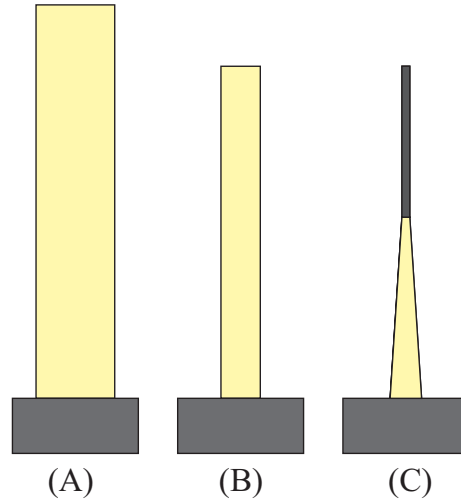


Figure 4.33: Optimized designs.

As the results in Table 4.14 show, the tapered actuator with an extension, design (C), should have been 80.4% lighter than the original actuator. However, the original actuator was just an arbitrary design. In order to truly see a difference, the tapered actuator should be compared to the optimized rectangular actuator. In this case, the tapered actuator was predicted to have a mass savings of 63.7% for the same mechanical energy output.

In order to test if the selected design was better than the optimized rectangular actuator, three rectangular actuators (design B) and six of the tapered actuators (design C) were manufactured and tested. The results of this testing are summarized in Table 4.15.

Table 4.15: Optimized actuator comparison, experimental data.

| Design | m (mg) | U (mJ) | D_U (J/kg) |
|--------|--------|----------|--------------|
| (B) | 960.1 | 0.0654 | 0.0681 |
| (C) | 293.2 | 0.0379 | 0.129 |

Unfortunately, the optimized tapered actuators did not produce the same mechanical energy as the rectangular actuators or what the improved model predicted. This could partly have been due to difficulties in assembling such small actuators because a larger amount of precision was required than for the rectangular actuators. However, the mechanical energy density was still 89.5% larger than the rectangular actuators, which shows that the tapered actuators with an extension still offered significant improvements. Also, while the blocked force produced for any of the actuators was not close to the force produced by the commercial actuators described in Section 4.6, the energy density of the optimized actuators are 19.5% greater than the commercial actuators.

4.11 Chapter Summary

The testing of actuators, both analytically and experimentally, was analyzed in this chapter to develop models that fit the empirical data and were able to design optimized actuators. First, the lamination theory model was selected for further analysis because it can take into account tapering the width of an actuator and adding a rigid extension. The mass, free displacement, and blocked force were determined for each actuator and compared to what the model predicted. There were some differences for each output compared to the model, but especially for the blocked force. These differences were corrected for by utilizing empirically determined values. The maximum operating range was determined to be a function of the applied electric field, and the predicted survivability at different field strengths was calculated using a Weibull distribution. Using this data, optimized actuators were designed and manufactured that exhibited an improvement in energy density over both manufactured rectangular actuators and commercially available strip actuators. The next chapter focuses on the conclusions that can be drawn from this data and the future work that could be accomplished.

V. Conclusions and Recommendations

5.1 Research Goals

The purpose of this project was to develop optimized piezoelectric actuators for use in flapping wing micro air vehicles by minimizing the mass and maximizing the output mechanical energy of the actuators. This was accomplished by first using an analytical lamination theory model to predict how different design variables affected the output performance of the actuators. Then, experimental testing was accomplished to attempt to replicate these results using two different manufacturing methods. Using the experimental results, the original lamination theory model could be adjusted using empirical data, the maximum operating range for actuators could be determined, and the differences in the manufacturing techniques could be examined. Through this process, optimized piezoelectric bimorph actuators for use in a FWMAV with two independently actuated wings could be designed.

5.2 Conclusions

Both manufacturing methods created piezoelectric bimorph bending actuators, but utilized different bonding processes. The first manufacturing method required the use of Pyralux and silver conductive epoxy and exhibited a high failure rate. The second method, which used the existing epoxy in the carbon fiber layup for bonding between layers, was much more successful. The overall effects of changing the design variables were similar for both the lamination theory model and the experimental data. However, the experimental results exhibited differences from the predicted results, so the lamination theory model was empirically adjusted to more accurately reflect reality. Since the second manufacturing method matched the predicted results better and produced actuators more reliably, only data from the second technique was used for the model adjustment.

These adjustments used empirical data to fit the lamination theory model to experimental results, however, these changes did not reflect the physics of the actuator and did not explain why the original modeled data was different than the experimental results. The original lamination theory model predictions were close to the commercial actuator results, therefore there may have been a problem with the manufacturing methods used at AFIT, which lessened the actuator effectiveness.

Also, sources of error in the lamination theory model may have stemmed from violating some of the assumptions of lamination theory. For example, the thickness of each layer was assumed to be much larger than the displacements (see Section 2.4.2). For this research, the displacements were often greater than ± 1 mm, which is much greater than the thickness of the actuators, which was typically less than 0.5 mm. This shows that this assumption was invalidated; however the amount that this contributed to the differences between the model and the results was unknown.

In addition to the model comparison, the maximum operating range of the piezoelectric actuators was determined by conducting experimental tests to failure for stress, strain, and electric field strength using both simultaneous and parallel driving methods. This data was then fit to Weibull distributions that, when combined with qualitative observations of the failure modes, showed that the maximum electric field was the limiting factor for the actuators, and the simultaneous driving method did not provide any significant advantages over the parallel driving method. For a 90% survival rate, 833 V/mm should be used.

The effects of hysteresis were also analyzed for both driving methods. As higher electric fields were applied for the actuators, the average effectiveness at each voltage level increased. While the simultaneous driving method was expected to show less hysteresis, there were not any statistical differences between the two.

Through this combination of analysis and testing, the maximum mechanical energy that would be produced by an actuator could be estimated. Utilizing an analytical exhaustive search optimization routine, tapered actuators with extensions were designed and then manufactured that had an average energy density of 0.129 J/kg, which was an improvement of 89.5% over an optimized rectangular actuator. This was also an improvement of 19.5% over the commercial actuators currently being used.

5.3 Recommendations for Future Work

Currently, none of the actuators which were designed in this research were used to actually flap an engineered wing. Further research should compare the lift from commercial actuators produced by Omega Piezo, Inc. to the lift produced by the optimized actuators. However, since the optimized actuators would require using a different transmission ratio than the commercial actuators, specific linkages for each actuator design would need to be created.

The actuators manufactured for this research did not meet the predicted values from the original lamination theory model. Further research should focus on explaining what caused these differences. Some possible causes for the variation from the lamination theory model could involve inaccurate material properties in the carbon fiber or piezoelectric layers, epoxy effects, or nonuniform electrical fields. In order to determine if these differences were due to the manufacturing techniques or problems with the lamination theory model, actuators with similar specifications but produced by companies that specialize in piezoelectric actuator production should be tested and compared to the lamination theory model. Several companies such as Piezo Systems, Inc. offer to build custom bimorph actuators, so further research into this area could involve testing commercially manufactured actuators of similar designs used in this research to determine if the results agree more closely with the original lamination theory model.

The primary failure mechanism in the actuators was due to the high electric fields, which caused either piezoelectric failure or arcing to occur across the different layers in the bimorph actuators. One possibility to increase the maximum electric field strength would be to insulate the edges of the actuators. The insulation may help to prevent both arcing and burn out, since these mechanisms typically started along the edges of the actuators. Building and testing the actuators with insulated edges may yield better performance results that would offset the weight of the insulation.

In Section 2.5, a process for testing actuators was discussed which used electromagnets to create a mass-spring-damper system to mimic realistic loads experienced during flight. Experimental testing using this technique was beyond the scope of this thesis; however this form of testing would help to further develop optimized actuators by determining during which phases of flight the actuators are under-powered or over-powered.

Finally, in the construction of the piezoelectric actuators one of the most tedious and time consuming processes was the attachment of the wires to provide the electric fields. Designs for the bench testing and the final FWMAV could include a way where the actuators are excited by electrical connections which are not permanently attached to the actuators, but instead are connected through contact, similar to the brushes in a DC motor. This system would save time in the actuator manufacturing process, and it could also potentially save weight in a FWMAV by eliminating some of the wiring.

Appendix: MATLAB Functions

Throughout the research in this thesis, various MATLAB scripts were written that allowed for the modeling and optimization of piezoelectric actuators, using both the original model and the empirically adjusted model. These functions, which are described below, are available on a CD-ROM.

1. `[mass,blockedForce,freeDisplacement] = ActuatorModelOriginal(l,lr, w0,wr,tp,layup,dispResult,V)`

This function predicts the mass, blocked force, and free displacement of an actuator using the original model developed in [42] without any adjustments.

Outputs:

`mass`: predicted mass of the actuator (kg).

`blockedForce`: predicted blocked force of the actuator (N).

`freeDisplacement`: predicted free displacement (one-sided) (m).

Inputs:

`l`: total length of the actuator (m).

`lr`: actuator extension ratio (l_{ext}/l_p).

`w0`: base width of the actuator (m).

`wr`: actuator width ratio (w_0/w_{nom}).

`tp`: piezoelectric ceramic thickness (one side) (m).

`layup`: matrix of the carbon fiber layup orientation in degrees offset from tip (i.e. [0 90 0]).

`dispResult`: whether or not to display the actuator geometry and performance results. 1 = display result. 0 = do not display result.

`V`: voltage applied to the actuator in parallel drive (V).

2. `[mass,blockedForce,freeDisplacement] = ActuatorModelAdjusted(l,lr, w0,wr,tp,layup,dispResult,V)`

This function predicts the mass, blocked force, and free displacement of an actuator using the model developed in [42] and adjusted with empirical constants.

Outputs/Inputs are identical to `ActuatorModelOriginal`.

3. `[Acf,Bcf,Dcf,tcf] = CFMatrixCalc(layup)`

This function calculates the stiffness matrices and thickness for a carbon fiber layup.

Outputs:

`Acf`: extensional stiffness matrix $[A]$ for the layup (N/m).

`Bcf`: coupling stiffness matrix $[B]$ for the layup (N).

`Dcf`: combined stiffness matrix $[D]$ for the layup (N-m).

`tcf`: thickness of the carbon fiber layup (m).

`layup`: matrix of the carbon fiber layup orientation in degrees (i.e. $[0\ 90\ 0]$).

Inputs:

4. `[l,lr, w0,wr,tp,layup] =`

`OptimizedActuator(Umin,n,lRange,w0Range,pOpt,layupOpt,dispResult)`

This function uses a brute force optimization routine to find the lightest actuator to meet the requirements for mechanical energy output.

Outputs:

`l`: total length of the actuator (m).

`lr`: actuator extension ratio (l_{ext}/l_p).

`w0`: base width of the actuator (m).

`wr`: actuator width ratio (w_0/w_{nom}).

`tp`: piezoelectric ceramic thickness (one side) (m).

`layup`: matrix of the carbon fiber layup orientation in degrees offset from tip (i.e. $[0\ 90\ 0]$).

Inputs:

`Umin`: minimum required mechanical energy (J).

`n`: number of different values for a variable to try. Higher numbers will give a better result, but run slower.

`lRange`: a two element array of the smallest and largest desired length to define the search area, $[lmin\ lmax]$ (meters).

`w0Range`: a two element array of the smallest and largest desired base width to define the search area, $[w0min\ w0max]$ (meters).

`pOpt`: an array of elements that define the different options for the thickness of the piezoelectric layer, $[tp1\ tp2\ \dots\ tpi]$ (meters).

`layupOpt`: a cell of arrays that define the different options for the carbon fiber layer, $\{layup1\ layup2\ \dots\ layupi\}$ (degrees).

`dispResult`: whether or not to display the actuator geometry and performance results. 1 = display result. 0 = do not display result.

Bibliography

- [1] Alguer, M, B.L Cheng, F Guiu, M.J Reece, M Poole, and N Alford. “Degradation of the d33 piezoelectric coefficient for PZT ceramics under static and cyclic compressive loading”. *Journal of the European Ceramic Society*, 21(10-11):1437 – 1440, 2001. ISSN 0955-2219.
- [2] Anderson, Michael L. *Design and Control of Flapping Wing Micro Air Vehicles*. Ph.D. thesis, Air Force Institute of Technology, September 2011.
- [3] ATI Industrial Automation. *ATI Force/Torque Sensor: Nano17 Titanium*, 2011.
- [4] Ballato, A. “Piezoelectricity: old effect, new thrusts”. *Ultrasonics, Ferroelectrics and Frequency Control, IEEE Transactions on*, 42(5):916 –926, sept. 1995. ISSN 0885-3010.
- [5] Burden, Richard L. and J. Douglas Faires. *Numerical Analysis*. Thomson Brooks/Cole.
- [6] Cross, Eric. “Materials science: Lead free at last”. *Nature*, 432, Nov. 2004.
- [7] Daniel, Isaac M. and Ori Ishai. *Engineering Mechanics of Composite Materials*. Oxford University Press, second edition, 2006.
- [8] Davis, William R., Bernard B. Kosicki, Don M. Boroson, and Daniel F. Kostishack. “Micro Air Vehicles for Optical Surveillance Micro Air Vehicles for Optical Surveillance”, 1996.
- [9] Dickinson, Michael H., Fritz-Olaf Lehmann, and Sanjay P. Sane. “Wing Rotation and the Aerodynamic Basis of Insect Flight”. *Science*, 284(5422):1954–1960, 1999.
- [10] E. Steltz, S. Avadhanula, M. Seeman and R.S. Fearing. “Power Electronics Design Choice for Piezoelectric Microrobots”. *International Conference on Intelligent Robots and Systems*, October 2006.
- [11] Finio, Benjamin M., Jessica K. Shang, and Robert J. Wood. “Body torque modulation for a microrobotic fly”. *Proceedings of the 2009 IEEE international conference on Robotics and Automation, ICRA’09*, 2546–2553. IEEE Press, Piscataway, NJ, USA, 2009. ISBN 978-1-4244-2788-8.
- [12] Hundley, R. O. and E. C Gritton. *Future Technology-Driven Revolution in Military Operations*. Technical report, RAND Corporation, 1994.
- [13] JMP. *JMP Design of Experiments (DoE)*.

- [14] Karpelson, Michael, Gu-Yeon Wei, and Robert J. Wood. “Milligram-scale high-voltage power electronics for piezoelectric microrobots”. *Proceedings of the 2009 IEEE international conference on Robotics and Automation*, ICRA’09, 883–890. IEEE Press, Piscataway, NJ, USA, 2009. ISBN 978-1-4244-2788-8.
- [15] Katz, H.W. (editor). *Solid State Magnetic and Dielectric Devices*. John Wiley and Sons, inc., London, 1959.
- [16] Li, T, Y H Chen, F Y C Boey, and J Ma. “High amplitude vibration of piezoelectric bending actuators”. *Journal of Electroceramics*, 18(3-4):231–242, 2007.
- [17] Mason, Warren P. “Piezoelectricity, its history and applications”. *Journal of the Acoustical Society of America*, 70(6):1561–1566, December 1981.
- [18] Matthew Keennon, Henry Won, Karl Klingebiel and Alexander Andriukov. “Development of the Nano Hummingbird: A Tailless Flapping Wing Micro Air Vehicle”. *50th AIAA Aerospace Sciences Meeting including the New Horizons Forum and Aerospace Exposition*, January 2012.
- [19] MatWeb. “Overview of materials for Stainless Steel”. URL <http://www.MatWeb.com>.
- [20] Michael L. Anderson, Nathanael J. Sladek and Richard G. Cobb. “Design, Fabrication, and Testing of an Insect-Sized MAV Wing Flapping Mechanism”. *49th AIAA Aerospace Sciences Meeting including the New Horizons Forum and Aerospace Exposition*, (2011-549), January 2011.
- [21] Micro-Epsilon. *Intelligent Laser-Optical Displacement Measurement: optoNCDT 1800*.
- [22] Milton, J. Susan and Jesse C. Arnold. *Introduction to Probability and Statistics*. McGraw-Hill.
- [23] Mueller, Kellog J.C. Ifju P.G. Shkarayev S.V., T.J. *Introduction to the Design of Fixed-Wing Micro Air Vehicles*. AIAA Education Series. AIAA, Reston, Virginia, 2007.
- [24] Ohara, Ryan P. *The Characterization of Material Properties and Structural Dynamics of the Manduca Sexta Forewing for Application to Flapping Wing Micro Air Vehicle Design*. Ph.D. thesis, Air Force Institute of Technology, June 2012.
- [25] Olympio, K Raymond and Guylaine Poulin-Vittrant. “Piezoelectric actuation of a flapping wing accounting for nonlinear damping”. *Active and Passive Smart Structures and Integrated Systems 2011*, 7977:79771S–79771S–12, 2011.
- [26] Omega Piezo Technologies, Inc., 2591 Clyde Ave, State College, PA. *Strip Actuators (Bimorph Equivalent)*, 2008.

- [27] Perez-Arancibia, N.O., J.P. Whitney, and R.J. Wood. “Lift force control of a flapping-wing microrobot”. *American Control Conference (ACC)*, 2011, 4761–4768. 29 July 1 2011. ISSN 0743-1619.
- [28] Pesavento, Umberto and Z. Jane Wang. “Flapping Wing Flight Can Save Aerodynamic Power Compared to Steady Flight”. *Phys. Rev. Lett.*, 103:118102, Sep 2009.
- [29] Pico Electronics, 143 Sparks Ave. Pelham, NY 10803. *Low Profile DC-DC Converters: Series AV/SMV*.
- [30] Piezo Systems, Inc, 65 Tower Office Park, Woburn, MA 01801. *Piezo Catalog*, 2011.
- [31] Sitti, Metin, Domenico Campolo, Joseph Yan, Ronald S. Fearing, Tao Su, David Taylor, and Timothy D. S. “Development of PZT and PZN-PT based unimorph actuators for micromechanical flapping mechanisms”. *In Proc of IEEE Intl Conf on Robotics and Automation, Seoul, Korea*, 21–26. 2001.
- [32] Steven R. Anton, Alper Erturk and Daniel J. Inman. “Bending Strength of Piezoelectric Ceramics and Single Crystals for Multifunctional Load-Bearing Applications”. *IEEE Transactions on Ultrasonics, Ferroelectrics, and Frequency Control*, 59(6):1085–1092, June 2012.
- [33] Uchino, Kenji. *Piezoelectric Actuators and Ultrasonic Motors*. The Kluwer International Series. Kluwer Academic Publishers, Boston/Dordrecht/London, 1997.
- [34] Wang, Qing-Ming and L Eric Cross. “Performance analysis of piezoelectric cantilever bending actuators”. *Ferroelectrics*, 215(1):187–213, 1998.
- [35] Wang, Qing-Ming, Xiao-Hong Du, Baomin Xu, and L.E. Cross. “Electromechanical coupling and output efficiency of piezoelectric bending actuators”. *Ultrasonics, Ferroelectrics and Frequency Control, IEEE Transactions on*, 46(3):638–646, may 1999. ISSN 0885-3010.
- [36] Weinberg, M.S. “Working equations for piezoelectric actuators and sensors”. *Microelectromechanical Systems, Journal of*, 8(4):529–533, dec 1999. ISSN 1057-7157.
- [37] Whitney, J P, P S Sreetharan, K Y Ma, and R J Wood. “Pop-up book MEMS”. *Journal of Micromechanics and Microengineering*, 21(11):115021, 2011.
- [38] Wood, R J. “The First Takeoff of a Biologically Inspired At-Scale Robotic Insect”, 2008.
- [39] Wood, R.J. “Design, fabrication, and analysis of a 3DOF, 3cm flapping-wing MAV”. *Intelligent Robots and Systems, 2007. IROS 2007. IEEE/RSJ International Conference on*, 1576–1581. 29 2007-nov. 2 2007.

- [40] Wood, R.J. “Liftoff of a 60mg flapping-wing MAV”. *Intelligent Robots and Systems, 2007. IROS 2007. IEEE/RSJ International Conference on*, 1889 –1894. 29 2007-nov. 2 2007.
- [41] Wood, R.J., E. Steltz, and R.S. Fearing. “Nonlinear Performance Limits for High Energy Density Piezoelectric Bending Actuators”. *Robotics and Automation, 2005. ICRA 2005. Proceedings of the 2005 IEEE International Conference on*, 3633 – 3640. april 2005.
- [42] Wood, R.J., E. Steltz, and R.S. Fearing. “Optimal energy density piezoelectric bending actuators”. *Sensors and Actuators A: Physical*, 119(2):476 – 488, 2005. ISSN 0924-4247.
- [43] Yang, Jiashi (editor). *Special Topics in the Theory of Piezoelectricity*. Springer, 2009.
- [44] Yoon, K Joon, Seokjun Shin, Hoon C Park, and Nam Seo Goo. “Design and manufacture of a lightweight piezo-composite curved actuator”. *Smart Materials and Structures*, 11(1):163, 2002.
- [45] Zbikowski, Pedersen C. B. Hameed A. Friend C. M., R. and P.C. Barton. “Current Research on Flapping Wing Micro Air Vehicles at Shrivenham”.

REPORT DOCUMENTATION PAGE

Form Approved
OMB No. 0704-0188

The public reporting burden for this collection of information is estimated to average 1 hour per response, including the time for reviewing instructions, searching existing data sources, gathering and maintaining the data needed, and completing and reviewing the collection of information. Send comments regarding this burden estimate or any other aspect of this collection of information, including suggestions for reducing this burden to Department of Defense, Washington Headquarters Services, Directorate for Information Operations and Reports (0704-0188), 1215 Jefferson Davis Highway, Suite 1204, Arlington, VA 22202-4302. Respondents should be aware that notwithstanding any other provision of law, no person shall be subject to any penalty for failing to comply with a collection of information if it does not display a currently valid OMB control number. **PLEASE DO NOT RETURN YOUR FORM TO THE ABOVE ADDRESS.**

| | | | | | | |
|---|-----------------------------|------------------------------|--|---------------------------------------|--|--|
| 1. REPORT DATE (DD-MM-YYYY) 27-03-2013 | | | 2. REPORT TYPE Master's Thesis | | 3. DATES COVERED (From — To) Oct 2011–Mar 2013 | |
| 4. TITLE AND SUBTITLE Development of Optimized Piezoelectric Bending Actuators For Use in an Insect Sized Flapping Wing Micro Air Vehicle | | | | | 5a. CONTRACT NUMBER | |
| | | | | | 5b. GRANT NUMBER | |
| | | | | | 5c. PROGRAM ELEMENT NUMBER | |
| 6. AUTHOR(S) Lenzen, Robert K., Second Lieutenant, USAF | | | | | 5d. PROJECT NUMBER | |
| | | | | | 5e. TASK NUMBER | |
| | | | | | 5f. WORK UNIT NUMBER | |
| 7. PERFORMING ORGANIZATION NAME(S) AND ADDRESS(ES) Air Force Institute of Technology Graduate School of Engineering and Management (AFIT/EN) 2950 Hobson Way WPAFB, OH 45433-7765 | | | | | 8. PERFORMING ORGANIZATION REPORT NUMBER AFIT-ENY-13-M-21 | |
| 9. SPONSORING / MONITORING AGENCY NAME(S) AND ADDRESS(ES) intentionally left blank | | | | | 10. SPONSOR/MONITOR'S ACRONYM(S) | |
| | | | | | 11. SPONSOR/MONITOR'S REPORT NUMBER(S) | |
| 12. DISTRIBUTION / AVAILABILITY STATEMENT DISTRIBUTION STATEMENT A: APPROVED FOR PUBLIC RELEASE; DISTRIBUTION UNLIMITED | | | | | | |
| 13. SUPPLEMENTARY NOTES This work is declared a work of the U.S. Government and is not subject to copyright protection in the United States. | | | | | | |
| 14. ABSTRACT Piezoelectric bimorph actuators, as opposed to rotary electric motors, have been suggested as an actuation mechanism for flapping wing micro air vehicles (FWMAVs) because they exhibit favorable characteristics such as low weight, rapidly adaptable frequencies, lower acoustic signature, and controllable flapping amplitudes. Research at the Air Force Research Labs and the Air Force Institute of Technology has shown that by using one actuator per wing, up to five degrees of freedom are possible. However, due to the weight constraints on a FWMAV, the piezoelectric bimorph actuators need to be fully optimized to support free flight. This study focused on three areas of investigation in order to optimize the piezoelectric actuators: validating and improving analytical models that have been previously suggested for the performance of piezoelectric bimorph actuators; identifying the repeatability and reliability of current custom manufacturing techniques; and determining the failure criteria for piezoelectric actuators so that they can be driven at the highest possible voltage. Through the optimization, manufacturing, and performance testing of piezoelectric bimorphs, analytical models have been adjusted to fit the empirical data to yield minimum mass actuators that could potentially meet the mechanical energy requirements in a FWMAV. For custom manufactured actuators, optimized tapered actuators with an end extension showed an 89.5% energy density improvement over optimized rectangular actuators and a 19.5% improvement in energy density over commercially available actuators. | | | | | | |
| 15. SUBJECT TERMS Flapping Wing Micro Air Vehicle, Piezo Actuator, Bimorph Benders | | | | | | |
| 16. SECURITY CLASSIFICATION OF: | | | 17. LIMITATION OF ABSTRACT | 18. NUMBER OF PAGES 127 | 19a. NAME OF RESPONSIBLE PERSON Richard G. Cobb (ENY) | |
| a. REPORT U | b. ABSTRACT U | c. THIS PAGE U | | | 19b. TELEPHONE NUMBER (include area code) (937) 255-3636 ext. 4559 | |